Structure and Reaction Study of Light Hypernuclei by the Microscopic Cluster Model

Taiichi Yamada

Structure and Reaction Study of Light Hypernuclei by the Microscopic Cluster Model

Taiichi YAMADA

Department of Applied Mathematics,
Faculty of Engineering Science,
Osaka University, Toyonaka 560

Abstract

The properties of $L^{\pi}=1^{-}$ resonance states observed in the pion forward cross section of the $^{9}Be(K^{-},\pi^{-})^{9}_{\Lambda}Be$ reaction and the structures of $^{13}_{\Lambda}C$ and $^{21}_{\Lambda}Ne$ are investigated by the microscopic cluster model. In the former study we solve the coupled-channel scattering problem, in which the three channels, $^{5}_{\Lambda}He+\alpha$, $\Lambda+^{8}Be(0^{+})$ and $\Lambda+^{8}Be(2^{+})$, are taken into account. Then, a quantitative estimate of the cross section of the $^{9}Be(K^{-},\pi^{-})^{9}_{\Lambda}Be$ reaction is performed by employing the continuum-state wave functions of $^{9}_{\Lambda}Be$, which are obtained by solving the three-channel coupled problem under the outgoing wave boundary condition. We find two resonance states: The $L^{\pi}=1^{-}_{2}$ state corresponds to the middle peak observed in the (K^{-},π^{-}) cross section, and its energy and width are in good agreement with the experimental data. The $L^{\pi}=1^{-}_{1}$ state has not been seen experimentally, but it is expected to be observed if the coincidence experiments such as the $^{9}Be(K^{-},\pi^{-}\alpha)^{5}_{\Lambda}He$ reaction are carried out in future.

In the latter half of this paper the structures of $^{13}_{\Lambda}C$ and $^{21}_{\Lambda}Ne$, which are the typical heavier p-shell and sd-shell hypernuclei, are investigated by the microscopic $3\alpha+\Lambda$ and $\alpha+^{16}O+\Lambda$ cluster models, respectively. We calculate the energy spectra, B(E2) values, root mean square radii, etc. The obtained states are classified into some rotational bands according to the underlying intrinsic structure. We have many aspects characteristic of the heavy hypernuclei, which do not appear in the light p-shell hypernuclei. The present studies put emphasis on clarifying the dynamical coupling effects between the collective motions of nuclear core part and the Λ single-particle motions.

Contents

§1. Introduction

Hypernuclear physics is the physics of the baryon many-body system including the nucleon's one. The recent counter experiments on the (K^-,π^-) strangeness exchange reaction and their theoretical analyses have disclosed characteristic aspects of the structure of hypernuclei, and the hypernuclear physics has entered into a new stage.

Since the first discovery of hypernucleus at 1952, the emulsion experiments have been the unique source of information on the hypernuclear structure in first two decades. The binding energies and weak decay rates (life times) of mainly light hypernuclei have been measured[1] and given the information on lambda-nucleon (Λ-N) interaction and the Λ single particle potential[2]. The discovery of two double Λ-hypernuclei, ${}^{6}_{\Lambda\Lambda}\mathrm{He}$ and ${}^{12}_{\Lambda\Lambda}\mathrm{Be}$ [3),4], have given the information on the properties of Λ-Λ interaction. Very poor low-energy Λ-N and Σ-N scattering data, for example, the Λ-p and $\Sigma^{\pm}$-p elastic scattering cross section and angular distribution[5], are available even at present. These data are not enough to perform the phase-shift analysis. The theoretical analysis of the available data and predictions were performed intensively[6].

The counter experiments on the (K^-,π^-) reaction performed at CERN and BNL[7)~17)] in middle of 1970's have brought a new development of hypernuclear physics. Using this reaction, hyperon can be produced in the excited state of hypernucleus and we can investigate in detail the properties of hypernuclear

structure; the major-shell spacing $\hbar\Omega_\Lambda$, the effective Λ mass M^*_Λ, the depth of spin-orbit potential U^{so}_Λ and the widths of single-particle levels for Λ particle, in addition to the depth of single-particle potential U^0_Λ. The most interesting finding is that the depth of Λ single-particle spin-orbit potential is about zero. The energy of γ-ray has been measured in coincidence with pions from the $(K^-,\gamma\pi^-)$ reaction[11),14)] and more detailed weak decay rates have been studied experimentally[15)]. The (K^-,π^-) reaction can also produce the Σ-hypernuclei[16)~18)]. The narrow widths of Σ single-particle levels , in spite of large conversion width of $\Sigma N \to \Lambda N$, are unexpected findings. The quenching mechanism remains as a mysterious unsolved problem.

A theoretical approach of the baryon-baryon interactions using the one boson exchange (OBE) model has been performed by the Niimegen group[19)]. They have proposed two OBE potentials, model D and F, which were based on the available N-N, Λ-N and Σ-N data with the aid of the SU(3) symmetry but had different characteristics in some respects each other. For example these two models lead to complete different results both for the ΣN and $\Lambda\Lambda$ channels; the attractive/repulsive potential depth U^0_Σ and the attractive/repulsive Λ-Λ effective interactions. Recently the Brueckner G-matrix theory using the model D and F has been applied to the system with one hyperon (Y) in nuclear matter[20)]. The single-particle potential U_Y, the effective mass M^*_Y, the effective local Y-N interaction and so on have been calculated. The development of the theory of baryon many-body system with accumulating more detailed experimental data will undoubtedly

lead to the unified understanding of baryon-baryon interactions.

A systematic shell-model application to the p-shell Λ-hypernuclei has been performed intensively by Dalitz, Gal, Dover and their collaborators[21)~26)] since the beginning of 1970's. Their shell model calculations were done for $\{s_N^4\, p_N^{A-5} s_\Lambda\}$ or $\{s_N^4 p_N^{A-5} s_\Lambda, p_\Lambda\}$ configurations using the interaction of Cohen and Kurath for the core wave functions. Zofka et al.[27),28)] have also applied the extended shell model approach including higher configurations to light hypernuclei. The model study based on the SU(3) group classification has been performed for the A=9~13 hypernuclei by Zhang et al.[29)] On the other hand, Bodmer et al.[30)] have investigated the ground state properties of light hypernuclei by the simple cluster model[31)~34)]. A faddeev equation approach has been made by Sunami, Narumi[35)] and Oryu et al.[36)] In these applications the constituent clusters, however, have been treated as structureless particles.

A fully microscopic cluster model approach has been made systematically for light hypernuclei by Bandō, Ikeda, Motoba, Yamada et al.[37)~47)] since the beginning of 1980's. In light hypernuclei the cluster aspect is essentially important since this aspect widely proved to be indispensable in describing the structures of the ordinary p- and sd-shell nuclei[48),49)]. In the model the constituent clusters are treated as composite particles and the antisymmetrization are properly taken into account and the effective two-body N-N and Λ-N interactions can be used. The cluster model wave function includes not only the low-lying shell model configurations but higher-shell model configurations

without any spurious center-of-mass excitation. Thus, the microscopic cluster model is suitable for making the realistic quantitative estimates of the properties of the ground and excited states, the electromagmetic transition probabilities and the particle decay widths. Moreover, this model is also able to describe the dynamical change of nuclear core part due to the participation of a hyperon.

The study of the light p-shell Λ-hypernuclei within the framework of the microscopic α+x+Λ cluster model (x=n,p,d,t,^{3}He, α) has been performed by Motoba, Bandō and Ikeda et al[37),38),40)]. They have calculated the energy spectra, electromagmetic transition probabilities, effective neutron number in the (K^-,π^-) reaction and spectroscopic factors going to the (αx)-Λ and $^5_\Lambda$He-x channel, etc. The existing data are in reasonable correspondence to the above results. The theoretical study of multi-strange hypernuclei also has been performed by the microscopic cluster model[43)~47)]. The particularly interesting $^6_{\Lambda\Lambda}$He hypernucleus, which is called as "lampha", have been investigated by the α+Λ+Λ cluster model. This has approximately the $(0s)^6$-shell-model configuration, which is the lightest closed shell of the p,n and Λ system with a complete analogue to ^{4}He=α particle in the p,n system. The lampha is considered to play the same important role in hypernuclei as the alpha, which occupies an unique position in ordinary nuclei as an important unit of the cluster model.

The investigations of light Λ-hypernuclei including single or multiple Λ particles have disclosed characteristic aspects of hypernuclear structure: i) An interesting feature is the

stabilization of the system due to the glue-like role of the hyperons. The sizes, defomations or clusterings undergo sizable changes, which manifest themselves clearly in some observables such as electromagmetic transitions. Hypernuclear physics, thus, offers another way to investigate the dynamical response of nuclei due to the participation of hyperons as impurities. ii) Another feature is the appearance of many states with new symmetries which can never be realized in ordinary nuclei because of the Pauli principle. The states are called as "genuinely hypernuclear" in contrast to "analogue" which have their correspondents in ordinary nuclei. How purely the genuinely hypernuclear states are realized depends on the properties of the individual states of the individual hypernucleus due to the different couplings with the other states. iii) The other characteristic is the coexistence of weak and strong coupling features. The low-lying levels of the (α+x+Λ) hypernucleus with Λ particle occupying the S-state look very similar to the ground band of the (α+x) nucleus, as if showing the weak coupling feature, while the P-state Λ particle couples strongly with the rotational motion of the nuclear part (α+x) to exhibit a strong coupling type energy spectra. If the deformation is oblate, the situation change to a certain extent. How such coupling will be beyond p-shell hypernucleus is an interesting problem.

The purposes of this paper are the following two: The first one is to investigate quantitatively the properties of resonance states of typical light p-shell hypernucleus, ${}^{9}_{\Lambda}\mathrm{Be}$, of which structure was found to be described nicely by the microscopic

$\alpha+\alpha+\Lambda$ cluster model under the bound state approximation (BSA)[37),38),40)]. In the studies we treat the scattering boundary conditions properly for the various two-body decay channels[39),40)]. This advanced treatment enables us to not only make a theoretical analysis of available data but also give the reliable predictions. The second one is to apply the microscopic cluster model to heavier p-shell and sd-shell hypernuclei. It is interesting whether the characteristic aspects obtained by the investigations of light p-shell hypernuclei persist also in the heavy region or not. We have obtained new aspects characteristic of hypernuclei in this region. In this paper we report the studies on the structures of ${}^{13}_{\Lambda}C$ and ${}^{21}_{\Lambda}Ne$ as the typical heavy hypernuclei[41),42)].

In the previous studies of the ${}^{9}_{\Lambda}Be$ hypernucleus under the BSA[37),38),40)], the important physical quantities of resonance states such the energies and the particle-decay widths were estimated on the basis of the reduced-width amplitudes deduced from the BSA wave functions. Concerning the analysis of the (K^-,π^-) hypernuclear production reaction, the effective neutron numbers or the production ratios of hypernucleus through the reaction were calculated, but the widths and their mechanisms of peaks observed in the (K^-,π^-) reaction were not discussed quantitatively. In the low-energy region of our interest, three particle-decay channels, ${}^{5}_{\Lambda}He+\alpha$, $\Lambda+{}^{8}Be(0^+)$ and $\Lambda+{}^{8}Be(2^+)$, are open. Thus, we investigate the properties of resonance states of ${}^{9}_{\Lambda}Be$ by solving the coupled-channel scattering problem, in which the above three channels are taken into account[39),40)]. Then, a

quantitative estimates of the excitation spectra of the $^{9}Be(K^{-},\pi^{-})^{9}_{\Lambda}Be$ hypernuclear production reaction are performed. Note that the $^{9}_{\Lambda}Be$ state produced by the (K^{-},π^{-}) reaction lies in the continuum state, where the three particle-decay channels are open. We calculate the cross section of the (K^{-},π^{-}) reaction by employing the wave functions of the $^{9}_{\Lambda}Be$ continuum states, which are obtained by solving the three-channel coupled problem under the Kapur-Peierls-type outgoing wave boundary condition[50]. The obtained results are compared with the experimental data and some predictions are given.

The structure of ^{12}C in the low-energy region is known to be described nicely by the microscopic 3α cluster model[51),52)]. The $K^{\pi}=0^{+}$ band states $(0^{+}_{2}\text{-}2^{+}_{2})$ starting from 7.6 MeV excitation have been interpreted to have a loosely coupled 3α cluster structure contrastively to the shell-model-like compact structure of the ground band $(0^{+}_{1}\text{-}2^{+}_{1}\text{-}4^{+}_{1})$. What kinds of couplings arise between these states when Λ particle is added is a new problem not considered of $^{9}_{\Lambda}Be$. Thus, we investigate the structure of $^{13}_{\Lambda}C$ by the microscopic 3α+Λ cluster model[42], which takes into account both contrastive types of structures and their couplings in a natural way.

The observed energy spectra of ^{20}Ne in the low-energy region are classified into six rotational bands, among which the ground $K^{\pi}=0^{+}$ band, the fourth $K^{\pi}=0^{+}$ band starting from 8.3 MeV excitation (higher nodal band) and the $K^{\pi}=0^{-}$ band from 5.78 MeV (parity doublet partner of the ground band[53]) are described successfully by the microscopic $\alpha+^{16}O$ cluster model[52)~55)]. (The

other three bands can only be described well by taking into account the configuration of α plus excited ^{16}O cluster[52].) We study the structure of $^{21}_{\Lambda}Ne$ by the microscopic $\alpha+^{16}O+\Lambda$ cluster model[41),42)]. A new feature of $^{21}_{\Lambda}Ne$ is that the addition of Λ particle to the $\alpha+^{16}O$ core induces a coupling between the different parity states, which should be quite strong, since the energy gap between the doublet[53)] is not large. Such couplings induced in $^{21}_{\Lambda}Ne$ determine the properties of hypernuclear eigenstates such as the selectivities on some particle-decay modes. Another interesting feature is the stabilization of the so-called higher nodal band in $^{21}_{\Lambda}Ne$, which has a large α-decay width in the corresponding ordinary nucleus ^{20}Ne.

The contents of this paper are as followings: In §2 we give the coupled-channel formulation of the scattering problem, and the coupling mechanism of high-lying resonance states of $^{9}_{\Lambda}Be$ is discussed. Then, the coupled-channel treatment with the Kapur-Peierls-type outgoing wave boundary condition is formulated and the cross section of the $^{9}Be(K^{-},\pi^{-})^{9}_{\Lambda}Be$ hypernuclear production reaction is calculated. The comparison with experimental data is performed. Section 3 and 4 are devoted to study the structure of $^{13}_{\Lambda}C$ and $^{21}_{\Lambda}Ne$ by the microscopic $3\alpha+\Lambda$ and $\alpha+^{16}O+\Lambda$ cluster model, respectively. We show new aspects characteristic of the two typical hypernuclei. Finally we give in §5 a summary of our results and remarks.

§2. ${}^{9}_{\Lambda}$Be hypernucleus

The structure of ${}^{9}_{\Lambda}$Be which is a typical p-shell hypernucleus has been studied intensively by the shell model[21),22)] and the cluster model[37),38),40)]. Figure 1 shows the forward pion cross section of the ^{9}Be$(K^-,\pi^-){}^{9}_{\Lambda}$Be reaction[7)], where three peaks are observed. The microscopic $\alpha+\alpha+\Lambda$ three-cluster model under the bound state approximation (BSA)[37),38),40)] was found to describe nicely the structure of ${}^{9}_{\Lambda}$Be hypernucleus. Figure 2 exhibits the energy spectra of ${}^{9}_{\Lambda}$Be calculated on the basis of this model. In Fig.2 and hereafter we refer to the orbital angular momentum L specifying levels and thus, each level should be understood to be degenerate with respect to Λ-spin up and down. The ground band $K^\pi=0^+$ ($L^\pi=0^+-2^+-4^+$) has the dominant configuration where the Λ particle occupies the S-state with respect to the $\alpha+\alpha$ symmetric axis. In the $K^\pi=0^-(L^\pi=1^--3^--5^-)$ and $K^\pi=1^-(L^\pi=1^--2^--3^--4^-)$ bands the Λ particle occupies the P-orbits parallel and perpendicular, respectively, to the $\alpha+\alpha$ symmetric axis. The states belonging to the $K^\pi=0^+$ and 0^- bands are the so-called "genuinely hypernuclear states" which can never be realized in ordinary nuclei because of the Pauli exclusion principle. Since the $K^\pi=0^+$ and 1^- bands correspond to the configurations with the SU(3) classification $(\lambda\mu)=(40)$ and (31), they are called as "^{8}Be-analogue" and "^{9}Be-analogue", respectively. The $K^\pi=0^-$ band is a group of states with a new symmetry $(\lambda\mu)=(50)$, which has no correspondent in ordinary nuclei and is called as "super-symmetric" by Dalitz and Gal[22)].

The peaks at $E_\Lambda \simeq -6.7$ MeV and 6.3 MeV observed in the forward (K^-,π^-) reaction correspond to the $L^\pi=0^+$ (ground) and $L^\pi=1^-_2$ levels, respectively. The $L^\pi=1^-_1$ level is expected to be located at $E_\Lambda \simeq 0$ MeV but it has not been separately seen in the excitation function because of experimental conditions. Another strong peak observed at $E_\Lambda \simeq 17$ MeV is generated by the recoilless conversion of a neutron in the α clusters to Λ particle. Therefore this state can not be described within the framework of the $\alpha+\alpha+\Lambda$ model[37),38),40)].

We confine ourselves to the $L^\pi=1^-$ states with particular interest in the width of the 1^-_2 state. The $E_\Lambda \simeq 6.3$ MeV 1^-_2 state shows a nice peak behavior with the width $\Gamma \simeq 7$-8 MeV in spite of its considerably high location above the three particle-decay thresholds: ${}^{5}_{\Lambda}\mathrm{He}+\alpha$ at $E_\Lambda=-3.1$ MeV, $\Lambda+{}^{8}\mathrm{Be}(0^+)$ at $E_\Lambda=0.0$ MeV and $\Lambda+{}^{8}\mathrm{Be}(2^+)$ at $E_\Lambda=2.9$ MeV (see Fig.2). Note that the experimental resolution is about 2-3 MeV. The height of the centrifugal barrier for Λ-particle in the $L^\pi=1^-$ state is only about 3 MeV. Thus, the $L^\pi=1^-_2$ level is just located at the top of the centrifugal barrier with respect to the $\Lambda+{}^{8}\mathrm{Be}(2^+)$ threshold. With this in mind we study the energies and widths of the $L^\pi=1^-$ resonance states by solving the coupled-channel scattering problem, in which the above three channels are taken into account. The ${}^{5}_{\Lambda}\mathrm{He}$ and ${}^{8}\mathrm{Be}$ are represented by the $\alpha+\Lambda$ and $\alpha+\alpha$ cluster configurations, respectively. These microscopic cluster models describe nicely the ground state of ${}^{5}_{\Lambda}\mathrm{He}$ and the ground band of ${}^{8}\mathrm{Be}(\ell^\pi=0^+\text{-}2^+\text{-}4^+)$. In §2.1 we give a brief description of the coupled-channel formulation under the scattering boundary

condition. The results are presented and the mechanism underlying the obtained resonance states is discussed in detail.

The widths of resonance states obtained by solving the coupled-channel scattering problem described above, however, do not directly correspond to the ones in the excitation function of the forward $^{9}Be(K^{-},\pi^{-})^{9}_{\Lambda}Be$ reaction. Note that the $^{9}_{\Lambda}Be$ state produced by the (K^{-},π^{-}) reaction lies in continuum state, where the three particle-decay channels are open. In order to make realistic estimates of resonance energies and widths, we evaluate the cross section of the $^{9}Be(K^{-},\pi^{-})^{9}_{\Lambda}Be$ hypernuclear production reaction by employing the wave functions (wf's) of $^{9}_{\Lambda}Be$ in continuum state, which are obtained by solving the three-channel coupled equation under the outgoing wave boundary condition for each channel. The cross section of the (K^{-},π^{-}) reaction is calculated by making use of the distorted wave impulse approximation (DWIA) and the incoming $K^{-}$and outgoing π^{-} distorted wf's are obtained by employing the eikonal approximation. In §2.2 the coupled-channel treatment with the outgoing wave boundary condition is formulated, and the (K^{-},π^{-}) cross section in DWIA is calculated. The results are compared with the experimental data and discussed.

2.1. Particle-decay widths of $L^{\pi}=1^{-}$ states

Throughout this paper we treat the Λ particle as a spinless one, since the Λ-N spin-spin interaction does not contribute to the coupling potential between Λ particle and spin-saturated α-cluster, and also the Λ one-body spin-orbit potential has been experimentally found to be very week[7].

2.1.1 Formulation

Labelling the ${}^{5}_{\Lambda}\mathrm{He}+\alpha$, $\Lambda+{}^{8}\mathrm{Be}(0^{+})$ and $\Lambda+{}^{8}\mathrm{Be}(2^{+})$ channels as channels 1, 2 and 3, respectively, the trial wf Ψ_L of total system with the total orbital angular momentum L is expressed as

$$\Psi_L = \Phi_L^{(1)} + \Phi_L^{(2)} + \Phi_L^{(3)} , \tag{2.1}$$

$$\Phi_L^{(1)} = \sqrt{\frac{4!4!}{8!}}\,\mathcal{A}'\left\{\phi({}^{5}_{\Lambda}\mathrm{He})\phi(\alpha)\,\chi_L^{(1)}(R_1)Y_L(\hat{R}_1)\right\}_L , \tag{2.2}$$

$$\Phi_L^{(2)} = \left\{\phi({}^{8}\mathrm{Be};\ell=0)\,\chi_L^{(2)}(R_2)Y_L(\hat{R}_2)\right\}_L , \tag{2.3}$$

$$\Phi_L^{(3)} = \sum_{\lambda}\left\{\phi({}^{8}\mathrm{Be};\ell=2)\,\chi_\lambda^{(3)}(R_3)Y_\lambda(\hat{R}_3)\right\}_L , \tag{2.4}$$

where $\vec{R}_\beta$ and $\chi^{(\beta)}$ $(\beta=1,2,3)$ represent respectively the relative coordinate and relative-motion wf's between the relevant clusters (see Fig.3). The operator $\mathcal{A}'$ antisymmetrizes the nucleons belonging to different clusters.

The relative-motion wf's $\chi^{(\beta)}$ $(\beta=1,2,3)$ in Eqs.(2.2)∼(2.4) are expanded in terms of the locally peaked Gaussian basis:

$$\chi_L^{(\beta)}(R_\beta) = \sum_{D_\beta} f_L^{(\beta)}(D_\beta)\,\varphi_L(R_\beta;D_\beta) \qquad (R_\beta<R_\beta^c), \tag{2.5a}$$

$$= \delta_{\gamma\beta}\,\chi_L^{(-)}(k_\beta,R_\beta) - S_{\gamma\beta}\,\chi_L^{(+)}(k_\beta,R_\beta) \qquad (R_\beta>R_\beta^c), \tag{2.5b}$$

$$\varphi_L(R_\beta;D_\beta) = 4\pi(2\nu_\beta/\pi)^{3/4}\exp\{-\nu_\beta(R_\beta^2+D_\beta^2)\}\, \mathcal{J}_L(2\nu_\beta D_\beta R_\beta), \quad (2.6)$$

where the generator coordinate D_β specifies the relative distance in the β-th channel and $\mathcal{J}_L(z)$ is the spherical Bessel function with an imaginary argument. The $f_L^{(\beta)}(D_\beta)$'s denote the expansion coefficients. The $\chi_L^{(\pm)}(k_\beta;R_\beta)$ represent the incoming (-)/ outgoing (+) Coulomb wf with the channel wave number k_β and $S_{\gamma\beta}$ the S-matrix from the β- to γ-th channel. The wf (2.5a) is smoothly connected with the wf (2.5b) at the channel radius R_β^c. The size parameter in the wave packet $\varphi_L(R_\beta,D_\beta)$ in Eq.(2.6) is chosen so that combination with the associated reduced mass gives the same harmonic oscillator (h.o.) frequency Ω, for examples,

$$\nu_1 = 4(4M_N+M_\Lambda)/(8M_N+M_\Lambda)\ \nu_N\ , \quad (2.7a)$$

$$\nu_2(=\nu_3) = 8M_\Lambda/(8M_N+M_\Lambda)\ \nu_N\ , \quad \nu_N=M_N\Omega/2\hbar\ . \quad (2.7b)$$

where $M_N(M_\Lambda)$ is the mass of nucleon (Λ particle).

The wf $\phi(\alpha)$ represents the internal wf of the α-cluster with the lowest h.o. configuration $(0s)_N^4$. The internal wf $\phi(^5_\Lambda\mathrm{He})$ and $\phi(^8\mathrm{Be};\ell)$ in Eqs.(2.2)$\sim$(2.4) are described as

$$\phi(^5_\Lambda\mathrm{He}) = \phi(\alpha)\ \xi_{\ell_\Lambda}(\eta)\ Y_{\ell_\Lambda}(\hat{\eta}) \text{ with } \ell_\Lambda=0, \quad (2.8)$$

$$\phi(^8\mathrm{Be};\ell) = \frac{1}{\sqrt{2}}\sqrt{\frac{4!4!}{8!}}\,\mathcal{A}'\left[\phi(\alpha)\phi(\alpha)\psi_\ell(r)Y_\ell(\hat{r})\right], \quad (2.9)$$

where $\xi_{\ell_\Lambda}(\eta)$ and ℓ_Λ denote respectively the wf and the angular momentum referring to the α-Λ relative coordinate $\vec{\eta}$, and $\psi_\ell(r)$ and ℓ the α-α relative coordinate $\vec{r}$. The relative wf's $\xi_{\ell_\Lambda}(\eta)$ in Eq.(2.8) and $\psi_\ell(r)$ in Eq.(2.9) are also expanded in terms of the

locally peaked Gaussian basis :

$$\xi_{\ell_\Lambda}(\eta) = \sum_{d_1} f_{\ell_\Lambda}^{(\alpha\Lambda)}(d_1)\, \mathcal{G}_{\ell_\Lambda}(\eta;d_1), \tag{2.10}$$

$$\psi_\ell(r) = \sum_{d_2} f_\ell^{(\alpha\alpha)}(d_2)\, \mathcal{G}_\ell(r;d_2), \tag{2.11}$$

where the expansion coefficients $f_{\ell_\Lambda}^{(\alpha\Lambda)}(d_1)$ and $f_\ell^{(\alpha\alpha)}(d_2)$ are determined by solving the $\alpha+\Lambda$ problem with the folding model and the $\alpha+\alpha$ problem with the microscopic cluster model, respectively. The expansion basis wf's $\{\mathcal{G}\}$ in Eqs.(2.10) and (2.11) are defined by Eq.(2.6). Here the generator coordinate $d_1(d_2)$ specifies the α-Λ (α-α) distance.

The total Hamiltonian operator H is given by the total kinetic energy and nucleon(N)-nucleon(N) and lambda(Λ)-nucleon(N) interactions,

$$H = T + V_{NN} + V_{\Lambda N} \ , \tag{2.12}$$

$$T = \sum_{i=1}^{8} t_i^N + t^\Lambda - T_{c.m.} \ , \tag{2.13}$$

$$V_{NN} = \sum_{i<j=1}^{8} v_{NN}(i,j), \quad V_{\Lambda N} = \sum_{i=1}^{8} v_{\Lambda N}(\Lambda,i), \tag{2.14}$$

where the center-of-mass kinetic energy $T_{c.m.}$ is subtracted. From the variational principle

$$< \delta\Phi_L^{(\beta)} \mid H - E \mid \Psi_L > = 0 \qquad (\beta=1,2,3), \tag{2.15}$$

we get a set of coupled integro-differential equations to determine the expansion coefficients $f^{(\beta)}(D_\beta)$ and the S-matrix elements $S_{\gamma\beta}$ of the relative wf $\chi^{(\beta)}(R_\beta)$ in Eqs.(2.5a) and (2.5b). Here we follow the variational method developed by

Kamimura et al[56]. The overlap and Hamiltonian kernels evaluated in the framework of the generator coordinate method (GCM) are given in the Appendix A.

From the S-matrix element the cross section is given as

$$\sigma^{\lambda}(\beta \to \gamma) = \left[(2\lambda+1)/k_{\beta}^{2}\right] \mid \delta_{\gamma\beta} - S_{\gamma\beta} \mid^{2} , \qquad (2.16)$$

where λ denotes the relative angular momentum of the γ channel.

2.1.2. Two-body interactions and model space

As the two-body N-N interaction we employ the Volkov No.2 (2-range Gaussian) potential[57] with Majonara parameter m_{NN}=0.58. The Coulomb interaction is taken into account. The size parameter ν_N for nucleons in the α-cluster is taken to be 0.2711 fm^{-2} (ν_N=1/2b_N^2, b_N=1.358 fm). This choice of interaction and above size parameter leads to a successful reproduction of the α-α scattering data including the resonance characters of ^{8}Be ground band (ℓ=0, 2 and 4)[58]. The two-body Λ-N interaction is simply chosen as a Gaussian form with the range $\beta_{\Lambda N}$ equivalent to the two-pion exchange Yukawa form,

$$v_{\Lambda N}(r) = v_{\Lambda N}^{0} \exp\{-(r/\beta_{\Lambda N})^{2}\}, \qquad (2.17)$$

$$v_{\Lambda N}^{0} = -38.14 \text{ MeV}, \quad \beta_{\Lambda N} = 1.034 \text{ fm}. \qquad (2.18)$$

The strength $v_{\Lambda N}^{0}$ was determined so as to reproduce the observed Λ binding energy (B_{Λ}≃3.1 MeV) in $^{5}_{\Lambda}$He [2] within the framework of the α-Λ folding model.

In the present calculation the following channels and parameter values are employed:

(I) The three channels ($L^{\pi}=1^{-}$)

channel-1 : ${}^{5}_{\Lambda}\mathrm{He} + \alpha$,

channel-2 : $\Lambda + {}^{8}\mathrm{Be}(0^{+})$ $(\lambda=1)$,

channel-3 : $\Lambda + {}^{8}\mathrm{Be}(2^{+})$ $(\lambda=1)$,

(II) The generator coordinate mesh points

D_1 = 2.5, 3.0, ..., 6.5, 7.0 fm (10 points),

$D_2(D_3)$ = 0.5, 1.5, ..., 5.5, 6.5 fm (7 points),

d_1 = 0.5, 2.0, 3.5, 5.0 fm (4 points),

$d_2(d_3)$ = 1.2, 2.4, 3.6, 4.8, 6.0 fm (5 points),

(III) The channel radii

R_1^c = 7.5 fm , R_2^c (R_3^c) = 7.0 fm .

The $\lambda=3$ component in the $\Lambda+{}^{8}\mathrm{Be}(2^{+})$ channel was found to be unimportant[37),38),40)] and is neglected here. Note that the essential importance is the reproduction of the experimental threshold energies when we treat a scattering problem involving the different channels. The adopted parameters $\{d_1\}$ and $\{d_2(d_3)\}$ are satisfactory in this respect. The parameter choise of (II) and (III) describes well the behavior of wf in the internal region and also guarantees satisfactorily the unitarity of the S-matrix.

2.1.3. Energies and structure characteristics of $L^{\pi}=1^{-}$ states under the bound state approximation (BSA).

In order to clarify physical picture of the problem, first we solve the three-channel coupled problem under the BSA and investigate the structure characteristics of the obtained eigenstates. Let us define the channel probability which is the squared overlap of the three-channel coupled wf $\Psi_{BSA}(L_N)$ (N=I,II

,III) with each single-channel wf $\Phi^{(\beta)}_{BSA}(L_n)$ (n=1,2) (or wf $\Phi^{(2+3)}_{BSA}(L_n)$ (n=1,2) obtained by solving the $\Lambda+^8Be(0^+,2^+)$ two-channel problem):

$$P^{(\beta)}_{n,N} = | < \Phi^{(\beta)}_{BSA}(L_n) | \Psi_{BSA}(L_N) > |^2 . \qquad (2.19)$$

The obtained values are given in Table I.

The $L^\pi=1^-_I$ solution with $E_\Lambda(=-B_\Lambda)=-0.5$ MeV has an almost complete overlap with the $^5_\Lambda$He+α channel ($P^{(1)}_{1,I}=0.980$) and at the same time very large overlap with the first solution ($\Phi^{(2+3)}_{BSA}(1^-_1)$) of the $\Lambda+^8Be(0^+,2^+)$ two-channel equation. This indicates that three channels are not fully independent each other because of the antisymmetrization among the nucleons. The $L^\pi=1^-_{II}$ solution with $E_\Lambda=3.7$ MeV has a complete overlap with the higher nodal solution for $\Phi^{(1)}_{BSA}(1^-_2)$ of the $^5_\Lambda$He+α channel. Since the energy level is located considerably high with respect to the $^5_\Lambda$He+α threshold, the resonance-like behavior should not appear when the problem is treated under the scattering boundary condition. The third solution $L^\pi=1^-_{III}$ with $E_\Lambda=5.0$ MeV has a structure very similar to the second solution $\Phi^{(2+3)}_{BSA}(1^-_2)$ of the $\Lambda+^8Be(0^+,2^+)$ two-channel equation ($P^{(2+3)}_{2,III}=0.920$) and also a considerable amount of the $\Lambda+^8Be(2^+)$ channel component ($P^{(3)}_{1,III}=0.341$). The energy level is located around the top of the centrifugal barrier with respect to the $\Lambda+^8Be(2^+)$ threshold. Thus this state is expected to show a resonance-like structure under the scattering boundary condition. From these consideration we learn here that there can exist two 1^- states (1^-_I and 1^-_{III}) which will persist in the scattering problem.

2.1.4. Results and discussion

First we calculate the phase shifts of three independent channels, ${}^{5}_{\Lambda}\mathrm{He}+\alpha$, $\Lambda+{}^{8}\mathrm{Be}(0^{+})$ and $\Lambda+{}^{8}\mathrm{Be}(2^{+})$, without channel couplings. The phase shift of the ${}^{5}_{\Lambda}\mathrm{He}+\alpha$ channel does not reach 90° but we find a broad resonance-like structure in the cross section at $E_{\alpha}\simeq 3.0$ MeV because of the Coulomb plus centrifugal barrier. The higher nodal resonance of the ${}^{5}_{\Lambda}\mathrm{He}+\alpha$ channel does not appear as described in §2.1.3. Only the $\Lambda+{}^{8}\mathrm{Be}(2^{+})$ channel phase shift exceeds 90°, while the $\Lambda+{}^{8}\mathrm{Be}(0^{+})$ one does not reach 90° but is saturated about 60° around $E_{\Lambda}\simeq 6$ MeV. The reason is that the $\Lambda-{}^{8}\mathrm{Be}(2^{+})$ P-wave folding potential is enough strong to make a quasi-bound state, while the $\Lambda+{}^{8}\mathrm{Be}(0^{+})$ one is considerably weak (see Fig.5). This type of difference between the two folding potentials is due to the prolate deformation of the ${}^{8}\mathrm{Be}$ nucleus[59]. Note that these properties of the folding potentials make small the energy gap between the diagonal energies of the $\Lambda+{}^{8}\mathrm{Be}(0^{+})$ and $\Lambda+{}^{8}\mathrm{Be}(2^{+})$ channels. Thus, the $L^{\pi}=1^{-}$ states of the single $\Lambda+{}^{8}\mathrm{Be}(0^{+})$ and $\Lambda+{}^{8}\mathrm{Be}(2^{+})$ channels without any channel coupling are almost degenerate in energy. If the channel coupling is introduced, the two states are strongly coupled and largely separated in energy to form the $L^{\pi}=1^{-}_{1}$ and 1^{-}_{2} levels (see Fig.2 or Table I).

Let us switch on the channel couplings among three channels. The calculated cross sections $\sigma^{L=1}(\beta \to \gamma)$ and the absolute values of the S-matrix elements, $|S_{\gamma\beta}|$, for the incident ${}^{5}_{\Lambda}\mathrm{He}+\alpha$ and $\Lambda+{}^{8}\mathrm{Be}(0^{+})$ channels are shown in Fig.6 and 7, respectively, as a function of the $\alpha(\Lambda)$ incident energy $E_{\alpha}(E_{\Lambda})$ in the center-of-mass

frame ($E_\alpha^{cal} = E_\Lambda^{cal} + 2.5$ MeV).

We see a somewhat broad resonance at $E_\alpha \simeq 2.3$ MeV ($E_\Lambda \simeq -0.2$ MeV) with the width of about 2 MeV in the ${}^{5}_{\Lambda}$He+α elastic cross section. This corresponds to the $K^\pi=0^-$ band head state in the BSA; $L^\pi=1^-_1$ in Fig.2 or $L^\pi=1^-_I$ in Table I. Some structures also appear in the cross sections $\sigma^{L=1}(\beta \to \gamma)$ (and the absolute values of the S-matrix elements, $|S_{\gamma\beta}|$) when the $\Lambda+{}^{8}$Be(0^+) channel is open. These are due to the effect of the channel couplings. In the ^{9}Be(K^-,π^-)${}^{9}_{\Lambda}$Be experiment the corresponding peak has not yet been observed because of the following reasons: The ground state of the target ^{9}Be nucleus has the structure where a valence neutron occupies the P-orbit perpendicular to the α-α symmetric axis, while in the $K^\pi=0^-$ band head state of the produced ${}^{9}_{\Lambda}$Be hypernucleus the Λ particle occupies the P-orbits parallel to the α+α symmetric axis. Thus, the small overlap between the target ^{9}Be nucleus and the residual ${}^{9}_{\Lambda}$Be hypernucleus makes the cross section in the (K^-,π^-) reaction small. Moreover this peak seems to be masked by the tail of the second big peak observed at $E_\Lambda \simeq 6.3$ MeV. It is expected to be observed, however, if the coincidence experiments such as the ^{9}Be($K^-,\pi^-\alpha$)${}^{5}_{\Lambda}$He reaction are carried out in future.

In the inelastic cross section $\sigma^{L=1}(2 \to 3)$ from the $\Lambda+{}^{8}$Be(0^+) to $\Lambda+{}^{8}$Be(2^+) channel, there appears a broad resonance structure at $E_\Lambda \simeq 6.0$ MeV with the width of about 6 MeV. This resonance corresponds to the $K^\pi=1^-$ band head state in the BSA; $L^\pi=1^-_2$ in Fig.2 or $L^\pi=1^-_{III}$ in Table I. The energy ($E_\Lambda \simeq 6.3$ MeV) and the width ($\Gamma \simeq 6$ MeV) are in good agreement with the middle

peak ($E_\Lambda^{exp}\simeq 6.3$ MeV and $\Gamma^{exp}\simeq 7$-8 MeV) in the excitation spectra of the $^9Be(K^-,\pi^-)^9_\Lambda Be$ reaction. When the $\Lambda+^8Be(0^+)$ channel is open, in the resonance region, there appears a strong-energy dependence of the $|S_{22}|$ and $|S_{32}|$, while not so much in the $|S_{12}|$, as seen in Fig.7(b). This indicates that, around $E_\Lambda\simeq 6$ MeV, the $\Lambda+^8Be(0^+)$ and $\Lambda+^8Be(2^+)$ channels are strongly coupled each other but the coupling of these two channels with the $^5_\Lambda He+\alpha$ channel is weak. These properties have already seen in the BSA treatment (see Table I) and persist in the case of the present three-channel coupled scattering problem. The channel-coupling effects push up the $K^\pi=1^-$ band-head state to such a high energy position as $E_\Lambda\simeq$ 6.0 MeV but still just at the top of the centrifugal barrier with respect to the $\Lambda+^8Be(2^+)$ channel, so that the width of this resonance state comes to somewhat broad one ($\Gamma\simeq 6$ MeV).

A few words should be said here. Speaking exactly, the widths of the resonance states obtained by the present three-channel coupled scattering calculation do not directly correspond to the actual widths in the excitation spectra of the forward $^9Be(K^-,\pi^-)^9_\Lambda Be$ reaction. The present evaluated widths, however, are expected to simulate the experimental values because of the following reason: The wf of the outgoing pion in the (K^-,π^-) reaction would not be distorted so largely by the nuclear optical potential since the pion energy is very high ($P_\pi\simeq 600$ MeV/c, $T_\pi\simeq 480$ MeV). Thus, the observed pions carry the information about the structure of the $^9_\Lambda Be$ hypernucleus which is just generated by the recoilless conversion of a valence neutron to Λ particle. A more realistic calculation of the exitation function of the $^9Be(K^-,\pi^-)^9_\Lambda Be$ reaction is given in next §2.2.

2.2. Strength function of the $^{9}Be(k^{-},\pi^{-})^{9}_{\Lambda}Be$ hypernuclear production reaction

In order to make a realistic estimate of the energy and width of the second peak ($E_{\Lambda}^{exp}\simeq 6.3$ MeV and $\Gamma^{exp}\simeq 7$-8 MeV) in the excitation function of the forward $^{9}Be(K^{-},\pi^{-})^{9}_{\Lambda}Be$ reaction[7], we evaluate the cross section of the $^{9}Be(K^{-},\pi^{-})^{9}_{\Lambda}Be$ hypernuclear production reaction by employing the coupled-channel treatment with the Kapur-Peierls-type outgoing wave boundary condition[50] for each channel. Thus, the particle-decay width of $^{9}_{\Lambda}Be$ produced in the (K^{-},π^{-}) reaction is taken into account in a natual way.

2.2.1. Formulation

a) Wave function (wf) of $^{9}_{\Lambda}Be$ with the outgoing wave boundary condition

The particle-decay channel wf's of the $^{9}_{\Lambda}Be$ hypernucleus we consider are the following three with the total angular momentum $L^{\pi}=1^{-}$;

$$\Phi^{(1)}(E) = \sqrt{\frac{4!4!}{8!}}\,\mathcal{A}'\left\{\phi(^{5}_{\Lambda}He)\phi(\alpha)\chi^{(1)}(R_1;E)Y_{\ell=1}(\hat{R}_1)\right\}_{L=1}, \quad (2.20)$$

$$\Phi^{(2)}(E) = \left\{\phi(^{8}Be;0^{+})\chi^{(2)}(R_2;E)Y_{\ell=1}(\hat{R}_2)\right\}_{L=1}, \quad (2.21)$$

$$\Phi^{(3)}(E) = \left\{\phi(^{8}Be;2^{+})\chi^{(3)}(R_3;E)Y_{\ell=1}(\hat{R}_3)\right\}_{L=1}, \quad (2.22)$$

where $\phi(\alpha)$ is the internal wf of the α particle with the lowest $(0s)^{4}_{N}$ h.o. configuration. The internal wf's, $\phi(^{5}_{\Lambda}He)$ and $\phi(^{8}Be;0^{+},2^{+})$, are given in Eqs.(2.8) and (2.9), respectively.

The other notations are self-explanatory (see §2.1.). The total wf is given as

$$\Psi({}^{9}_{\Lambda}\mathrm{Be};E) = \Phi^{(1)}(E) + \Phi^{(2)}(E) + \Phi^{(3)}(E), \qquad (2.23)$$

$$E = E(K^-) + E({}^{9}\mathrm{Be}) - E(\pi^-) \ , \qquad (2.24)$$

where $E({}^{9}\mathrm{Be})$, $E(K^-)$ and $E(\pi^-)$ represent the internal energy of the ground state of the target ${}^{9}\mathrm{Be}$ nucleus, the incoming kaon and the outgiong pion energies, respectively. Thus, E denotes the available energy for ${}^{9}_{\Lambda}\mathrm{Be}$ in the ${}^{9}\mathrm{Be}(K^-,\pi^-){}^{9}_{\Lambda}\mathrm{Be}$ reaction.

The radial wf's, $\chi^{(\beta)}(R_\beta;E)$ (β=1,2,3), in Eqs.(2.20)∿(2.22) are expanded in terms of the locally peaked Gaussian basis $\{\ \varphi\ \}$ and satisfy the following outgoing wave boundary condition at the channel radius R^c_β:

$$\chi^{(\beta)}(R_\beta;E) = \sum_{D_\beta} f^{(\beta)}(D_\beta;E)\ \varphi_{\ell=1}(R_\beta;D_\beta) \quad (R_\beta<R^c_\beta) \ , \qquad (2.25)$$

$$\frac{d}{dR_\beta}\left[R_\beta\chi^{(\beta)}(R_\beta;E)\right] \Big/ \left[R_\beta\chi^{(\beta)}(R_\beta;E)\right] \Big|_{R_\beta=R^c_\beta} = O'_\beta(k_\beta,R^c_\beta) \Big/ O_\beta(k_\beta,R^c_\beta) \quad (R_\beta=R^c_\beta) \ , \qquad (2.26)$$

where the generator coordinate D_β denotes the relative distance between the relevant clusters. The $f^{(\beta)}(D_\beta;E)$'s are the expansion coefficients and $\varphi_\ell(R;D)$ is given in Eq.(2.6). The $O_\beta(k_\beta,R_\beta)$ is the outgoing Coulomb wf , which is expressed by

$$O_\beta(k_\beta,R_\beta) = G_{\ell=1}(k_\beta,R_\beta) + i\ F_{\ell=1}(k_\beta,R_\beta) \ , \qquad (2.27)$$

where F_ℓ and G_ℓ are the regular and irregular Coulomb functions, respectively. The k_β is the β-channel wave number of

$\{(2\mu_\beta/\hbar^2)(E-E_\beta)\}^{1/2}$ where $E_\beta(\mu_\beta)$ is the threshold energy (the reduced mass) of β-channel.

The continuum-state wf $\Psi(^{9}_{\Lambda}\mathrm{Be};E)$ with the outgoing wave boundary condition for each particle-decay channel are obtained by solving the coupled-channel integro-differential equations with the use of the Bloch operator[60]:

$$\sum_{\beta'} \int_0^{R_{\beta'}^c} R_{\beta'}^2 dR_{\beta'} \left\{ \mathcal{H}_{\beta\beta'}(R_\beta,R_{\beta'}) - W_n(E) N_{\beta\beta'}(R_\beta,R_{\beta'}) \right\} \chi_n^{(\beta')}(R_{\beta'}) = 0 \quad (R_\beta < R_\beta^c,\ \beta=1,2,3) \quad , \tag{2.28}$$

$$\mathcal{H}_{\beta\beta'}(R_\beta,R_{\beta'}) = H_{\beta\beta'}(R_\beta,R_{\beta'}) + \mathcal{L}_\beta(R_\beta,b_\beta)\delta_{\beta\beta'} \quad , \tag{2.29}$$

where $H_{\beta\beta'}$ and $N_{\beta\beta'}$ are the Hamiltonian and norm kernels, respectively, in the framework of the resonating group method (RGM). The Bloch operator $\mathcal{L}_\beta(R_\beta,b_\beta)$ is defined by

$$\mathcal{L}_\beta(R_\beta,b_\beta) = \frac{\hbar^2}{2\mu_\beta R_\beta} \delta(R_\beta - R_\beta^c) \left\{ \frac{d}{dR_\beta} R_\beta - b_\beta \right\} \quad , \tag{2.30}$$

$$b_\beta = \frac{d}{dR_\beta} \left[R_\beta \chi^{(\beta)}(R_\beta;E) \right] \Big/ \chi^{(\beta)}(R_\beta;E) \Big|_{R_\beta=R_\beta^c} \quad , \tag{2.31a}$$

$$= R_\beta^c \cdot O_\beta'(k_\beta,R_\beta^c) \Big/ O_\beta(k_\beta,R_\beta^c) \quad , \tag{2.31b}$$

where b_β is the logarithmic derivative of the radial wf $\chi^{(\beta)}(R_\beta;E)$ at the channel radius R_β^c and given in Eq.(2.31b) in the present treatment. Note that b_β is complex because of the outgoing wave boundary condition. In Eq.(2.28), $W_n(E)$ denotes the n-th eigenenergy which is complex

$$W_n(E) = \varepsilon_n(E) - i\Gamma_n(E)/2 \quad , \tag{2.32}$$

with Γ_n being interpreted as a sort of width of the n-th eigenstate $\Psi_n({}^{9}_{\Lambda}\mathrm{Be};E)$. As well known, the eigenstates satisfy the following biorthogonality and completeness:

$$\langle \tilde{\Psi}_n({}^{9}_{\Lambda}\mathrm{Be};E) \mid \Psi_{n'}({}^{9}_{\Lambda}\mathrm{Be};E) \rangle = \delta_{nn'} \quad , \tag{2.33}$$

$$\sum_n |\Psi_n({}^{9}_{\Lambda}\mathrm{Be};E)\rangle \langle\tilde{\Psi}_n({}^{9}_{\Lambda}\mathrm{Be};E)| = 1 \quad , \tag{2.34}$$

$$\tilde{\Psi}_n({}^{9}_{\Lambda}\mathrm{Be};E) = \left(T\Psi_n({}^{9}_{\Lambda}\mathrm{Be};E) \right)^* \quad , \tag{2.35}$$

where T is the usual time-reversal operator. In the present calculation the radial wf $\chi^{(\beta)}(R_\beta;E)$ is expanded as given in Eq.(2.25), and the expansion coefficient $f^{(\beta)}(D_\beta,E)$ and the eigenvalue W(E) are obtained by solving the Eq.(2.28) with the use of the variational method.

The total Hamiltonian H of ${}^{9}_{\Lambda}\mathrm{Be}$ system is given in Eqs.(2.12) ~(2.14). The N-N, Λ-N interactions and the parameters of the generator coordinate $\{D_\beta\}$ are the same as those used in §2.1. For the channel radii, $\{R^c_\beta\}$, we take the following values:

$$R^c_1 = 8.5 \text{ fm} \quad , \quad R^c_2 \ (R^c_3) = 8.0 \text{ fm} \ . \tag{2.36}$$

The above parameter choice is found to describe well the internal behavior of wf ($R_\beta < R^c_\beta$) with the outgoing wave boundary condition. The expression of various matrix elements are given in Appendix A, which are the same as those given in §2.1.

b) Strength function

The double differential cross section of the (K^-,π^-)

reaction in the distorted wave impulse approximation (DWIA) is expressed as

$$\frac{d^2\sigma}{dEd\Omega_\pi} = \left[\frac{d\sigma}{d\Omega_\pi}\right]_{K^-n\to\Lambda\pi^-} \times S(E) \quad , \tag{2.37}$$

where $(d\sigma/d\Omega_\pi)_{K^-n\to\Lambda\pi^-}$ is the differential cross section of the elementary process. The S(E) is the strength function and given by the following formula:

$$S(E) = -\frac{1}{\pi} \, \mathrm{Im} < \Psi(^9\mathrm{Be}) \mid \hat{O}^\dagger \frac{1}{E - H + i\varepsilon} \hat{O} \mid \Psi(^9\mathrm{Be}) >, \tag{2.38}$$

Here, H and E are given in Eqs.(2.12) and (2.24), respectively, and $\Psi(^9\mathrm{Be})$ is the ground-state wf of the target ^{9}Be nucleus. The operator $\hat{O}$ in Eq.(2.38) is the $n \to \Lambda$ transition operator[61),62)],

$$\hat{O} = \int d\vec{r}^3 \, \chi^{(-)*}_{p_{\pi^-}}(\vec{r}) \, \chi^{(+)}_{p_{K^-}}(\vec{r}) \sum_{k=1}^{9} \delta(\vec{r}-\vec{r}_k) \, u_-(k) \quad , \tag{2.39}$$

where $u_-(k)$ denotes the u-spin lowering operator acting on k-th nucleon:

$$u_- \mid n> = \mid \Lambda> \quad , \quad u_- \mid p> = 0 \; . \tag{2.40}$$

Here, $|n>$, $|p>$ and $|\Lambda>$ express the state vectors of neutron, proton and lambda, respectively. With the use of the biorthogonality and completeness of the $^9_\Lambda$Be eigenstates given in Eqs.(2.33) and (2.34), we can express the strength function S(E) as

$$S(E) = -\frac{1}{\pi} \, \mathrm{Im} \sum_n \frac{N_n(E)}{E - W_n(E)} \quad , \tag{2.41}$$

$$N_n(E) = <\Psi(^9\mathrm{Be})|\hat{O}^\dagger|\Psi(^9_\Lambda\mathrm{Be};E)> <\Psi(^9_\Lambda\mathrm{Be};E)|\hat{O}|\Psi(^9\mathrm{Be})>. \tag{2.42}$$

Since the relevant $L^{\pi}=1^{-}$ states of ${}^{9}_{\Lambda}$Be hypernucleus are generated by the recoilless conversion of a valence neutron of the target ^{9}Be nucleus to Λ particle, we consider that the $u_{-}(k)$ in Eq.(2.39) operates only the valence neutron.

The kaon and pion distorted waves are calculated by employing the eikonal approximation since the incident K^{-} and outgoing π^{-} energies are very high (p_K=790 MeV/c and $p_\pi \simeq$600 MeV/c):

$$\chi^{(+)}_{p_{K^-}}(\vec{r}) = \exp\left[i\vec{p}_K\cdot\vec{r} - i\frac{1}{v_K}\int_{-\infty}^{z} U_K(\sqrt{b^2+z'^2}\,)\,dz' \right], \quad (2.43)$$

$$\chi^{(-)*}_{p_{\pi^-}}(\vec{r}) = \exp\left[-i\vec{p}_\pi\cdot\vec{r} + i\frac{1}{v_\pi}\int_{Z}^{\infty} U^{*}_\pi(\sqrt{B^2+Z'^2}\,)\,dZ' \right], \quad (2.44)$$

$$z = \vec{p}_K\cdot\vec{r}/p_K, \quad b = \sqrt{r^2-z^2}, \quad Z = \vec{p}_\pi\cdot\vec{r}/p_\pi, \quad B = \sqrt{r^2-Z^2}, \quad (2.45)$$

where p_K (v_K) and p_π (v_π) are the kaon and pion momentums (velocities), respectively. As for the meson-nucleus optical potential $U_m(r)$ (m=K,π), we employ the lowest order one given by the multiple scattering theory:

$$U_m(r) = -i\frac{v_m}{2}\bar{\sigma}_{mN}(1-i\alpha_m)\rho(r) \qquad (m=K,\pi). \quad (2.46)$$

Here, $\bar{\sigma}_{mN}$ denotes the avarage total cross section of the elementary process, and $\rho(r)$ is the density distribution of the target ^{9}Be nucleus, and α_m is the ratio of the real to imaginary part. According to the Ref.61) and 62), we calcualte the distorted waves by employing the parameters, $\bar{\sigma}_{KN}=\bar{\sigma}_{\pi N}$=30 mb and α_m=0, for p_K=790 MeV/c. The product of the distorted waves in

Eq.(2.39) are expanded in the multipole series with the use of the expressions in Eqs.(2.43) and (2.44):

$$\chi^{(-)*}_{p_{\pi^-}}(\vec{r})\ \chi^{(+)}_{p_{K^-}}(\vec{r}) = \sum_{k\mu} \sqrt{4\pi}\ \sqrt{2k+1}\ i^k\ \gamma_{k\mu}(p_K, p_\pi, \theta_{\pi^-}; r) Y_{k\mu}(\hat{r}), \quad (2.47)$$

where θ_{π^-} is the pion scattering angle with respect to the kaon incident direction.

For the ground-state wf of the target ^{9}Be nucleus, we employ the one obtained by the microscopic α+α+n cluster model[63]. The model is found to describe nicely the structure of ^{9}Be in the low-energy region. The explicit expression of the squared transition matrix element $N_n(E)$ in Eq.(2.42) is given in Appendix B.

2.2.2. Results and discussion

First we discuss the characteristics of the eigenstates $\Psi_n(^9_\Lambda\mathrm{Be};E)$ and the energy-dependence of their eigenvalues $W_n(E_\alpha)$ (n=1-3) which are given in Fig.8, where E_α corresponds to the energy E in Eq.(2.24) measured with respect to the $^5_\Lambda$He+α theshold. According to the wf analysis under the BSA (see §2.1.3), $\Psi_{n=1}$ has a large overlap with the $^5_\Lambda$He+α channel and simultaneously with the $\Phi^{(2)}+\Phi^{(3)}$ combination, $\Psi_{n=2}$ with the excited $\Phi^{(1)}$ and $\Psi_{n=3}$ with the $\Phi^{(2)}-\Phi^{(3)}$ combination. Thus, the eigenstates, $\Psi_{n=1}$ and $\Psi_{n=3}$, correspond to the $K^\pi=0^-$ and 1^- band-head states, respectively. As seen in Fig.8, the state $\Psi_{n=1}$ has width $\Gamma_{n=1}$ (of Eq.(2.32)) of about 1 MeV which entirely comes from the $^5_\Lambda$He+α decay, while $\Psi_{n=3}$ has width of about 4 MeV for which all the three decay channels are open. This width comes

almost entirely from the decay into the $\Lambda+{}^{8}Be(0^{+},2^{+})$ channels, and its size at such a high energy position is relevant to the present problem of our interest. The eigenstate $\Psi_{n=2}$ has a large decay width $\Gamma_{n=2}\simeq 6\text{-}7$ MeV since this state corresponds to the higher nodal state of the ${}^{5}_{\Lambda}He+\alpha$ channel, and the energy level is located above the Coulomb plus centrifugal barrier.

Table II lists the calculated squared values of the transition matrix element $N_n(E_\alpha)$ in Eq.(2.42) and also $W_n(E_\alpha)$, n=1-3, for p_K-=790 MeV/c and θ_π=0°. The value of $N_{n=1}$ is small because of the following: In the ground state of the target ${}^{9}Be$ nucleus a valence neutron occupies the $K^\pi=1^-$ molecular orbit, while the Λ particle in the $L^\pi=1^-_1$ state of the residual ${}^{9}_{\Lambda}Be$ hypernucleus occupies the $K^\pi=0^-$ one. Thus, a small overlap between both wf's makes the $N_{n=1}$ value small. The state $\Psi_{n=3}$, however, has a large $N_{n=3}$ value since the Λ particle occupies the $K^\pi=1^-$ molecular orbit. This substitutional state is expected to be populated strongly in the strength function S(E). The state $\Psi_{n=2}$ has a small $N_{n=2}$ value and a large decay width $\Gamma_{n=2}$, and therefore should not appear as any structure in the S(E).

Figure 9 shows the calculated strength function S(E) for p_K-=790 MeV/c and θ_π-=0°, 5° and 10°, where the lowest ten states ($\Psi_n({}^{9}_{\Lambda}Be;E)$, n=1-10) are taken into account. At the forward pion angle (θ_π-=0°) for which the observation was done, there exist two peaks: a small peak at $E_\Lambda\simeq -0.5$ MeV with the width $\Gamma\simeq 2$ MeV and a big peak at $E_\Lambda\simeq 6.0$ MeV with the width $\Gamma\simeq 6$ MeV. The latter big peak corresponds to the $K^\pi=1^-$ band-head $L^\pi=1^-_2$ state and is in good agreement with experimental data ($E_\Lambda^{exp}\simeq 6.3$ MeV and $\Gamma^{exp}\simeq 7\text{-}8$

MeV). The origin of the width of this peak is the Λ escape width for decay into the $\Lambda+{}^{8}\mathrm{Be}(0^{+},2^{+})$ channels. The lower small peak corresponds to the genuinely hypernuclear $L^{\pi}=1^{-}_{1}$ state and the width comes from the decay into the ${}^{5}_{\Lambda}\mathrm{He}+\alpha$ channel. This state has not been observed because of the various experimental condition (see §2.1).

When the pion scattering angle θ_{π^-} increases and the momentum transfer becomes larger, the strength of the upper peak decreases and at $\theta_{\pi^-}=10°$ there is no longer the visible-peak behavior around $E_{\Lambda}\simeq 6$ MeV since this state is the substitutional-type. On the other hand, the small peak at $E_{\Lambda}\simeq -0.5$ MeV remains unchanged against increased θ_{π^-}. The interesting $L^{\pi}=1^{-}_{1}$ state will be hopefully observed, if the $\pi^{-}\alpha$ coincidence experiments such as the ${}^{9}\mathrm{Be}(K^{-},\pi^{-}\alpha){}^{5}_{\Lambda}\mathrm{He}$ reaction are carried out in future.

§3. Structure of $^{13}_{\Lambda}C$

In this section, we present an investigation of the structure of $^{13}_{\Lambda}C$ by the microscopic 3α+Λ cluster model[42]. The nucleus ^{12}C is typical coexistent nuclear system of the shell-model like structure and the well-developed cluster structure; that is, i) the shell-model like ground $K^{\pi}=0^{+}_{1}$ band ($\ell^{\pi}=0^{+}_{1}$-2^{+}_{1}-4^{+}_{1}) and its parity-doublet $K^{\pi}=3^{-}$ band ($\ell^{\pi}=3^{-}$), ii) the $K^{\pi}=0^{+}_{2}$ band ($\ell^{\pi}=0^{+}_{2}$-2^{+}_{2}) with the loosely bound 3α cluster structure, iii) the $K^{\pi}=1^{-}$ band ($\ell^{\pi}=1^{-}$) with the intermediate structure. The two contrastive structures of ^{12}C are known to be described nicely by the microscopic 3α cluster model[51),52)], as shown in Fig.10. Therefore the study of $^{13}_{\Lambda}C$ within the framework of the microscopic 3α+Λ cluster model can take into account the effect of the dynamical coupling between the Λ particle motion and the two kinds of characteristic nuclear structures.

3.1. Formulation of the microscopic 3α+Λ model

The total wf Ψ_L of a $^{13}_{\Lambda}C$ state with the total orbital angular momentum L is expanded as

$$\Psi_L = \sum_{c,n} \omega_c(n) \left[\Phi_{i\ell}(\xi) \otimes u_{n\lambda}(\vec{R}) \right]_L , \qquad (3.1)$$

where $c=(i\ell,\lambda)_L$ denotes a channel of the angular momentum coupling. Here, in Eq.(3.1), $\Phi_{i\ell}(\xi)$ (ξ: whole nucleon coordinates) represents the i-th state of ^{12}C with angular momentum ℓ obtained by solving the equation of the 3α resonating group method (RGM) and $u_{n\lambda}(\vec{R})= u_{n\lambda}(R)\cdot Y_{\lambda}(\hat{R})$ the normalized

harmonic oscillator (h.o.) wf of the Λ-^{12}C relative coordinate $\vec{R}$ with $N=2n+\lambda$ quanta.

The total Hamiltonian of the $3\alpha+\Lambda$ system can be written in the following form ;

$$H = h(^{12}C) + T_\Lambda + V_{\Lambda N} \quad , \tag{3.2}$$

$$h(^{12}C) = \sum_{i=1}^{12} t_i + \sum_{i<j=1}^{12} v_{NN}(i,j) - T_G \quad , \tag{3.3}$$

$$V_{\Lambda N} = \sum_{i=1}^{12} v_{\Lambda N}(\Lambda,i) \quad , \tag{3.4}$$

where $h(^{12}C)$ is the internal Hamiltonian for the 3α nuclear part with the center-of-mass (c.m.) kinetic energy T_G subtracted and the other notations are self-explanatory.

The equation of motion is expressed as a set of coupled-channel linear equations for the coefficients $\omega_c(n)$;

$$\sum_{c_2 n_2} \Big[\{ T_\Lambda^{\lambda_1}(n_1,n_2) - (E_L-\varepsilon_{c_1})\delta_{n_1,n_2} \} \delta_{c_1,c_2} + U_L(c_1 n_1, c_2 n_2) \Big] \omega_{c_2}(n_2) = 0 \quad , \tag{3.5}$$

$$T_\Lambda^\lambda(n_1,n_2) = \langle u_{n_1\lambda}(\vec{R}) | \; T_\Lambda \; | u_{n_2\lambda}(\vec{R}) \rangle \quad , \tag{3.6}$$

$$U_L(c_1 n_1, c_2 n_2) = \langle u_{n_1\lambda_1}(R) | \; U_L(R;c_1,c_2) \; | u_{n_2\lambda_2}(R) \rangle \quad , \tag{3.7}$$

$$U_L(R;c_1,c_2) = \langle \Big[\Phi_{i_1\ell_1}(\xi) \; Y_{\lambda_1}(\hat{R}) \Big]_L | V_{\Lambda N} | \Big[\Phi_{i_2\ell_2}(\xi) \; Y_{\lambda_2}(\hat{R}) \Big]_L \rangle, \tag{3.8}$$

$$\varepsilon_c = \langle \Phi_{i\ell}(\xi) | \; h(^{12}C) \; | \Phi_{i\ell}(\xi) \rangle \quad . \tag{3.9}$$

where E_L is the total energy of a ${}^{13}_{\Lambda}C$ state and ε_c the eigenenergy of $i\ell$ state of ${}^{12}C$.

The channel coupling in Eq.(3.5) is induced by U_L which is the Λ-N interactions folded by the transition density matrix of the totally antisymmetrized 3α RGM wf's $\Phi_{i\ell}(\xi)$. The transition density matrix of ${}^{12}C$ is defined by

$$\rho_{i\ell m,i'\ell'm'}(\vec{r}) = \int d\xi\ \Phi^*_{i\ell m}(\xi) \sum_{k=1}^{12} \delta(\vec{r}-\vec{r}_k)\ \Phi_{i'\ell'm'}(\xi), \quad (3.10)$$

and can be expanded in the following multipole series:

$$\rho_{i\ell m,i'\ell'm'}(\vec{r}) = \sum_{k,\mu} (\ell'm'k\mu|\ell m)\ (-)^{\ell}\ (4\pi(2k+1))^{1/2} \times \overset{\circ}{\rho}{}^{(k)}_{i\ell,i'\ell'}(r)\ Y^*_{k\mu}(\hat{r}), \quad (3.11)$$

where $\vec{r}_k$ (each nucleon coordinate) and $\vec{r}$ are measured with respect to the c.m. of ${}^{12}C$. The multipole transition density matrix element $\overset{\circ}{\rho}{}^{(k)}_{i\ell,i'\ell'}(r)$ is approximately expanded in terms of the Gaussian basis:

$$\overset{\circ}{\rho}{}^{(k)}_{i\ell,i'\ell'}(r) = \sum_{n=1}^{N} \overset{\circ}{C}{}^{(k)}_{i\ell,i'\ell'}(n)\ (r/r_n)^k \exp(-r^2/r_n^2), \quad (3.12)$$

$$r_n = r_1 a^{n-1} \quad (n=1\text{-}N). \quad (3.13)$$

Here, after choosing a set of N, r_1 and r_N, the coefficients $\overset{\circ}{C}{}^{(k)}_{i\ell,i'\ell'}(n)$ are determined in order to minimize the integrated value of the squared derivation of expansion. If the Λ-N interaction is given in the form of Gaussian type as in Eq.(2.17), the folding potential $U_L(R;c_1,c_2)$ in Eq.(3.8) is expressed by

$$U_L(R;c_1,c_2) = (-)^L \sqrt{[\ell_1][\ell_2][\lambda_1][\lambda_2]}$$

$$\times \sum_k (\lambda_1 0 \lambda_2 0 | k0)\ W(\ell_1\lambda_1\ell_2\lambda_2;Lk)\ \overset{\circ}{U}{}^{(k)}_{i_1\ell_1,i_2\ell_2}(R), \quad (3.14)$$

$$\overset{\circ}{U}{}^{(k)}_{i_1\ell_1,i_2\ell_2}(R) = v^0_{\Lambda N}\ (\pi\beta^2_{\Lambda N})^{3/2} \sum_{n=1}^{N} \overset{\circ}{C}{}^{(k)}_{i_1\ell_1,i_2\ell_2}(n) \left[\frac{r_n^2}{\beta^2_{\Lambda N}+r_n^2} \right]^{3/2}$$

$$\times \left[\frac{r_n R}{\beta^2_{\Lambda N}+r_n^2} \right]^k \exp\left[-R^2/(\beta^2_{\Lambda N}+r_n^2) \right], \quad (3.15)$$

where $[\ell]$ is $2\ell+1$, and $\beta_{\Lambda N}$ and $v^0_{\Lambda N}$ are the range and depth of the Λ-N interaction, respectively. We use the transition density matrices of ^{12}C given by Kamimura[64].

3.2. Electric quadrupole transition probability

The operator of the electric quadrupole transition acting only on protons can be effectively given as

$$\hat{M}(E2) = \frac{e}{2} \left[\hat{Q}(3\alpha) + \hat{Q}(\Lambda) \right], \quad (3.16)$$

where $\hat{Q}(3\alpha)$ is the mass quadrupole operator of 3α nuclear part and $\hat{Q}(\Lambda)$ takes into account the recoil effect,

$$\hat{Q}(3\alpha) = \sum_{k=1}^{12} \vec{r}_k^{\,2}\ Y_2(\hat{r}_k), \quad (3.17)$$

$$\hat{Q}(\Lambda) = \frac{12M_\Lambda^2}{(12M_N+M_\Lambda)^2} R^2\ Y_2(\hat{R}). \quad (3.18)$$

The reduced quadupole transition probability $B(E2;L_i \to L_f)$ is expressed by

$$B(E2;L_i \to L_f) = e^2[L_f] \left\{ \sum_{c_f n_f} \sum_{c_i n_i} \omega_{c_f}(n_f)\, \omega_{c_i}(n_i) \right.$$

$$\times \left[\delta_{\lambda_f \lambda_i} \delta_{n_f n_i} (-)^{\lambda_i+\ell_i-L_f} \sqrt{[\ell_f]}\, W(\ell_f L_f \ell_i L_i;\lambda_i 2) \right.$$

$$\times (-)^{\ell_f} \sqrt{[\ell_i]}\, \frac{15\pi}{16} \sum_{n=1}^{N} \overset{\circ}{C}{}^{(2)}_{k_f \ell_f, k_i \ell_i}\, r_n^5$$

$$+ \delta_{\ell_f \ell_i} (-)^{\ell_f+\lambda_f-L_i} \sqrt{[\lambda_f]}\, W(\lambda_f L_f \lambda_i L_i;\ell_i 2)$$

$$\left. \left. \times \sqrt{\frac{5}{4\pi}}\, \frac{6M_\Lambda^2}{(12M_N+M_\Lambda)^2} (\lambda_f 020|\lambda_i 0) \langle u_{n_f \lambda_f}(R)|R^2|u_{n_i \lambda_i}(R)\rangle \right] \right\}^2, \quad (3.19)$$

where $c_i=(k_i\ell_i,\lambda_i)_{L_i}$ and $c_f=(k_f\ell_f,\lambda_f)_{L_f}$ denote the initial and final channels of the angular momentum coupling, respectively.

3.3. Root mean square (r.m.s.) radii

The r.m.s. radius of 3α nuclear part, $\sqrt{\langle r^2\rangle}$, and that of the Λ-^{12}C(3α) relative coordinate $\vec{R}$, $\sqrt{\langle R^2\rangle}$, are given by

$$\langle \Psi_L|r^2|\Psi_L\rangle = \frac{\pi^{3/2}}{8} \sum_{c,c',n} \delta_{\ell\ell'}\, \delta_{\lambda\lambda'}\, \omega_c(n)\, \omega_{c'}(n')$$

$$\times (-)^{\ell} \sqrt{[\ell']} \sum_{n=1}^{N} \overset{\circ}{C}{}^{(0)}_{i\ell, i'\ell'}(n)\, r_n^5 \ , \quad (3.20)$$

$$\langle \Psi_L|R^2|\Psi_L\rangle = \sum_{c,n,n'} \omega_c(n)\, \omega_c(n')$$

$$\times \langle u_{n\lambda}(R)|R^2|u_{n'\lambda}(R)\rangle \ . \quad (3.21)$$

3.4. Model space and Λ-N interaction

Our model space is specified by the 3α-Λ h.o. quanta $N=2\lambda+n$

and the channel $c=(i\ell,\lambda)_L$. In the present calculation, the following truncation of the model space is made:

(1) the 3α-Λ h.o. quanta

$N=2n+\lambda$ with $n=0,1,2,3,4$ and $\lambda^\pi=0^+,1^-,2^+,3^-$,

(2) the $^{12}C(3\alpha)$ states

$\ell = 0_1, 0_2 ; 2_1, 2_2 ; 4_1$ for $k^\pi=0^+$,

$\ell = 1_1$ for $k^\pi=1^-$; $\ell = 3_1$ for $k^\pi=3^-$.

Figure 11 shows the energy levels of ^{12}C calculated by the 3α RGM. Those corresponding to the observed states shown in Fig.10 are drawn by solid lines. For energy spectra of ^{12}C given in Eqs.(3.5) and (3.9), we use the experimental energies for the observed states and the calculated RGM eigenvalues for the other higher states. This ajustment of the calculated results is necessary to see the realistic effect of the participation of Λ particle. The truncation of model space and the ajustment of ^{12}C energy mentioned above are found to be good enough to describe the low-lying states of $^{13}_{\Lambda}C$.

The two-body Λ-N interaction is simply chosen as a Gaussian form with the range $\beta_{\Lambda N}=1.034$ fm (equilvalent to the two pion exchange Yukawa form) and the strength $v^0_{\Lambda N}=-35.4$ MeV, which reproduces the Λ-binding energy $B_\Lambda^{exp}= 11.22 \pm 0.08$ MeV in $^{13}_{\Lambda}C$ [13].

We label each of the obtained bands of $^{13}C(K^\pi)$ by means of its leading component $\left\{ k\otimes\lambda \right\}$, where k denotes the intrinsic quantum number of ^{12}C and λ a Λ-^{12}C state.

3.5. Energy spectra and structure characteristics

First we show in Fig.12 the density distributions of the $\ell^\pi=0_1^+$, 2_1^+, 4_1^+, 0_2^+, 2_2^+, 1_1^- and 3_1^- states of ^{12}C calculated by the 3α RGM[64]. The corresponding s-wave folding potentials for Λ-$^{12}C(\ell^\pi)$ are also shown in Fig.12, together with the energy of each eigenstate. The density distributions clearly exhibit the coexistence of the shell-model-like states ($\ell^\pi=0_1^+$, 2_1^+, 4_1^+, 3_1^-) and the loosely coupled 3α cluster-like states ($\ell^\pi=0_2^+$, 2_2^+). Note that the structure of 1_1^- state is intermediate between them. Reflecting the drastic dependence of the density distributions of ^{12}C on its states, the folding potentials for Λ-$^{12}C(0_1^+,2_1^+,4_1^+)$ are deep ($\sim$ -35 MeV) and short-ranged ($\sim$ 4.5 fm), while those for Λ-$^{12}C(0_2^+,2_2^+,1_1^-)$ are shallow ($\sim$ -15 MeV) and long-ranged ($\sim$ 6.5 fm). Thus, the eigenstate for Λ-$^{12}C(0_1^+)$ gives a binding energy of 3.5 times as large as that for Λ-$^{12}C(0_2^+)$, and the energy splitting between them becomes about 15 MeV in contrast to 7.65 MeV between the 0_1^+ and 0_2^+ states in ^{12}C. The s-wave folding potential for Λ-$^{12}C(3_1^-)$ has an intermediate depth ($\sim$ -21 MeV) and range ($\sim$ 5.5 fm) among others. The reason of this is following: The 3_1^- state of ^{12}C, which constitutes an inversion doublet with the ground state 0_1^+ [52], has a rather shell-model-like character but a little looser structure than 0_1^+ ($\sqrt{\langle r^2\rangle}_{3\alpha}$=2.42 fm in 0_1^+ vs. 2.77 fm in 3_1^-; cf. 3.55 fm in 0_2^+).

Let us switch on the channel couplings. The obtained energy levels can be classified into nine bands, namely, three $K^\pi=0^+$ bands, two $K^\pi=0^-$ bands, three $K^\pi=1^-$ bands and one $K^\pi=3^-$ band. They are shown in Fig.13 together with the calculated B(E2)

values. For comparison, Fig.13 contains also the energy spectra of ^{12}C.

(I) The $K^\pi=0^+_I$, 0^+_{II}, 1^-_{II} and 3^-_I bands

With the Λ particle mainly in the $(0s)_\Lambda$ state, we obtain these four bands, where the 3α part is similar to the $k^\pi=0^+_1$, 0^+_2, 1^-_1 and 3^-_1 bands, respectively, of the isolated 3α system. Thus we could call them the ^{12}C-analogue bands. In order to see the effects of channel couplings, the energy eigenvalues obtained with (without) channel couplings are given in Table III.

i) The $K^\pi=0^+_I$ ground band

The main channel of this band is the $(\ell,\lambda)_L=(L,0)_L$ with 98% channel probability. The energy gain due to the couplings with the other channels is only 0.4 MeV. The separation energy of the α particle in $^{13}_\Lambda C$ is about 13 MeV, which is much larger than the value of about 7 MeV in ^{12}C. This stabilization is caused by an additional Λ-3α interaction. A similar energy gain is obtained for the 2^+_I and 4^+_I members. Then the 4^+_I state becomes stable against the α-decay, though this level may have a small Λ-decay width due to its appearance at about 2 MeV above the $\Lambda+^{12}C$(g.s.) threshold.

The calculated r.m.s. radii $\sqrt{\langle r^2\rangle}_{3\alpha}$ and $\sqrt{\langle R^2\rangle}_{3\alpha-\Lambda}$ of $^{13}_\Lambda C$ as well as $\sqrt{\langle r^2\rangle}_{3\alpha}$ of ^{12}C are displayed in Table IV. We see only a slight contraction of $\sqrt{\langle r^2\rangle}_{3\alpha}$ of $^{13}_\Lambda C(K^\pi=0^+_I)$ compared with that of $^{12}C(k^\pi=0^+_1)$. This contraction reduces the intra-band B(E2) values in $^{13}_\Lambda C$ (see Fig.11 and 13). In the $^{9}_\Lambda Be$ case, such

reduction of B(E2) is rather drastic as emphasized in Ref.37), 38) and 40), while it is not so remarkable in the present ${}^{13}_{\Lambda}C$ ground band, reflecting its compact shell-model-like structure. More significant change should be seen in the ${}^{13}_{\Lambda}C$ excited states.

The obtained 0^+_I and 2^+_I states have good correspondences to the first and second peaks, respectively, in the excitation function of the forward ${}^{13}C(K^-,\pi^-){}^{13}_{\Lambda}C$ reaction[13].

ii) The $K^\pi=0^+_{II}$ band

The dominant component is the $\left[{}^{12}C(k^\pi=0^+_2)\otimes(0s)_\Lambda \right]$ intrinsic configuration with 70-79 % probability. The largest mixing comes from the coupling with the $\left[{}^{12}C(k^\pi=0^+_1)\otimes(1s.0d)_\Lambda \right]$ configuration, which amounts to almost 14 %. Thus the energy gain due to the channel couplings is large, about 1.5 MeV.

The ${}^{12}C(k^\pi=0^+_2)$ band states are characterized by the loosely coupled 3α intrinsic structure and hence an extended density distribution as seen in Fig.12. We find in Table IV that the addition of Λ leads to a cosiderable reduction of $\sqrt{\langle r^2\rangle}_{3\alpha}$ (3.48∿3.62 fm from 3.55∿3.91 fm) and a significant extension of $\sqrt{\langle R^2\rangle}_{3\alpha-\Lambda}$ (3.24∿3.70 fm) compared with the ground $K^\pi=0^+_I$ band (2.07∿2.17 fm). The intra-band B(E2) value is reduced to even half, in contrast to the very small reduction in the case of the ground band, but still remains fifteen times as large as the $B(E2;\ 2^+_1 \to 0^+_1)$ value.

The binding energy of Λ-${}^{12}C(0^+_1)$ in the ground state is as large as 11 MeV, while that of Λ-${}^{12}C(0^+_2)$ in the $L^\pi=0^+_{II}$ state is only 4 MeV, thus making the excitation energy of the 0^+_{II} state

twice as high as the corresponding one in ^{12}C. As described above, this is due to the drastic difference of the folding potentials for Λ-$^{12}C(0_1^+)$ and Λ-$^{12}C(0_2^+)$ (see Fig.12). This striking distinction of the potential forms causes the difference of binding energy and $\sqrt{\langle R^2\rangle}_{3\alpha-\Lambda}$ between the $L^\pi=0_I^+$ and 0_{II}^+ states.

iii) The $K^\pi=1_{II}^-$ band

The wf of the band head $L^\pi=1_{II}^-$ state with the 17.5 MeV excitaion energy is given by

$$|L^\pi=1_{II}^-\rangle=\sqrt{0.665}\left[\ ^{12}C(1_1^-)\otimes s_\Lambda\ \right]+\sqrt{0.239}\left[\ ^{12}C(2_1^+)\otimes p_\Lambda\ \right]+\cdots \quad (3.23)$$

The component of the $\left[\ ^{12}C(2_1^+)\otimes p_\Lambda\ \right]$ configuration is quite large but that of the $\left[\ ^{12}C(0_1^+)\otimes p_\Lambda\ \right]$ is very small ($\sim$1.5 %). The reason of this is following : Among the three configurations $\left[\ ^{12}C(0_1^+)\otimes p_\Lambda\ \right]$, $\left[\ ^{12}C(2_1^+)\otimes p_\Lambda\ \right]$ and $\left[\ ^{12}C(1_1^-)\otimes s_\Lambda\ \right]$, the first one is separated from the others in energy, while the latter two are approximately degenerate in energy. The second one is located at $Ex(p_\Lambda) + Ex(2_1^+) = 12.6 + 4.4 = 17.0$ MeV excitation, while the last one at $Ex(1_1^-) + \Delta\varepsilon = 10.8 + \Delta\varepsilon$, where $\Delta\varepsilon$ is the difference between s_Λ binding energies due to the $^{12}C(0_1^+)$-Λ and $^{12}C(1_1^-)$-Λ folding potentials. See Fig.14 showing the relevant diagonal potentials. The $^{12}C(1_1^-)$ state provides a potential shallower than $^{12}C(0_1^+)$ and hence gives a sizable positive value $\sim$ 7 MeV for $\Delta\varepsilon$. This is again explained by the compact (0_1^+) and non-compact (1_1^-) structures.

iv) The $K^\pi=3_I^-$ band

The band head $L^{\pi}=3^{-}_{I}$ state is characterized by the $\left[{}^{12}C(3^{-}_{1})\otimes s_{\Lambda} \right]$ configuration with 98 % channel probability. Thus the r.m.s. radius $\sqrt{\langle r^2\rangle}_{3\alpha}$ is almost the same as the ${}^{12}C(3^{-}_{1})$ state. It is interesting to compare the $L^{\pi}=3^{-}_{I}$ state with the ground $L^{\pi}=0^{+}_{I}$ state. The $\sqrt{\langle R^2\rangle}_{3\alpha-\Lambda}$ value of this state is considerably larger than that of the ground state ${}^{13}_{\Lambda}C(0^{+}_{I})$ and in between those of ${}^{13}_{\Lambda}C(0^{+}_{I})$ and ${}^{13}_{\Lambda}C(0^{+}_{II})$ (see Table IV). The binding energy of $\Lambda+{}^{12}C(3^{-}_{1})$ in the $L^{\pi}=3^{-}_{I}$ state is about 7 MeV, while that of $\Lambda+{}^{12}C(0^{+}_{1})$ in the $L^{\pi}=0^{+}_{I}$ state is about 11 MeV. The energy splitting between the 0^{+}_{1} and 3^{-}_{1} states in ${}^{12}C$, which constitute an inversion doublet[52], is about 10 MeV, and therefore that in ${}^{13}_{\Lambda}C$ is now about 14 MeV. This is due to the significant difference between the folding potentials for $\Lambda-{}^{12}C(3^{-}_{1})$ and $\Lambda-{}^{12}C(0^{+}_{1})$ as already seen in Fig.12.

(II) The $K^{\pi}=1^{-}_{I}$, 0^{-}_{I} and $K^{\pi}=1^{-}_{III}$, 0^{-}_{II} bands

The excitation of the Λ particle to $(0p)_{\Lambda}$-orbit leads to the formation of the four bands, where the $K^{\pi}=1^{-}_{I}$, 0^{-}_{I} bands and the $K^{\pi}=1^{-}_{III}$, 0^{-}_{II} bands are dominated by the $k^{\pi}=0^{+}_{1}$ and $k^{\pi}=0^{+}_{2}$ nuclear parts, respectively. The $K^{\pi}=1^{-}$ and 0^{-} bands could be, respectively, identified with the intrinsic structures in which the $(0p)_{\Lambda}$-orbit is parallel ($K^{\pi}=1^{-}$) or perpendicular ($K^{\pi}=0^{-}$) to the 3α oblate deformation plane in the sense of the strong coupling picture.

i) The $K^{\pi}=1^{-}_{I}$ and 0^{-}_{I} bands

Since the ground band of ${}^{12}C$ has an oblate deformation, the

$K^\pi=1^-_I$ band appears at a lower energy than the $K^\pi=0^-_I$ one in contrast to the ${}^{9}_{\Lambda}$Be and ${}^{21}_{\Lambda}$Ne cases with prolate deformation. In the SU(3) shell-model limit they correspond to the $(\lambda\mu)=(14)^{K=1}_{L=1,2,3,4,5}$ and $(03)^{K=0}_{L=1,3}$, respectively, constructed from $(04)\otimes(10)$[59].

Reflecting the structure of the main configuration $\left[\ {}^{12}C(k^\pi=0^+_1)\otimes(0p)_\Lambda\ \right]$, the r.m.s. radii $\sqrt{\langle r^2\rangle}_{3\alpha}$'s do not show any noticeable difference from those of the ${}^{12}C$ ground band (see Table IV). The $\sqrt{\langle R^2\rangle}_{3\alpha-\Lambda}$ values are 3.2∿3.9 fm, which are relevant to the $(0p)_\Lambda$ wf.

The wf's of the $K^\pi=1^-_I$ and 0^-_I band head states ($L^\pi=1^-_I$ and 1^-_{III}, respectively) have the following main components :

$$|\ L^\pi=1^-_I\ \rangle = \sqrt{0.900}\left[\ {}^{12}C(0^+_1)\otimes p_\Lambda\ \right] - \sqrt{0.084}\left[\ {}^{12}C(2^+_1)\otimes p_\Lambda\ \right] + \cdots \quad (3.24)$$

$$|\ L^\pi=1^-_{III}\rangle = \sqrt{0.140}\left[\ {}^{12}C(0^+_1)\otimes p_\Lambda\ \right] + \sqrt{0.600}\left[\ {}^{12}C(2^+_1)\otimes p_\Lambda\ \right] + \sqrt{0.217}\left[\ {}^{12}C(1^-_1)\otimes s_\Lambda\ \right] + \cdots \quad (3.25)$$

As seen in Eq.(3.24) the $L^\pi=1^-_I$ state consists of the two $\left[\ {}^{12}C(0^+_1)\otimes p_\Lambda\ \right]$ and $\left[\ {}^{12}C(2^+_1)\otimes p_\Lambda\ \right]$ configurations coupled rather weakly. This is related to the energy difference (∿4.4 MeV) between ${}^{12}C(0^+_1)$ and ${}^{12}C(2^+_1)$ states and a folding potential for Λ-${}^{12}C(2^+_1)$ shallower than that for Λ-${}^{12}C(0^+_1)$ (see Fig.14), of which the difference is due to the oblate deformation of ${}^{12}C$. (Relation between the strong and weak couplings is discussed in Ref.59)). In the case of the $L^\pi=1^-_{III}$ state, however, the mixing of the $\left[\ {}^{12}C(1^-_1)\otimes s_\Lambda\ \right]$ component is quite large (∿22 %). This is caused by the same reason as discussed in iii) of (I). These two

$L^{\pi}=1^{-}_{I}$ and 1^{-}_{III} states with the substitutional components correspond to the third and fourth peaks, respectively, which are experimentally observed in the excitation function of the forward $^{13}C(K^{-},\pi^{-})^{13}_{\Lambda}C$ reactions[13] :

$$L^{\pi}=1^{-}_{I} \quad ; \quad E_x^{cal}= 11.5 \text{ MeV} \quad vs. \quad E_x^{exp}= 10.4 \text{ MeV}. \tag{3.26}$$

$$L^{\pi}=1^{-}_{III} \quad ; \quad E_x^{cal}= 18.0 \text{ MeV} \quad vs. \quad E_x^{exp}= 16.4 \text{ MeV}. \tag{3.27}$$

ii) The $K^{\pi}=1^{-}_{III}$ and 0^{-}_{II} bands

These bands are constructed mainly by the configuration with the 0p-state Λ particle and the $k^{\pi}=0^{+}_{2}$ band of 3α nuclear part. Reflecting the well-developed cluster structure of the $k^{\pi}=0^{+}_{2}$ band of ^{12}C, the r.m.s. radii $\sqrt{\langle r^2\rangle}_{3\alpha}$ and intra-band B(E2) values are larger than those of the $K^{\pi}=1^{-}_{I}$ and 0^{-}_{I} bands.

The wf's of the $K^{\pi}=1^{-}_{III}$ band head $L^{\pi}=1^{-}_{IV}$ state and $K^{\pi}=0^{-}_{II}$ band head $L^{\pi}=1^{-}_{VI}$ state are written by

$$|\, L^{\pi}=1^{-}_{IV} \rangle = \sqrt{0.592}\left\{ {}^{12}C(0^{+}_{2})\otimes p_{\Lambda} \right\} - \sqrt{0.229}\left\{ {}^{12}C(2^{+}_{2})\otimes p_{\Lambda} \right\} + .. \tag{3.28}$$

$$|\, L^{\pi}=1^{-}_{VI} \rangle = \sqrt{0.270}\left\{ {}^{12}C(0^{+}_{2})\otimes p_{\Lambda} \right\} + \sqrt{0.672}\left\{ {}^{12}C(2^{+}_{2})\otimes p_{\Lambda} \right\} + .. \tag{3.29}$$

In contrast to the case of the $K^{\pi}=1^{-}_{I}$ and 0^{-}_{I} bands, the above two $L^{\pi}=1^{-}$ states are described by the $\left\{ {}^{12}C(0^{+}_{2})\otimes p_{\Lambda} \right\}$ and $\left\{ {}^{12}C(2^{+}_{2})\otimes p_{\Lambda} \right\}$ configurations coupled strongly. The reason of this is following: The energy difference between the 0^{+}_{2} and 2^{+}_{2} states in ^{12}C is small ($\sim$2.7 MeV). As seen in Fig.15, the folding potential for Λ-$^{12}C(2^{+}_{2})$ is shallower at the central region but deeper and long-ranged at the surface region than that

for Λ-$^{12}C(0_2^+)$. Thus the eigenstates for Λ-$^{12}C(0_2^+)$ and Λ-$^{12}C(2_2^+)$ are approximately degenerate in energy. In addition, the coupling potential connecting $^{12}C(0_2^+)$ and $^{12}C(2_2^+)$ are quite strong as shown in Fig.15.

Since the $L^\pi=1^-_{IV}$ state is located around the top of the centrifugal barrier with respect to the Λ-$^{12}C(0_2^+)$ threshold, it may have a chance to become a quasi-bound state.

(III) The $K^\pi=0^+_{III}$ band

The coupling of Λ in the $(1s)_\Lambda$ state with the 3α nuclear core still remaining in the $k^\pi=0_1^+$ band produces this $K^\pi=0^+_{III}$ band. However, there is a remarkable amount of mixed component ($\sim$10 %) where the 3α part is excited to the $k^\pi=0_2^+$ band with Λ occupying s-state (mainly Os).

This band head $L^\pi=0^+_{III}$ state is located at 6.0 MeV above the Λ-$^{12}C(0_1^+)$ threshold but below the Λ+$^{12}C(0_2^+)$ threshold. It is hardly expected, however, that this state appears as a resonance due to the coupling with the Λ+$^{12}C(0_2^+)$ channel.

§4. Structure of $^{21}_{\Lambda}$Ne

This section is concentrated to study the structure of $^{21}_{\Lambda}$Ne by the microscopic $\alpha+^{16}$O+Λ cluster model[41),42)]. The microscopic $\alpha+^{16}$O cluster model[52)~55)] of ^{20}Ne is known to describe nicely the structure of the ground $K^{\pi}=0^{+}$ band, its parity-doublet partner $K^{\pi}=0^{-}$ band[53)] starting from 5.78 MeV excitation and the fourth $K^{\pi}=0^{+}$ band starting from 8.3 MeV excitation which is called as the higher nodal band, as shown in Fig.16. Note that the ground band has a shell-model-like structure characteristic with a considerable clustering, while the latter two bands have a well-developed cluster structure. The other bands shown in Fig.16 (the second and third $K^{\pi}=0^{+}$ bands, and the $K^{\pi}=2^{+}$ band) can only be described by taking into account the configuration of α plus excited ^{16}O cluster[52)]. A characteristic of $^{21}_{\Lambda}$Ne is the coupling between the positive and negative parity bands of the core nucleus which appear in the same energy region, while such a parity coupling is quite unimportant in p-shell hypernuclei.

4.1. Formulation of the microscopic $\alpha+^{16}$O+Λ cluster model

The total wave function (wf) Ψ_L of a $^{21}_{\Lambda}$Ne state with the orbital angular momentum L is expanded in terms of the generator coordinate (GC) basis $\Phi(\ell;d)$ for the $\alpha+^{16}$O relative part and the normalized harmonic oscillator (h.o.) wf $u_{n\lambda}(\vec{R})=u_{n\lambda}(R)\cdot Y_{\lambda}(\hat{R})$ with quanta $N=2n+\lambda$ for the $(\alpha+^{16}O)$-Λ relative part:

$$\Psi_L = \sum_{c,d,n} w_c(d,n) \left[\Phi(\ell;d)\otimes u_{n\lambda}(\vec{R}) \right]_L , \qquad (4.1)$$

where $w_c(d,n)$ is the expansion coefficient and $c=(\ell,\lambda)_L$ denotes a channel of the angular momentum coupling with $\vec{r}$ and $\vec{R}$ reffering to the α-^{16}O and (α+^{16}O)-Λ relative coordinates, respectively, as shown in Fig.17(a). The GC basis is expressed as

$$\Phi(\ell;d) = \sqrt{\binom{20}{4}^{-1}}\mathcal{A}'\Big\{ \phi(\alpha)\phi(^{16}\mathrm{O})\mathcal{Y}_\ell(r;d)Y_\ell(\hat{r}) \Big\} . \qquad (4.2)$$

Here, $\phi(\alpha)$ and $\phi(^{16}\mathrm{O})$ represent the internal wf's with h.o. $(0s)_N^4$ and $(0s)_N^4(0p)_N^{12}$ configurations, respectively, with the same nucleon size parameter ν_N, and the operator $\mathcal{A}'$ antisymmetrizes the nucleons belonging to different clusters. The wave packet $\mathcal{Y}_\ell(r;d)$ with the generator coordinate d specifying the relative α-^{16}O distance is given in Eq.(2.6) and is expanded in terms of the h.o. basis:

$$\mathcal{Y}_\ell(r;d) = \sum_n a_{n\ell}(d)\, u_{n\ell}(r) , \qquad (4.3)$$

$$a_{n\ell}(d) = (-)^n \sqrt{2}\,\pi^{3/4} \Big[\Gamma(n+1)\,\Gamma(n+\ell+3/2) \Big]^{-1/2} \times (\sqrt{\nu_r/2}\, d)^{2n+\ell} \exp\Big\{ -(\sqrt{\nu_r/2}\, d)^2 \Big\} . \qquad (4.4)$$

All size parameters appearing in the following are chosen to give the same h.o. frequency Ω as for nucleons, for example,

$$\nu_r = \frac{16}{5}\nu_N , \quad \nu_R = \frac{20M_\Lambda}{20M_N+M_\Lambda}\nu_N , \qquad (4.5)$$

$$\nu_N = M_N\Omega / 2\hbar , \qquad (4.6)$$

where M_N (M_Λ) is the mass of nucleon (Λ particle).

The total Hamiltonian H of the α+^{16}O+Λ system can be written in the form of

$$H = H_N + T_\Lambda + V_{\Lambda N} , \tag{4.7}$$

$$H_N = \sum_{i=1}^{20} t_i^N + \sum_{i<j=1}^{20} v_{NN}(i;j) - T_G , \tag{4.8}$$

$$V_{\Lambda N} = \sum_{i=1}^{20} v_{\Lambda N}(\Lambda,i) , \tag{4.9}$$

where H_N is the internal Hamiltonian for the nuclear $\alpha+^{16}O$ part with the center-of-mass T_G subtracted, T_Λ the kinetic energy with respect to the $(\alpha+^{16}O)$-Λ relative coordinate $\vec{R}$, $V_{\Lambda N}$ the sum of Λ-N interactions.

The equation of motion is derived from the variational principle for the functional $\langle\Psi_L|H-E_L|\Psi_L\rangle$, and then we obtain a set of coupled-channel linear equations for the coefficient $w_c(d,n)$ in Eq.(4.1) :

$$\sum_{c_2,d_2,n_2} \Big\{ \Big(H_{\ell_1}(d_1,d_2) - E_L N_{\ell_1}(d_1,d_2) \Big) \delta_{c_1c_2}\delta_{n_1n_2} + T_{\lambda_1}(n_1,n_2) N_{\ell_1}(d_1,d_2)\delta_{c_1c_2} + U_L(c_1d_1n_1;c_2d_2n_2) \Big\} w_{c_2}(d_2,n_2) = 0, \tag{4.10}$$

with the normalization condition of

$$\sum_{c,d_1,d_2,n} w_c(d_1,n)\, N_\ell(d_1,d_2)\, w_c(d_2,n) = 1 . \tag{4.11}$$

The matrix elements in Eq.(4.10) are defined by

$$\begin{pmatrix} H_\ell(d_1,d_2) \\ N_\ell(d_1,d_2) \end{pmatrix} = \langle \Phi(\ell;d_1) | \begin{pmatrix} H_N \\ 1 \end{pmatrix} | \Phi(\ell;d_2) \rangle , \tag{4.12}$$

$$T_\lambda(n_1,n_2) = \langle u_{n_1\lambda}(\vec{R}) \mid T_\Lambda \mid u_{n_2\lambda}(\vec{R}) \rangle , \tag{4.13}$$

$$U_L(c_1d_1n_1;c_2d_2n_2)=\langle u_{n_1\lambda_1}(R)|U_L(R;c_1d_1,c_2d_2)|u_{n_2\lambda_2}(R)\rangle, \quad (4.14)$$

where $U_L(R;c_1d_1,c_2d_2)$ is the folding potential between the Λ particle and the $\alpha+^{16}O$ nucleus , which is defined by

$$U_L(R;c_1d_1,c_2d_2)=\langle\left[\Phi(\ell_1;d_1)\otimes Y_{\lambda_1}(\hat{R})\right]|V_{\Lambda N}|\left[\Phi(\ell_2;d_2)\otimes Y_{\lambda_2}(\hat{R})\right]\rangle. \quad (4.15)$$

The channel coupling in Eq.(4.10) is induced by U_L, whose explicit expression is given in Appendix C for the Λ-N interaction with the Gaussian type.

For later discussion we introduce here the channel probability and the h.o. state probability in a channel defined by

$$W_c^2 = \sum_{d_1,d_2,n} w_c(d_1,n)\, N_\ell(d_1,d_2)\, w_c(d_2,n) , \quad (4.16)$$

$$W_c^2(n) = \sum_{d_1,d_2} w_c(d_1,n)\, N_\ell(d_1,d_2)\, w_c(d_2,n)/W_c^2 , \quad (4.17)$$

respectively, where $\sum_c W_c^2 = 1$. From these quantities, we can see what channels and what components are important in a noted hypernuclear state of $^{21}_{\Lambda}Ne$.

4.2. Expressions of various physical quantities

4.2.1. Electric quadrupole transition probability

The electric quadrupole transition operator can be effectively expressed as

$$M(E2) = \frac{e}{2}\left[\, Q(\alpha+^{16}O) + Q(\Lambda)\,\right] , \quad (4.18)$$

where $Q(\alpha+^{16}O)$ and $Q(\Lambda)$ are the mass quadrupole operators for

$\alpha+^{16}O$ nuclear part and its recoil effect,

$$Q(\alpha+^{16}O) = \frac{5}{16} r^2 Y_2(r) + Q^{int}(\alpha) + Q^{int}(^{16}O) , \quad (4.19)$$

$$Q(\Lambda) = \frac{20M_N^2}{(20M_N+M_\Lambda)^2} R^2 Y_2(R) . \quad (4.20)$$

The explicit expression of the reduced E2 transition probability B(E2) is given in Appendix D. Note that the contributions of Q^{int} vanish due to the closed shell configuration assumed for α and ^{16}O.

4.2.2. Root mean square (r.m.s.) radii

The r.m.s. radii $\sqrt{\langle r^2\rangle}$ and $\sqrt{\langle R^2\rangle}$ for the relative coordinates shown in Fig.17(a) are expressed by

$$\langle\Psi_L|r^2|\Psi_L\rangle = \sum_{c,k,d_1,d_2} w_c(d_1,k)\, w_c(d_2,k) \times \sum_{n_1,n_2} a_{n_1\ell}(d_1)\, a_{n_2\ell}(d_2)\, \mu_N \langle u_{n_1\ell}(r)|r^2|u_{n_2\ell}(r)\rangle, \quad (4.21)$$

$$\langle\Psi_L|R^2|\Psi_L\rangle = \sum_{c,d_1,d_2,k_1,k_2} w_c(d_1,k_1)\, N_\ell(d_1,d_2)\, w_c(d_2,k_2), \times \langle u_{k_1\lambda}(R)|R^2|u_{k_2\lambda}(R)\rangle . \quad (4.22)$$

The coefficient μ_N in Eq.(4.21) is the eigenvalue of the norm kernel defined by

$$\langle\phi(\alpha)\phi(^{16}O)|\mathcal{A}'\left\{\phi(\alpha)\phi(^{16}O)u_{n\ell}(\vec{r})\right\}\rangle = \mu_N\, u_{n\ell}(\vec{r}) , \quad (4.23)$$

with $N=2n+\ell$ and expressed as

$$\mu_N = \sum_{q=0}^{4} \binom{4}{q} (-)^q \sum_{r=0}^{q} \binom{q}{r} \theta(N-r) \frac{N!}{(N-r)!} \left(1 - \frac{5}{16}q\right)^{N-r}, \quad (4.24)$$

where $\theta(x)=1$ for $x\geq 0$ and 0 for $x<0$. The notation $N<$ in Eq.(4.21) represents the smaller value of $N_i (i=1,2)$.

4.2.3. Reduced width amplitudes (RWA) and spectroscopic factors

We consider the following four kinds of two-body decay channels with low-energy threshold and the corresponding widths are deduced by the separation method[65),66)].

a) $\alpha+{}^{17}_{\Lambda}O(s)$ and $\alpha+{}^{17}_{\Lambda}O(p)$ channels

The $\alpha+{}^{17}_{\Lambda}O$ RWA's with Λ particle occupying the lowest s or p orbit are defined by

$$Y^{L}_{sL}(\rho) = \sqrt{\binom{20}{4}}\ \rho\ \langle\phi(\alpha)\phi({}^{17}_{\Lambda}O(s))Y_L(\hat{\rho})|\Psi_L\rangle\ , \tag{4.25}$$

$$Y^{L}_{pL'}(\rho) = \sqrt{\binom{20}{4}}\ \rho\ \langle\phi(\alpha)\left[\phi({}^{17}_{\Lambda}O(p))Y_{L'}(\hat{\rho})\right]_L|\Psi_L\rangle\ , \tag{4.26}$$

where $\vec{\rho}$ is the relative coordinate between α and ${}^{17}_{\Lambda}O$ as shown in Fig.17(b). The internal wf of ${}^{17}_{\Lambda}O$ is given by

$$\phi({}^{17}_{\Lambda}O) = \phi({}^{16}O)\ \xi_{\ell_\Lambda}(\eta)\ Y_{\ell_\Lambda}(\hat{\eta}) \quad (\ell_\Lambda=0,1)\ , \tag{4.27}$$

where the relative wf $\xi_\ell(\eta)$ is expanded in terms of h.o. basis:

$$\xi_\ell(\eta) = \sum_n c_n^{(\ell)}\ u_{n\ell}(\eta). \tag{4.28}$$

The coefficients $\{c_n^{(\ell)}\}$ are given in Table V.

The explicit expression of Eqs.(4.25) and (4.26) are given by

$$Y^{L}_{\ell_\Lambda L'}(\rho) = \sum_{c,d}\ \sum_{N_1,N_{31},N_{23}} w_c(d,N_1)\ a_{N_{23}\ell}(d)\ c^{(\ell_\Lambda)}_{N_{31}}\ \mu_{N_{23}} \tag{4.29}$$

$$\times \sum_{N_2=N_1+N_{21}-N_{31}} \langle N_{31}\ell_\Lambda(\vec{\eta}), N_2L'(\vec{\rho}) | N_{23}\ell(\vec{r}), N_1\lambda(\vec{R})\rangle_L \rho u_{N_2L'}(\rho),$$

where we employ the notation of the h.o. quantum number $(N=2n+\ell,\ell)$ in place of (n,ℓ), and $\langle|\rangle$ indicates the h.o. Moshinsky bracket for the coordinate transformation from the coordinate system in Fig.17(a) to that in Fig.17(b). Note that, for the $\alpha+{}^{17}_{\Lambda}O(p)$ decay from a natural parity state (L) of ${}^{21}_{\Lambda}Ne$, the angular momentum L' takes the values of $L\pm1$ because of the parity conservation, while, for an unnatural parity state, the L' is restricted to L. The spectroscopic factor S^2 is defined by the norm $Y^L_{\ell\,\Lambda L'}(\rho)$,

$$S^2 = \int_0^\infty d\rho \, \{Y^L_{\ell\,\Lambda L'}(\rho)\}^2 \ . \tag{4.30}$$

b) ${}^{5}_{\Lambda}He+{}^{16}O$ channel

The ${}^{5}_{\Lambda}He+{}^{16}O$ reduced width amplitude is expressed by

$$Y_L(Z) = \sqrt{\binom{20}{4}} \ Z\langle\phi({}^{5}_{\Lambda}He)\phi({}^{16}O)Y_L(\hat{Z})|\Psi_L\rangle \ . \tag{4.31}$$

$$= \sum_{c,d} \sum_{N_1,N_{12},N_{23}} w_c(d,N_1) \ a_{N_{23}\ell}(d) \ c_{N_{12}} \ \mu_{N_{23}} \tag{4.32}$$

$$\times \sum_{N_3=N_1+N_{23}-N_{12}} \langle N_{12}O(\vec{x}), N_3L\,(\vec{Z})|N_{23}\ell(\vec{r}), N_1\lambda(\vec{R})\rangle_L Z \ u_{N_3L}(Z),$$

where the $\langle|\rangle$ is the h.o. Moshinsky bracket between the coordinate systems shown in Fig.17(a) and (b). The coefficients $\{c_N\}$ in Eq.(4.32) are obtained by expanding the Λ-α relative wf

in terms of the h.o. basis, which are given in Table V. It should be noted , however, that the Λ-α folding potential is obtained by adopting the α-cluster wf with an appropriate nucleon size parameter ν_N=0.511 fm^{-2} (ν_N=1/2b_N^2, b_N=1.358 fm).

c) ^{20}Ne(ℓ)+Λ channel

The RWA of ^{20}Ne(ℓ)+Λ channel is given by

$$Y^L_{\ell\lambda}(R) = R \left\langle \left[\Phi(^{20}\mathrm{Ne}(\ell)) Y_\lambda(R) \right]_L | \Psi_L \right\rangle , \tag{4.33}$$

$$= \sum_{c,d,d',n} w_c(d,n)\, N_\ell(d,d')\, f_\ell(d')\, R\, u_{n\lambda}(R). \tag{4.34}$$

The free ^{20}Ne wf $\Phi(^{20}\mathrm{Ne}(\ell))$ is described by the microscopic α+^{16}O cluster model and expressed by

$$\Phi(^{20}\mathrm{Ne}(\ell)) = \sum_d f_\ell(d)\, \Phi(\ell;d), \tag{4.35}$$

where $\Phi(\ell;d)$ is given in Eq.(4.2).

4.3. Model space and two-body interactions

Our model space is specified by the channel of angular momentum coupling $c=(\ell,\lambda)_L$, the α-^{16}O relative distance parameter d and the (α+^{16}O)-Λ h.o. quanta ($N=2n+\lambda,\lambda$). In the present calculation, we make the following truncation of the model space, which are found to be enough to describe the low-lying states of $^{21}_{\Lambda}$Ne:

(I) the α-^{16}O orbital angular momenta

ℓ=0,2,4,6,8, for $K^\pi=0^+$ and ℓ=1,3,5,7,9 for $K^\pi=0^-$,

(II) the generator coordinate mesh points

d=1.2, 2.4, 3.6, 4.8, 6.0 fm ,

(III) the $(\alpha+^{16}O)$-Λ h.o. quanta

$N=2n+\lambda$ with $n=0,1,2,.....,9$ and $\lambda^{\pi}=0^{+},1^{-},2^{+},3^{-},4^{+}$.

As the two-body N-N interaction we employ the Volkov No.2 (2-range Gaussian) potential[57] with Majonara parameter $m_{NN}=0.62$. The h.o. size parameter for nucleons in the α- and ^{16}O-cluster is fixed to $\nu_N=0.160$ fm^{-2} ($\nu_N=1/2b_N^2$, $b_N=1.77$ fm). The Coulomb interaction is treated exactly by the computational method developed by Tohsaki-Suzuki[67] for the GCM-RGM calculation. This choice of parameters leads to a succesfull reproduction of the energies and other properties of the observed $K^{\pi}=0_1^{+}$, 0_1^{-} and 0_2^{+} (experimentally forth $K^{\pi}=0_4^{+}$) bands of ^{20}Ne (see Fig.16)[52)~55)].

The two-body Λ-N interaction is simply chosen as a Gaussian form with the range $\beta_{\Lambda N}=1.034$ fm (equivalent to the two-pion exchange Yukawa form) and the strength $v^{o}_{\Lambda N}=-38.0$ MeV. By solving the ^{16}O-Λ problem with the folding model, the strength $v^{o}_{\Lambda N}$ is determined so as to reproduce the Λ binding energy in $^{17}_{\Lambda}O$ given by the empirical formula[2] $B_{\Lambda}=(27.0-81.9A^{-2/3})\pm1.5$ MeV, where A is the baryon number.

The main component of the obtained bands of $^{21}_{\Lambda}Ne(K^{\pi})$ is labeled by $\left\{ k\otimes\lambda \right\}$, where k represents the intrinsic quantum number of the $\alpha+^{16}O$ nuclear part and λ a $(\alpha+^{16}O)$-Λ state.

4.4. Positive parity states

Figure 18 shows the calculated energy spectra and B(E2)

values of the positive parity states of $^{21}_{\Lambda}$Ne, which are able to be classified to seven bands, namely, six $K^{\pi}=0^{+}$ and one $K^{\pi}=1^{+}$ bands. In order to see the effects of the α-^{16}O parity couplings, there are given in Table VI the energies and channel probabilities for all seven band-head states obtained with (without) parity couplings.

i) The $K^{\pi}=0^{+}_{I}$ ground band

The main channel of this band is the $(\ell,\lambda)_{L}=(L,0)_{L}$ with 98% channel probability, and the energy gain due to the parity coupling is very small (about 0.3 MeV). The α+^{16}O nuclear part is similar to the ground band of the isolated α+^{16}O system and the Λ particle occupies mainly the $(0s)_{\Lambda}$ state. Thus this band is called as the "^{20}Ne-ground-band-analogue". The binding energy of Λ is about 17 MeV, which is much larger than the one in $^{17}_{\Lambda}$O (B_{Λ}=14.8 MeV), and the separation energy of the α particle in $^{21}_{\Lambda}$Ne is about 7.5 MeV, which is also much larger than the one in ^{20}Ne (B_{α}=4.5MeV). These energy stabilization are due to the additional Λ-(α+^{16}O) interaction, and make the 6^{+}_{I} member a bound state which is unbound in ^{20}Ne.

The moment of inertia extracted from the energy spectrum is almost the same as that of the α+^{16}O ground band. This does not simply mean that the α-^{16}O distance is unchanged. The calculated r.m.s. radii $\sqrt{\langle r^2\rangle}$ are displayed in Fig.19. We see a certain contraction of $\sqrt{\langle r^2\rangle}$ in $^{21}_{\Lambda}$Ne ($K^{\pi}=0^{+}_{I}$) compared with that in ^{20}Ne($K^{\pi}=0^{+}_{1}$). This contraction sizably reduces the intra-band B(E2) values in $^{21}_{\Lambda}$Ne as shown in Fig.18.

The reduced width amplitudes (RWA) and their spectroscopic

factors for $\alpha+{}^{17}_{\Lambda}O$ and ${}^{5}_{\Lambda}He+{}^{16}O$ in ${}^{21}_{\Lambda}Ne(L=0)$ and for $\alpha+{}^{16}O$ in ${}^{20}Ne$ are shown in Fig.20 and Table VII. (The $S^2({}^{20}Ne+\Lambda)$-factor can be inferred from the channel probabilities W_c^2 in Table VI.) The overall behaviors of the three RWA's are common to all these cases, but an appreciable shrinkage of the outermost peak is seen in the former two in comparision with the latter one. Thus, the $S^2(\alpha+{}^{17}_{\Lambda}O(s))$-factors in ${}^{21}_{\Lambda}Ne(K^{\pi}=0^{+}_{I})$ are smaller than the $S^2(\alpha+{}^{16}O)$-factors in ${}^{20}Ne(K^{\pi}=0^{+}_{1})$. These facts reflect the energy stabilization and the contraction due to the Λ participation.

ii) The $K^{\pi}=0^{+}_{II}$ band

This band has the dominant channel $(\ell,\lambda)_L=(L,0)_L$ of the $\left[(k^{\pi}=0^{+}_{2})\otimes 0s_{\Lambda}\right]$ configuration, and therefore is analogous to the higher nodal band in ${}^{20}Ne$ [52)~55)]. The parity coupling, however, is considerably strong: For example, the $(\ell,\lambda)=(1,1)$ channel probability is about 18%, and the energy gain due to the parity coupling amounts to 2.1 MeV as shown in Table VI.

Figure 20 shows that the $\alpha+{}^{17}_{\Lambda}O$ and ${}^{5}_{\Lambda}He+{}^{16}O$ RWA's of the 0^{+}_{II} state have one more node than those of the 0^{+}_{I} ground state and extend to the outer region, which manifests a developed-cluster structure. Reflecting the structure characteristic, the B(E2) values of the intra-band transition are more than five times as large as those of the ground band, and simultaneously the r.m.s. radius $\sqrt{\langle r^2\rangle}$ is about 5.5~6.0 fm which is larger than that of the $K^{\pi}=0^{+}_{I}$ band ($\sqrt{\langle r^2\rangle}$=3.4~3.8 fm) (see Fig.19). Another remarkable point is the distinct increase of the spectroscopic factors $S^2(\alpha+{}^{17}_{\Lambda}O(p))$ as seen in Table VII. These results are caused by

the activation of the α-^{16}O relative vibrational mode.

It is interesting to compare the $K^{\pi}=0^{+}_{II}$ band in $^{21}_{\Lambda}Ne$ with the corresponding $K^{\pi}=0^{+}_{2}$ band in ^{20}Ne. In ^{20}Ne the higher nodal 0^{+}_{2} state has a large α-decay width since it is located at 3.6 MeV above the α+^{16}O threshold, which is just on the top of the Coulomb barrier. The corresponding higher nodal state (0^{+}_{II}) in $^{21}_{\Lambda}Ne$, however, comes down to the energy of about 2 MeV lower than the top of the barrier, and therefore has very small penetrability. This different situation results in the fact that the RWA of $^{21}_{\Lambda}Ne(0^{+}_{II})$ damps in outer region faster than that of $^{20}Ne(0^{+}_{2})$ as seen in Fig.20. The α-decay width is estimated by employing the separation energy method[65),66)] and given in Table VIII. Considering that the ^{20}Ne higher nodal states are a very rare realization of the "nuclear di-molecular vibrational mode", its further stabilization in $^{21}_{\Lambda}Ne$ is worth while to be noted.

iii) The $K^{\pi}=0^{+}_{III}$ band

In the dominant channel $(\ell,\lambda)_{L}=(L,0)_{L}$, the α-^{16}O relative wf has two more nodes than the ground band with the Λ particle occupying $(0s)_{\Lambda}$ state. The band head state 0^{+}_{III} appears at the energy lower than the Λ+^{20}Ne threshold but remarkably higher than the potential barrier with respect to the α+$^{17}_{\Lambda}O$ one. Under the present bound state approximation, it seems inadequate to discuss about the properties of this band further. Whether such higher vibrational states appear in this energy region as definite resonances, however, is an interesting problem.

iv) The $K^{\pi}=0^{+}_{IV}$ and 1^{+} bands

The dominant configuration $\left[(k^{\pi}=0_1^-)\otimes 0p_{\Lambda}\right]$ characterizes these two bands, which are respectively identified with the intrinsic structure where the 0p-orbital is parallel (K=0) or perpendicular (K=1) to the $\alpha+^{16}O$ symmetry axis in the molecular orbital terminology. In the SU(3) classification they correspond to the $(\lambda,\mu)=(10,0)^{K=0}_{L=0,2,\ldots,10}$ and $(8,1)^{K=1}_{L=1,2,\ldots,9}$ constructed from $(9,0)\otimes(1,0)$. The calculated B(E2) values reveal this strong coupling type two-band structure.

Another feature of the $K^{\pi}=0^+_{IV}$ band is a large admixture of the $\left[(k^{\pi}=0_1^+)\otimes(1s.0d)_{\Lambda}\right]$ configuration (see Table VI). The calculated spectroscopic factors given in Table VII indicate that these two configurations are admixed in such a way that $S^2(^5_{\Lambda}He+^{16}O)$ are enhanced in $K^{\pi}=0^+_{IV}$ and reduced in $K^{\pi}=0^+_{V}$ and 0^+_{VI}. In fact the $S^2(^5_{\Lambda}He+^{16}O)$ factors of the $K^{\pi}=0^+_{IV}$ band is much larger than those of other bands. This fact is interpreted that the $K^{\pi}=0^+_{IV}$ band has the configuration assigned in terms of the coordinate system in Fig.17(c) rather than that in Fig.17(a). The coupling between the above two configurations leads the structure that the Λ particle favors to go with $^5_{\Lambda}He$, not $^{17}_{\Lambda}O$. In the SU(3) (λ,μ) context this may by said as a linear combination of three (10,0)'s from (80)⊗(20), (90)⊗(10) and (10,0)⊗(00) of the $\alpha-^{16}O$ and $(\alpha+^{16}O)-\Lambda$ relative wf's constitutes a new (10,0) made up from (00) for $\alpha-\Lambda$ and (10,0) for $^5_{\Lambda}He+^{16}O$. The actual situation of couplings depends on the energies of the configurations, which are determined by the energy splitting of the Λ states and the energy spectra of ^{20}Ne. All these dynamical interplays underlie our calculated results.

v) The $K^{\pi}=0^{+}_{V}$ and 0^{+}_{VI} bands

As discussed just above in iv), these bands are the counterpart of the $K^{\pi}=0^{+}_{IV}$ band and have the configuration of $\left[(k^{\pi}=0^{+}_{1})\otimes(1s.0d)_{\Lambda}\right]$ with a significant admixture of $\left[(k^{\pi}=0^{-}_{1})\otimes 0p_{\Lambda}\right]$. In the SU(3) (λ,μ) classification they correspond to $(\lambda,\mu)=(10,0)^{K=0}_{L=0,2,\ldots,10}$ and $(62)^{K=2}_{L=2,4,6}$, respectively, of which the latter comes from $(80)\otimes(20)=(10,0)+(81)+(62)$. Such a strong coupling picture is supported by the B(E2) values in Fig.18, although the obtained wf components are not really like those of the SU(3) (λ,μ).

As seen in Table VII, the S^{2}-factors for the three decay channels are very small, since the wf components effective for these channels have gone to the lower bands.

vi) The substitutional $L^{\pi}=1^{+}$ state

It is interesting to predict the energy of the state which is generated in the recoilless $(K^{-},\pi^{\pm})$ reaction by substituting a Λ particle for a valence nucleon in target ^{21}Ne (^{21}Na). Since the main component of the ^{21}Ne (^{21}Na) ground state is the SU(3) $(\lambda,\mu)=(81)^{K=1}_{L=1,2,\ldots,9}$ configuration, we predict in the present calculation that the $L^{\pi}=1^{+}$ state is found at the excitation energy of 22.1 MeV, i.e., $B_{\Lambda}=-4.8$ MeV.

4.5. Negative parity states

The calculated energy spectra and B(E2) values of negative parity states are shown in Fig.21. There are four rotational

bands, that is, three $K^\pi=0^-$ and one $K^\pi=1^-$, whose band head $L^\pi=1^-$ states lie below the $\Lambda+^{20}$Ne threshold. The reason why so many negative parity bands appear in the low-energy region are i) the existence of the negative parity $K^\pi=0^-$ band in ^{20}Ne starting from only 5.8 MeV excitation, ii) the small energy gap ($\sim$10 MeV) between the s- and p-state of Λ particle.

i) The $K^\pi=0^-_I$ band

This band has mainly the $\left[(k^\pi=0^-_1)\otimes 0s_\Lambda\right]$ configuration, and therefore could be called the "^{20}Ne $K^\pi=0^-_1$-band analogue". The band head 1^- state of ^{20}Ne is unstable for the α-decay since it appears at 1.05 MeV above the $\alpha+^{16}$O threshold, while the corresponding $L^\pi=1^-_I$ state of $^{21}_\Lambda$Ne is particle-stable because of its location at 1.16 MeV below the $\alpha+^{17}_\Lambda$O threshold. The $\alpha-^{16}$O parity coupling is considerably strong: For example, the $(\ell,\lambda)=(0,1)$ and $(2,1)$ channel probabilities are 5.1% and 8.4%, respectively, and the energy gain due to the parity coupling is 1.4 MeV as shown in Table IX. Thus, we understand that the strong parity coupling induced by the glue-like role of Λ makes the 1^-_I member a bound state.

The RWA's for the $\alpha+^{17}_\Lambda$O and $^5_\Lambda$He$+^{16}$O channels have very large amplitudes outside the outermost nodal point as seen in Fig.22. This indicates that the developed-cluster structure in the $K^\pi=0^-_1$ band of ^{20}Ne persists in $^{21}_\Lambda$Ne, although a shrinkage of the system is seen in the r.m.s. radii $\sqrt{\langle r^2\rangle}$ (Fig.19), the $S^2(\alpha+^{17}_\Lambda O(s))$-factors (Table X) and the intra-band B(E2) values (Fig.21).

ii) The $K^\pi=0^-_{II}$ and 1^- bands

These bands are constructed mainly by the $\left[(k^{\pi}=0_1^+)\otimes 0p_{\Lambda}\right]$ configuration, which again splits into the two strong coupling type bands. They correspond to the SU(3) limits, $(\lambda\mu)=(90)$ and (71), respectively.

The two bands lie above the α-decay threshold but their band head states appear below the other thresholds. The calculated α-decay widths are given in Table VIII. Those of the $K^{\pi}=0^-_{II}$ band are fairly large since the $S^2(\alpha+{}^{17}_{\Lambda}O)$-factors for this band are not small (see Table X). Some of the α-decays from the unnatural parity states of the $K^{\pi}=1^-$ band is forbidden because of the parity conservation.

iii) The $K^{\pi}=0^-_{III}$ band

The dominant configuration is $\left[(k^{\pi}=0_2^-)\otimes 0s_{\Lambda}\right]$ where the $\alpha+{}^{16}O$ part is the "negative parity higher nodal state". The admixture due to the parity coupling is remarkable (20%) and the associated energy gain amounts to 3.2 MeV. The strong couplings result in the fact that the $\left[(k^{\pi}=0_1^+)\otimes 0p_{\Lambda}\right]$ configuration is located close to the donimant configuration in energy. The band head energy is just around the top of the $\alpha+{}^{17}_{\Lambda}O$ Coulomb barrier, and therefore this situation is similar to that of the positive parity state in ${}^{20}Ne(\ell^{\pi}=0_2^+$, experimentally $0_4^+)$. The possible realization of this "negative parity higher nodal band" in ${}^{21}_{\Lambda}Ne$ which does not exist in ${}^{20}Ne$ is entirely due to the stabilization induced by the participation of Λ.

§5. Summary

We have studied the properties of $L^{\pi}=1^{-}$ resonance states found in the forward cross section of the $^{9}Be(K^{-},\pi^{-})^{9}_{\Lambda}Be$ reaction and the structures of $^{13}_{\Lambda}C$ and $^{21}_{\Lambda}Ne$ by the microscopic cluster model. The model is suitable to make realistic estimates and predictions of the particle-decay widths and electromagnetic transition probabilities as well as energy properties, since the model space covers wide-range shell-model space without the spurious center-of-mass excitation, and the antisymmetrization is taken into account properly. The obtained results exhibit various aspects characteristic of the hypernuclear structures, which are generated by the participation of Λ particle to core nuclei. We summarize main results and remarks.

Section 2 has been devoted to investigate the properties of high-lying $L^{\pi}=1^{-}_{2}$ resonance state of $^{9}_{\Lambda}Be$, which corresponds to the second peak ($E_{\Lambda}^{exp}\simeq 6.3$ MeV and $\Gamma^{exp}\simeq 7$-8 MeV) in the excitation function of the forward $^{9}Be(K^{-},\pi^{-})^{9}_{\Lambda}Be$ reaction. The coupled-channel scattering problem including the $^{5}_{\Lambda}He+\alpha$, $\Lambda+^{8}Be(0^{+})$ and $\Lambda+^{8}Be(2^{+})$ cluster configurations has been solved in order to estimate the energies and widths of $L^{\pi}=1^{-}$ states. We have found two resonance states by studying the energy dependence of the elastic and inelastic cross sections as well as the absolute values of S-matrix elements in the energy region up to about 15 MeV above the $^{5}_{\Lambda}He+\alpha$ threshold. A broad resonance state has been obtained at $E_{\Lambda}\simeq 6.0$ MeV with the width $\Gamma\simeq 6$ MeV in the inelastic cross section from the $\Lambda+^{8}Be(0^{+})$ to $\Lambda+^{8}Be(2^{+})$ channel, which is

identified as the $K^{\pi}=1^{-}$ band head $L^{\pi}=1^{-}_{2}$ state obtained under the bound state approximation (BSA). This resonance corresponds to the second peak observed in the $^{9}Be(K^{-},\pi^{-})^{9}_{\Lambda}Be$ reaction, and the energy and width are in good agreement with the experimental data. On the other hand, the microscopic $\alpha+\alpha+\Lambda$ cluster model under the BSA has predicted the $K^{\pi}=0^{-}$ band head $L^{\pi}=1^{-}_{1}$ state around $E_{\Lambda}\simeq 0$ MeV, which is called as "genuinely hypernuclear state". However, it has not been seen in the excitation function of the forward $^{9}Be(K^{-},\pi^{-})^{9}_{\Lambda}Be$ reaction since it might have small cross section and be hidden by the tail of the big peak observed at $E_{\Lambda}^{exp}\simeq 6.3$ MeV. The present investigation justifies the previous prediction obtained by the BSA treatment and furthermore predicts the 1^{-}_{1} resonance state at $E_{\Lambda}\simeq -0.2$ MeV with the width $\Gamma\simeq 2$ MeV which will be seen in the $^{5}_{\Lambda}He+\alpha$ elastic cross section.

The widths of the resonance states obtained by solving the above coupled-channel scattering problem, however, do not directly correspond to those in the excitation spectra of the forward $^{9}Be(K^{-},\pi^{-})^{9}_{\Lambda}Be$ reaction. In order to compare directly with the experimental data, the double differential cross section or the strength function of the $^{9}Be(K^{-},\pi^{-})^{9}_{\Lambda}Be$ reaction has been evaluated with the help of the distorted wave impulse approximation (DWIA) by employing the continuum-state $^{9}_{\Lambda}Be$ wf's. The wf's have been obtained by solving the three-channel coupled equation under the Kapur-Peierls-type outgoing wave boundary condition. Therefore, the particle-decay widths of continuum states of the $^{9}_{\Lambda}Be$ hypernucleus produced in the (K^{-},π^{-}) reaction have been taken into account in a natural way. The distorted

kaon and pion wf's have been calculated with the use of the eikonal approximation. The microscopic α+α+n cluster model wf has been employed as the ground state wf of the target ^{9}Be nucleus. We have obtained two peaks, a small peak at $E_{\Lambda}\simeq-0.5$ MeV with the width $\Gamma\simeq2$ MeV and a big peak at $E_{\Lambda}\simeq6.0$ MeV with the width $\Gamma\simeq6$ MeV, by studying the energy dependence of the strength function for p_{K^-} = 790 MeV/c and θ_{π^-} = 0° where the observation was done. The latter big peak corresponds to the second peak in the excitation function of the ^{9}Be$(K^-,\pi^-)^{9}_{\Lambda}$Be reaction and is in good agreement with the experimental data ($E_{\Lambda}^{exp}\simeq6.3$ MeV and $\Gamma^{exp}\simeq7$-8 MeV). The width of this peak comes from the decay into the $\Lambda+^{8}$Be$(0^+,2^+)$ channels. The lower small peak corresponds to the genuinely hypernuclear $L^{\pi}=1^-_1$ state, and the origin of the width of this peak (∿ 2 MeV) is mainly due to the α decay into the $^{5}_{\Lambda}$He+α channel. This state has not been observed because of the small cross section and large width in addition to the poor experimental resolution. It is hoped to be observed, however, if the coincidence experiments such as the ^{9}Be$(K^-,\pi^-\alpha)^{5}_{\Lambda}$He reaction are carried out in future.

In §3 and 4 the structures of $^{13}_{\Lambda}$C and $^{21}_{\Lambda}$Ne, which are the typical heavier p-shell and sd-shell hypernuclei, have been investigated by the microscopic 3α+Λ and α+^{16}O+Λ cluster models, respectively. Various physical quantities such as the B(E2) values, the root mean square (r.m.s.) radii, the reduced width amplitudes and the spectroscopic factors for two-body decay channels have been evaluated in order to study the structure characteristics. The obtained many states have been classified

into some rotational bands according to the underlying intrinsic structures which are characterized by the $k^{\pi}(3\alpha$ or $\alpha+{}^{16}O)$ and λ (Λ) as two building blocks. We have found many interesting aspects; a) coexistence of weak and strong coupling features, b) realizations of genuinely hypernuclear states with new symmetry, c) stabilization due to the glue-like role of Λ particle, d) appearance of many new bound and quasi-bound states. Some of them have already been found in the investigations of light p-shell hypernuclei. However, there appeared additional aspects characteristic of the heavy region, which do not appear in the light p-shell hypernuclei; for example, i) in ${}^{13}_{\Lambda}C$, the dynamical couplings between the Λ particle motions $((0s)_{\Lambda},(0p)_{\Lambda},(1s0d)_{\Lambda},..)$ and the two contrastive nuclear structures, that is, the shell-model-like structure and the loosely-coupled 3α cluster structure, ii) in ${}^{21}_{\Lambda}Ne$, the parity couplings induced by the addition of Λ, which connect the ground $K^{\pi}=0^{+}$ band with its parity-doublet partner $K^{\pi}=0^{-}$ band in ${}^{20}Ne$ since the energy gap between them is not large. We summarize the main results obtained in §3 and 4 as follwings:

——— ${}^{13}_{\Lambda}C$ hypernucleus ———

i) The folding potentials for Λ-${}^{12}C(0^{+}_{1},2^{+}_{1},4^{+}_{1})$ are deep and short-ranged, while those for Λ-${}^{12}C(0^{+}_{2},2^{+}_{2},1^{-}_{1})$ are shallow and long-ranged. The one for Λ-${}^{12}C(3^{-}_{1})$ has intermediate depth and range. These differences are due to the drastic dependence of the density distributions of ${}^{12}C$ on its states, induced by the α-clustering.

ii) Reflecting the drastic difference of the folding potentials for Λ-$^{12}C(0_1^+)$ and Λ-$^{12}C(0_2^+)$, the binding energy difference between the ground $L^\pi=0_I^+$ state and the $L^\pi=0_{II}^+$ state ($\sim$14 MeV) is twice as large as that of ^{12}C ($\sim$7 MeV). A similar situation occurs in the case of the $L^\pi=1_{II}^-$ or 3_I^- states.

iii) The intra-band B(E2) values and the r.m.s. radii $\sqrt{\langle r^2\rangle}_{3\alpha}$'s of the ground $K^\pi=0_I^+$ band with the dominant configuration $\left[^{12}C(k^\pi=0_1^+)\otimes(0s)_\Lambda\right]$ are almost same as those of the ^{12}C ground band. This indicates that the ^{12}C nuclear core part with the compact shell-model-like structure scarcely change in spite of the Λ participation.

iv) The first ($B_\Lambda^{exp}\simeq$11.3 MeV) and the second peaks ($B_\Lambda^{exp}\simeq$6.9 MeV) observed in the forward cross section of the $^{13}C(K^-,\pi^-)^{13}_\Lambda C$ reaction correspond well to the $L^\pi=0_I^+$ ($B_\Lambda^{cal}\simeq$11.3 MeV) and 2_I^+ ($B_\Lambda^{cal}\simeq$6.9 MeV) states of the $K^\pi=0_I^+$ ground band, respectively. Similarly, the $K^\pi=1_I^-$ band head $L^\pi=1_I^-$ ($B_\Lambda^{cal}\simeq$-0.1 MeV) and $K^\pi=0_I^-$ band head $L^\pi=1_{III}^-$ ($B_\Lambda^{cal}\simeq$-7.3 MeV) states have good correspondence to the third ($B_\Lambda^{exp}\simeq$-0.9 MeV) and the fourth ($B_\Lambda^{exp}\simeq$-5.1 MeV) peaks observed in the (K^-,π^-) reaction.

——— $^{21}_\Lambda$Ne hypernucleus ———

i) The Λ particle plays a glue-like role and induces a parity coupling to stabilize the system in energy; for example, the 6_I^+ member of the ground band and the band head 1_I^- state of the $K^\pi=0_I^-$ band newly become particle-stable, and the higher nodal ($K^\pi=0_{II}^+$) states come down below the $\alpha+^{17}_\Lambda$O potential barrier as the definite resonances with small widths ($\Gamma_\alpha^{cal}=0.7\sim0.8$ MeV). In

addition, a negative parity higher nodal band ($K^{\pi}=0^{-}_{III}$) may be realized, whose corresponding band in ^{20}Ne does not appear.

ii) The energy stabilization due to Λ participation reduces the intra-band E2-transition probability and the r.m.s. radii $\sqrt{\langle r^2\rangle}_{\alpha-^{16}O}$'s in comparision with those of ^{20}Ne. For example, the B(E2) values in the $^{21}_{\Lambda}$Ne ground band is half as large as those in the ^{20}Ne one.

iii) There is a strong coupling or admixture among the configurations which could be assigned the same (λμ) label in the shell-model limit. A typical case is the three (10,0)-like configurations which are constituted from (80)⊗(20), (90)⊗(10) and (10,0)⊗(00). They are coupled strongly and recombined so that each new (10,0) gives a large ($K^{\pi}=0^{+}_{IV}$) or small ($K^{\pi}=0^{+}_{III}$ and 0^{+}_{V}) $^{5}_{\Lambda}$He+^{16}O channel probability (spectroscopic factor).

iv) We predict that the substitutional state generated by the (K^{-},π) reaction on ^{21}Ne(^{21}Na) may be found at the excitation energy of 22.1 MeV, i.e., B_{Λ}=-4.8 MeV.

Before concluding this section, we give some remarks on the next step for the present investigations of light hypernuclei. As for the $^{9}_{\Lambda}$Be hypernucleus, there remains a problem of the biggest peak observed at $E_{\Lambda}\simeq$17 MeV in the excitation spectra of the ^{9}Be$(K^{-},\pi^{-})^{9}_{\Lambda}$Be reaction. This state is considered to be generated by the recoilless conversion of a neutron in the α clusters to a Λ particle. Therefore it can not be described by the α+α+Λ model. We are now studying the structure of this state by the microscopic (α+3N+N)+Λ cluster model. Since this model includes the space spanned by the microscopic α+α+Λ cluster

model, it can describe simultaneously not only the low-lying states of ${}^{9}_{\Lambda}$Be but also the high-lying ones (${}^{9}_{\Lambda}$Be*), and take into account the coupling between the configurations $\alpha+\alpha+\Lambda$ and $\alpha+\alpha^{*}+\Lambda$. As an application of this model, there is a structure study of the Σ-hypernucleus ${}^{9}_{\Sigma}$Be, which is observed in the (K^{-},π^{-}) reaction, by the microscopic $(\alpha+3N+N)+\Sigma$ cluster model. This investigation will give some solutions on the mysterious quenching mechanism of the narrow widths of Σ single-particle levels in spite of the large conversion width $\Sigma N \rightarrow \Lambda N$, since in this model the Σ particle-N hole interactions, which are considerably strong and expected to play an important role in the quenching mechanism, are taken into account in a natural way. Concerning the ${}^{13}_{\Lambda}$C and ${}^{21}_{\Lambda}$Ne hypernuclei, we need to make a realistic and quantitative estimate of the energies and widths of resonance states as in the ${}^{9}_{\Lambda}$Be case. These investigations enable us to not only make a analysis of existing data but also give reliable predictions.

Since the accurate and enough data for wide-range hypernuclei are necessary for the advancement of hypernuclear physics, we hope highly the further development of hypernuclear experiments and especially expect the results of experiments which will be perfomed at KEK.

Acknowledgements

The author is thankful to Professor S. Takagi for the valuable discussions, encouragements and careful reading through the manuscript. He would like to thank Professor T. Sawada, Dr. T. Ueda, Dr. K. Itonaga and other members of Department of Applied Mathematics, Faculty of Engineering Science, Osaka University, for the useful discussions and continuous encouragements.

He wishes to express his gratitudes to Professor K. Ikeda, Professor H. Bandō and Professor T. Motoba for many valuable discussions, helpful advices and continuous encouragements. He is indebted to them for collaboration of a series of his works. He is also thankful to Professor M. Kamimura for collaboration on the ${}^{13}_{\Lambda}\mathrm{C}$ problem.

The computer calculation for this work has been financially supported in part by Research Center for Nuclear Physics, Osaka University. Numerical computations were carried out at the Data Processing Centers of Osaka University and Kyoto University.

Appendix A

In this Appendix we present the expressions of the overlap and Hamiltonian kernels pertinent to the generator coordinate method (GCM) applied to the ${}^{5}_{\Lambda}$He+α and Λ+^{8}Be configurations with ${}^{5}_{\Lambda}$He and ^{8}Be consisting of α+Λ and α+α, respectively.

The basis wf's for Eqs. (2.2)∿(2.4) are written as

$$\Phi^{c_1}_{\ell_1\lambda_1 L}(d_1;D_1) = \sqrt{\frac{4!4!}{8!}}\,\mathcal{A}'\Big\{\,\phi(\alpha)\varphi_{\ell_1}(\eta;d_1)Y_{\ell_1}(\hat{\eta}) \times \phi(\alpha)\,\varphi_{\lambda_1}(R_1;D_1)Y_{\lambda_1}(\hat{R}_1)\,\Big\}_L\,, \quad (A.1)$$

$$\Phi^{c_2}_{\ell_2\lambda_2 L}(d_2;D_2) = \Big\{\,\frac{1}{\sqrt{2}}\sqrt{\frac{4!4!}{8!}}\,\mathcal{A}'\{\phi(\alpha)\phi(\alpha)\varphi_{\ell_2}(r;d_2)Y_{\ell_2}(\hat{r})\} \times \varphi_{\lambda_2}(R_2;D_2)Y_{\lambda_2}(\hat{R}_2)\,\Big\}_L\,, \quad (A.2)$$

where c_1 and c_2 denote the ${}^{5}_{\Lambda}$He(α+Λ)+α and Λ+^{8}Be(α+α) channels, respectively. The kinetic energy and interaction operators are defined by Eqs. (2.12)∿(2.14). The N-N interaction used is of the form

$$v_{NN}(r) = v^0_{NN}\exp\{-(r/\beta_{NN})^2\}\ (\ W + BP_\sigma - HP_\tau - MP_\sigma P_\tau\ ). \quad (A.3)$$

In addition, the following quantities are defined :

$$q = b_N^2/\Big[2(\beta_{NN}^2+2b_N^2)\Big],\quad \gamma_\Lambda = b_N^2/\Big[2(\beta_{\Lambda N}^2+(1+M_N/M_\Lambda)b_N^2)\Big],$$

$$V_d = v^0_{NN}(2q\beta_{NN}^2/b_N^2)^{3/2}\ (8W+4B-4H-2M),$$

$$V_e = v^0_{NN}(2q\beta_{NN}^2/b_N^2)^{3/2}\ (8M+4H-4B-2W),$$

$$\bar{V}_{\Lambda N} = 4v^0_{\Lambda N}(2\gamma_\Lambda\beta_{\Lambda N}^2/b_N^2)^{3/2},$$

$$x = (4M_N+M_\Lambda)/(8M_N+M_\Lambda),\quad y = 4M_N/(8M_N+M_\Lambda),$$

$$z = M_\Lambda/(4M_N+M_\Lambda),\quad u = 4M_N/(4M_N+M_\Lambda),$$

$$x' = M_\Lambda/(8M_N+M_\Lambda), \quad y' = 8M_N/(8M_N+M_\Lambda),$$

$$\eta_k = (4-kz)z, \qquad \eta_k^{(\pm)} = \eta_k \pm 2qz^2,$$

$$\zeta_k = 4x-k, \qquad \zeta_k^{(\pm)} = \zeta_k \pm 2q,$$

$$\varepsilon_k = kz, \qquad \varepsilon_k^{(\pm)} = \varepsilon_k \pm 2qz,$$

$$\tilde{\eta}_k = (2-k)z, \qquad \tilde{\eta}_k^{(\pm)} = \tilde{\eta}_k \pm 2qz,$$

$$\tilde{\varepsilon}_k = 2-k, \qquad \tilde{\varepsilon}_k^{(\pm)} = \tilde{\varepsilon}_k \pm 2q,$$

$$\tilde{C}(\ell_1\ell_3\ell_4\ell_2, J_1J_2J_3J_4; J) = [\ell_1][\ell_2][\ell_3][\ell_4] \begin{pmatrix} \ell_1 & \ell_3 & J_1 \\ \ell_4 & \ell_2 & J_2 \\ J_3 & J_4 & J \end{pmatrix}$$

$$\times (\ell_1 0 \ell_3 0 | J_1 0)(\ell_2 0 \ell_4 0 | J_2 0)(\ell_1 0 \ell_4 0 | J_3 0)(\ell_3 0 \ell_2 0 | J_4 0)$$

$$F(J_1J_2\ell\lambda; L\ell_5) = \{[J_1][J_2]\}^{1/2}[\ell_5]\ (\ell_5 0 J_1 0 | \ell 0)(\ell_5 0 J_2 0 | \lambda 0)$$

$$\times W(J_1J_2\ell\lambda; L\ell_5)\ ,$$

with $[\ell]=2\ell+1$. It is convenient to redefine the generator coordinate as

$$\sqrt{\nu_N}\, d_\beta \to d_\beta\ , \qquad \sqrt{\nu_N}\, D_\beta \to D_\beta \qquad \beta=1,2 \text{ and } 3,$$

where $\nu_N = 1/2b_N^2$ denotes the size parameter for nucleons.

(1) The overlap kernels

$$\langle \Phi^{c_1}_{\ell\lambda L}(d_1; D_1) | \Phi^{c_1}_{\ell'\lambda' L}(d_1'; D_1') \rangle = (-)^{\ell+\lambda}\, N_{c_1c_1}$$

$$\times \sum_{\ell_1\sim\ell_4} (-)^{\ell_1+\ell_2}\, \tilde{C}(\ell_1\ell_3\ell_4\ell_2, \ell\lambda\ell'\lambda'; L) \sum_{k=0}^{4} (-)^k \binom{4}{k}$$

$$\times J_{\ell_1}(\eta_k d_1 d_1')\, J_{\ell_2}(\zeta_k D_1 D_1')\, J_{\ell_3}(\varepsilon_k d_1 D_1')\, J_{\ell_4}(\varepsilon_k d_1' D_1)$$

$$\langle \Phi^{c_2}_{\ell\lambda L}(d_2; D_2) | \Phi^{c_2}_{\ell'\lambda' L}(d_2'; D_2') \rangle = \delta_{\ell\ell'}\delta_{\lambda\lambda'}\, N_{c_2c_2}\ (1+(-)^\ell)$$

$$\times J_\lambda(8x' D_2 D_2') \Big[J_\ell(2d_2 d_2') - 4 J_\ell(d_2 d_2') + 3\delta_{\ell 0} \Big],$$

$$\langle \overset{c_1}{\Phi}_{\ell\lambda L}(d_1;D_1)\,|\,\overset{c_2}{\Phi}_{\ell'\lambda' L}(d_2;D_2)\rangle = (-)^{\ell+\lambda}\, N_{c_1c_2}$$

$$\times \sum_{\ell_1\sim\ell_4} (-)^{\ell_1+\ell_3+\ell_4}\, \tilde{C}(\ell_1\ell_3\ell_4\ell_2,\ell\lambda\ell'\lambda';L)\, \int_{\ell_2}(4x'D_1D_2)$$

$$\int_{\ell_3}(4zd_1D_2) \sum_{k=0}^{4} (-)^k \binom{4}{k} \int_{\ell_1}(\tilde{\eta}_k d_1 d_2)\, \int_{\ell_4}(\tilde{\varepsilon}_k D_1 d_2),$$

where
$$N_{c_1c_1} = (4\pi)^2 \cdot \exp\left[-\{2x(D_1^2+D_1'^2)+2z(d_1^2+d_1'^2)\}\right],$$

$$N_{c_2c_2} = (4\pi)^2/2 \cdot \exp\left[-\{4x'(D_2^2+D_2'^2)+(d_2^2+d_2'^2)\}\right],$$

$$N_{c_1c_2} = (4\pi)^2/\sqrt{2} \cdot \exp\left[-(2xD_1^2+4x'D_2^2+2zd_1^2+d_2^2)\right].$$

(2) The kinetic energy kernerls

$$\langle \overset{c_1}{\Phi}_{\ell\lambda L}(d_1;D_1)\,|\,T\,|\,\overset{c_1}{\Phi}_{\ell'\lambda' L}(d_1';D_1')\rangle/\hbar\Omega$$

$$= \left\{6-\left[x(D_1^2+D_1'^2)+z(d_1^2+d_1'^2)\right]\right\} \cdot \langle \overset{c_1}{\Phi}_{\ell\lambda L}(d_1;D_1)\,|\,\overset{c_1}{\Phi}_{\ell'\lambda' L}(d_1';D_1')\rangle$$

$$+ N_{c_1c_1}(-)^{\ell+\lambda}\left\{\delta_{\ell\ell'}\delta_{\lambda\lambda'}(-)^{\ell+\lambda}\left[2zd_1d_1' \int_{\ell}(\eta_0 d_1 d_1') \int_{\lambda}(\zeta_0 D_1 D_1')\right.\right.$$

$$\left.\left. +2xD_1D_1' \int_{\ell}(\eta_0 d_1 d_1') \int_{\lambda}(\zeta_0 D_1 D_1')\right]\right.$$

$$+ 2\sum_{\ell_1\sim\ell_4} \tilde{C}(\ell_1\ell_3\ell_4\ell_2,\ell\lambda\ell'\lambda';L)\,(-)^{\ell_1+\ell_2}$$

$$\times \sum_{k=1}^{4}\Big[\; A_k^{(1)} d_1 d_1' \int_{\ell_1}^{(1)}(\eta_k d_1 d_1') \int_{\ell_2}(\zeta_k D_1 D_1') \int_{\ell_3}(\varepsilon_k d_1 D_1') \int_{\ell_4}(\varepsilon_k d_1' D_1)$$

$$+ A_k^{(2)} D_1 D_1' \int_{\ell_1}(\eta_k d_1 d_1') \int_{\ell_2}^{(1)}(\zeta_k D_1 D_1') \int_{\ell_3}(\varepsilon_k d_1 D_1') \int_{\ell_4}(\varepsilon_k d_1' D_1)$$

$$+ A_k^{(3)} d_1 D_1' \int_{\ell_1}(\eta_k d_1 d_1') \int_{\ell_2}(\zeta_k D_1 D_1') \int_{\ell_3}^{(1)}(\varepsilon_k d_1 D_1') \int_{\ell_4}(\varepsilon_k d_1' D_1)$$

$$\left. + A_k^{(3)} d_1' D_1 \int_{\ell_1}(\eta_k d_1 d_1') \int_{\ell_2}(\zeta_k D_1 D_1') \int_{\ell_3}(\varepsilon_k d_1 D_1') \int_{\ell_4}^{(1)}(\varepsilon_k d_1' D_1)\Big]\right\},$$

where
$$A_k^{(1)} = (-)^k\left[\binom{4}{k} z - \binom{3}{k-1} z^2\right], \quad A_k^{(2)} = (-)^k\left[\binom{4}{k} x - \binom{3}{k-1}\right],$$

$$A_k^{(3)} = (-)^k \binom{3}{k-1} z,$$

$$
\begin{aligned}
&\langle \Phi^{c_2}_{\ell\lambda L}(d_2;D_2)\,|\,T\,|\,\Phi^{c_2}_{\ell'\lambda' L}(d_2';D_2')\rangle/\hbar\Omega \\
&= \left\{6-\left[2x'(D_2^2+D_2'^2)+\frac{1}{2}(d_2^2+d_2'^2)\right]\right\}\langle \Phi^{c_2}_{\ell\lambda L}(d_2;D_2)\,|\,\Phi^{c_2}_{\ell'\lambda' L}(d_2';D_2')\rangle \\
&\quad + \delta_{\ell\ell'}\,\delta_{\lambda\lambda'}\,N_{c_2c_2}(1+(-)^{\ell}) \\
&\qquad \times\left\{4x'D_2D_2'\int^{(\omega)}_{\lambda}(8x'D_2D_2')\left[\int_{\ell}(2d_2d_2')-4\int_{\ell}(d_2d_2')+3\delta_{\ell 0}\right]\right. \\
&\qquad\quad \left. + \int_{\lambda}(8x'D_2D_2')\,(d_1d_1')\left[\int^{(\omega)}_{\ell}(2d_2d_2')-2\int^{(\omega)}_{\ell}(d_2d_2')\right]\right\},
\end{aligned}
$$

$$
\begin{aligned}
&\langle \Phi^{c_1}_{\ell\lambda L}(d_1;D_1)\,|\,T\,|\,\Phi^{c_2}_{\ell'\lambda' L}(d_2;D_2)\rangle/\hbar\Omega \\
&= \left\{6-\left[xD_1^2+2x'D_2^2+zd_1^2+\frac{1}{2}d_2^2\right]\right\}\langle \Phi^{c_1}_{\ell\lambda L}(d_1;D_1)\,|\,\Phi^{c_2}_{\ell'\lambda' L}(d_2;D_2)\rangle \\
&\quad + N_{c_1c_2}(-)^{\ell+\lambda}\sum_{\ell_1\sim\ell_4}(-)^{\ell_1+\ell_3+\ell_4}\,\mathcal{C}(\ell_1\ell_3\ell_4\ell_2,\ell\lambda\ell'\lambda';L) \\
&\quad \times\left\{\int_{\ell_2}(4x'D_1D_2)\int_{\ell_3}(4zd_1D_2)\sum_{k=0}^{4}{}' B_k\left[zd_1d_2\int^{(\omega)}_{\ell_1}(\tilde{\eta}_k d_1d_2)\int_{\ell_4}(\tilde{\varepsilon}_k D_1d_2)\right.\right. \\
&\qquad\qquad \left. + D_1d_2\int_{\ell_1}(\tilde{\eta}_k d_1d_2)\int^{(\omega)}_{\ell_4}(\tilde{\varepsilon}_k D_1d_2)\right] \\
&\quad + 2\left[x'D_1D_2\int^{(\omega)}_{\ell_2}(4x'D_1D_2)\int_{\ell_3}(4zd_1D_2)\right. \\
&\qquad + zd_1D_2'\int_{\ell_2}(4x'D_1D_2)\left.\int^{(\omega)}_{\ell_3}(4zd_1D_2)\right] \\
&\qquad\quad \times\left.\sum_{k=0}^{4}(-)^k\binom{4}{k}\int_{\ell_1}(\tilde{\eta}_k d_1d_2)\int_{\ell_4}(\tilde{\varepsilon}_k D_1d_2)\right\},
\end{aligned}
$$

where $\sum_{k=0}^{4}{}'$ denotes the exclusion of summation for k=2, and

$$
B_k = \begin{cases} 1 & \text{for } k=0 \\ (-)^k\left[\binom{4}{k} - 2\binom{3}{k-1}\right] & \text{for } k=1\sim 4 \end{cases}.
$$

(3) The N-N interaction kernels

$$
\begin{aligned}
&\langle \Phi^{c_1}_{\ell\lambda L}(d_1;D_1)\,|\,V_{NN}\,|\,\Phi^{c_1}_{\ell'\lambda' L}(d_1';D_1')\rangle \\
&= N_{c_1c_1}(-)^{\ell+\lambda} \\
&\quad \times\left\{2(V_d+V_e)\left[(-)^{\ell+\lambda}\delta_{\ell\ell'}\,\delta_{\lambda\lambda'}\int_{\ell}(\eta_0 d_1d_1')\int_{\lambda}(\zeta_0 D_1D_1')\right.\right.
\end{aligned}
$$

$$
\begin{aligned}
&+\sum_{\ell_1\sim\ell_4}(-)^{\ell_1+\ell_2}\,\mathcal{C}(\ell_1\ell_3\ell_4\ell_2,\ell\lambda\ell'\lambda';L)\\
&\quad\times\Big[\,\mathcal{J}_{\ell_1}(\eta_4 d_1 d_1')\mathcal{J}_{\ell_2}(\zeta_4 D_1 D_1')\mathcal{J}_{\ell_3}(\varepsilon_4 d_1 D_1')\mathcal{J}_{\ell_4}(\varepsilon_4 D_1 d_1')\\
&\qquad+2\sum_{k=1}^{3}(-)^k\mathcal{J}_{\ell_1}(\eta_k d_1 d_1')\mathcal{J}_{\ell_2}(\zeta_k D_1 D_1')\mathcal{J}_{\ell_3}(\varepsilon_k d_1 D_1')\mathcal{J}_{\ell_4}(\varepsilon_k D_1 d_1')\,\Big]\\
&+2\exp\Big[-q(D_1^2+z^2d_1^2)\Big](-)^{L+\ell+\lambda}\sum_{\ell_5 J_1 J_2}F(J_1J_2\ell\lambda;L\ell_5)\,\mathcal{J}_{\ell_5}(2qzd_1D_1)\\
&\quad\times\sum_{\ell_1\sim\ell_4}\mathcal{C}(\ell_1\ell_3\ell_4\ell_2,J_1J_2\ell'\lambda';L)\,(-)^{\ell_1+\ell_2}\\
&\quad\times\sum_{k=1}^{3}(-)^k\binom{2}{k-1}\mathcal{J}_{\ell_1}(\eta_k d_1 d_1')\mathcal{J}_{\ell_2}(\zeta_k D_1 D_1')\mathcal{J}_{\ell_3}(\varepsilon_k d_1 D_1')\mathcal{J}_{\ell_4}(\varepsilon_k D_1 d_1')\\
&+2\exp\Big[-q(D_1'^2+z^2d_1'^2)\Big](-)^{L+\ell+\lambda}\sum_{\ell_5 J_1 J_2}F(J_1J_2\ell'\lambda';L\ell_5)\,\mathcal{J}_{\ell_5}(2qzd_1'D_1')\\
&\quad\times\sum_{\ell_1\sim\ell_4}\mathcal{C}(\ell_1\ell_3\ell_4\ell_2,\ell\lambda J_1J_2;L)\,(-)^{\ell_1+\ell_2}\\
&\quad\times\sum_{k=1}^{3}(-)^k\binom{2}{k-1}\mathcal{J}_{\ell_1}(\eta_k d_1 d_1')\mathcal{J}_{\ell_2}(\zeta_k D_1 D_1')\mathcal{J}_{\ell_3}(\varepsilon_k d_1 D_1')\mathcal{J}_{\ell_4}(\varepsilon_k D_1 d_1')\\
&+2\exp\Big[-q\{D_1^2+D_1'^2+z^2(d_1^2+d_1'^2)\}\Big]\\
&\quad\times\sum_{\ell_5 J_1 J_2}F(J_1J_2\ell\lambda;L\ell_5)\,\mathcal{J}_{\ell_5}(2qzd_1D_1)\sum_{\ell_6 J_3 J_4}F(J_3J_4\ell'\lambda';L\ell_6)\,\mathcal{J}_{\ell_6}(2qzd_1'D_1')\\
&\quad\times\sum_{\ell_1\sim\ell_4}\mathcal{C}(\ell_1\ell_3\ell_4\ell_2,J_1J_2J_3J_4;L)\,(-)^{\ell_1+\ell_2}\\
&\quad\times\Big[\,V_d\Big\{\sum_{k=0}^{2}(-)^k\binom{2}{k}\mathcal{J}_{\ell_1}(\eta_k d_1 d_1')\mathcal{J}_{\ell_2}(\zeta_k D_1 D_1')\mathcal{J}_{\ell_3}(\varepsilon_k d_1 D_1')\mathcal{J}_{\ell_4}(\varepsilon_k D_1 d_1')\\
&\qquad+\sum_{k=2}^{4}(-)^k\binom{2}{k-1}\mathcal{J}_{\ell_1}(\eta_k d_1 d_1')\mathcal{J}_{\ell_2}(\zeta_k D_1 D_1')\mathcal{J}_{\ell_3}(\varepsilon_k d_1 D_1')\mathcal{J}_{\ell_4}(\varepsilon_k D_1 d_1')\Big\}\\
&\quad-V_e\sum_{k=1}^{3}(-)^k\binom{2}{k-1}\Big\{\mathcal{J}_{\ell_1}(\eta_k d_1 d_1')\mathcal{J}_{\ell_2}(\zeta_k D_1 D_1')\mathcal{J}_{\ell_3}(\varepsilon_k d_1 D_1')\mathcal{J}_{\ell_4}(\varepsilon_k D_1 d_1')\\
&\qquad+\mathcal{J}_{\ell_1}(\eta_k d_1 d_1')\mathcal{J}_{\ell_2}(\zeta_k D_1 D_1')\mathcal{J}_{\ell_3}(\varepsilon_k d_1 D_1')\mathcal{J}_{\ell_4}(\varepsilon_k D_1 d_1')\Big\}\,\Big]\Big\},
\end{aligned}
$$

$$
\begin{aligned}
&\langle\Phi^{c_2}_{\ell\lambda L}(d_2;D_2)\,|\,V_{NN}\,|\,\Phi^{c_2}_{\ell'\lambda' L}(d_2';D_2')\rangle\\
&\quad=\delta_{\ell\ell'}\delta_{\lambda\lambda'}\,N_{c_2c_2}\,(1+(-)^{\ell})\,\mathcal{J}_{\lambda}(8x'D_2D_2')
\end{aligned}
$$

$$
\times \Big\{ (2V_d+2V_e) \Big[\int_\ell (2d_2d_2') - 2\int_\ell (d_2d_2') + \delta_{\ell 0}
- 2\Big[\exp(-qd_2^2)+\exp(-qd_2'^2)\Big] \Big(\int_\ell (d_2d_2') - \delta_{\ell 0} \Big) \Big]
$$

$$
+ 2V_d \cdot \exp\Big[-q(d_2^2+d_2'^2)\Big]
\times \Big[\int_\ell ((2-2q)d_2d_2') - 2\int_\ell ((1-2q)d_2d_2') + \int_\ell (2qd_2d_2') \Big]
$$

$$
+ 2V_e \cdot \exp\Big[-q(d_2^2+d_2'^2)\Big]
\times \Big[\int_\ell ((1-2q)d_2d_2') - 2\int_\ell (2qd_2d_2') + \int_\ell ((1+2q)d_2d_2') \Big] \Big\},
$$

$$
\langle \Phi^{c_1}_{\ell\lambda L}(d_1;D_1) | V_{NN} | \Phi^{c_2}_{\ell'\lambda' L}(d_2;D_2) \rangle
$$

$$
= N_{c_1c_2} (-)^{\ell+\lambda}
$$

$$
\times \Big\{ 2(V_d+V_e) \sum_{\ell_1\sim\ell_4} (-)^{\ell_1+\ell_3+\ell_4} \tilde{C}(\ell_1\ell_3\ell_4\ell_2, \ell\lambda\ell'\lambda'; L)
$$

$$
\Big[\int_{\ell_2}(4x'D_1D_2) \int_{\ell_3}(4zd_1D_2) \{ \int_{\ell_1}(\tilde{\eta}_0 d_1d_2) \int_{\ell_4}(\tilde{\varepsilon}_0 D_1d_2)
$$

$$
+ \int_{\ell_1}(\tilde{\eta}_4 d_1d_2) \int_{\ell_4}(\tilde{\varepsilon}_4 D_1d_2) - 2\delta_{\ell_1 0}\,\delta_{\ell_4 0}
$$

$$
+2\Big[1+\exp(-qd_2^2)\Big] \sum_{k=1}^{3} (-)^k \binom{2}{k-1} \int_{\ell_1}(\tilde{\eta}_k d_1d_2) \int_{\ell_4}(\tilde{\varepsilon}_k D_1d_2) \} \Big]
$$

$$
+ (-)^{\ell+\lambda+L} \sum_{\ell_5 J_1 J_2} F(J_1J_2\ell\lambda; L\ell_5) \int_{\ell_5}(2qzd_1D_1)
$$

$$
\times \sum_{\ell_1\sim\ell_4} \tilde{C}(\ell_1\ell_3\ell_4\ell_2, J_1J_2\ell'\lambda'; L)(-)^{\ell_1+\ell_3+\ell_4} \int_{\ell_2}(4x'D_1D_2) \int_{\ell_3}(4zd_1D_2)
$$

$$
\times \Big\{ 4(V_d+V_e)\exp\{-q(D_1^2+z^2d_1^2)\} \sum_{k=1}^{3} (-)^k \binom{2}{k-1} \int_{\ell_1}(\tilde{\eta}_k d_1d_2) \int_{\ell_4}(\tilde{\varepsilon}_k D_1d_2)
$$

$$
+ 2\exp\Big[-q(D_1^2+z^2d_1^2+d_2^2)\Big]
$$

$$
\times \Big\{ V_d \Big[\sum_{k=0}^{2} (-)^k \binom{2}{k} \int_{\ell_1}(\tilde{\eta}_k d_1d_2) \int_{\ell_4}(\tilde{\varepsilon}_k D_1d_2)
$$

$$
+ \sum_{k=2}^{4} (-)^k \binom{2}{k-2} \int_{\ell_1}(\tilde{\eta}_k d_1d_2) \int_{\ell_4}(\tilde{\varepsilon}_k D_1d_2) \Big]
$$

$$
+ V_e \sum_{k=1}^{3} (-)^{k+1} \binom{2}{k-1} \Big[\int_{\ell_1}(\tilde{\eta}_k d_1d_2) \int_{\ell_4}(\tilde{\varepsilon}_k D_1d_2)
$$

$$
+ \int_{\ell_1}(\tilde{\eta}_k d_1d_2) \int_{\ell_4}(\tilde{\varepsilon}_k D_1d_2) \Big] \Big] \Big\} \Big\}
$$

(4) The Λ-N interaction kernels

$$
\begin{aligned}
&\langle \overset{c_1}{\Phi}_{\ell\lambda L}(d_1;D_1)\,|\,V_{\Lambda N}\,|\,\overset{c_1}{\Phi}_{\ell'\lambda' L}(d_1';D_1')\rangle \\
&= N_{c_1c_1}(-)^{\ell+\lambda}\,\bar{V}_{\Lambda N} \\
&\times\Big\{\exp\Big[-\gamma_\Lambda(d_1^2+d_1'^2)\Big]\sum_{\ell_1\sim\ell_4}\tilde{C}(\ell_1\ell_3\ell_4\ell_2,\ell\lambda\ell'\lambda';L)\,(-)^{\ell_1+\ell_2} \\
&\qquad\times\sum_{k=0}^{3}(-)^k\binom{3}{k}\int_{\ell_1}\{(\eta_k-2\gamma_\Lambda)d_1d_1'\}\int_{\ell_2}\{\zeta_k D_1D_1'\} \\
&\qquad\qquad\times\int_{\ell_3}\{\varepsilon_k d_1D_2'\}\int_{\ell_4}\{\varepsilon_k D_1d_2'\} \\
&+\exp\Big[-\gamma_\Lambda(D_1^2+u^2d_1^2+d_1'^2)\Big]\,(-)^{\ell+\lambda+L} \\
&\times\sum_{\ell_5J_1J_2}F(J_1J_2\ell\lambda;L\ell_5)(-)^{\ell_5}\int_{\ell_5}\{2u\gamma_\Lambda d_1D_1\}\sum_{\ell_1\sim\ell_4}\tilde{C}(\ell_1\ell_3\ell_4\ell_2,J_1J_2\ell'\lambda';L) \\
&\quad\times(-)^{\ell_1+\ell_2}\sum_{k=1}^{4}(-)^k\binom{3}{k-1}\int_{\ell_1}\{(\eta_k-2u\gamma_\Lambda)d_1d_1'\}\int_{\ell_2}\{\zeta_k D_1D_1'\} \\
&\qquad\qquad\times\int_{\ell_3}\{\varepsilon_k d_1D_1'\}\int_{\ell_4}\{(\varepsilon_k-2\gamma_\Lambda)D_1d_1'\} \\
&+\exp\Big[-\gamma_\Lambda(D_1'^2+u^2d_1'^2+d_1^2)\Big]\,(-)^{\ell'+\lambda'+L} \\
&\times\sum_{\ell_5J_1J_2}F(J_1J_2\ell'\lambda';L\ell_5)(-)^{\ell_5}\int_{\ell_5}\{2u\gamma_\Lambda d_1'D_1'\}\sum_{\ell_1\sim\ell_4}\tilde{C}(\ell_1\ell_3\ell_4\ell_2,\ell\lambda J_1J_2;L) \\
&\quad\times(-)^{\ell_1+\ell_2}\sum_{k=1}^{4}(-)^k\binom{3}{k-1}\int_{\ell_1}\{(\eta_k-2u\gamma_\Lambda)d_1d_1'\}\int_{\ell_2}\{\zeta_k D_1D_1'\} \\
&\qquad\qquad\times\int_{\ell_3}\{(\varepsilon_k-2\gamma_\Lambda)d_1D_1'\}\int_{\ell_4}\{\varepsilon_k D_1d_1'\} \\
&+\exp\Big[-\gamma_\Lambda(D_1^2+D_1'^2+u^2(d_1^2+d_1'^2))\Big] \\
&\times\sum_{\ell_5J_1J_2}F(J_1J_2\ell\lambda;L\ell_5)(-)^{\ell_5}\int_{\ell_5}\{2u\gamma_\Lambda d_1D_1\}\sum_{\ell_6J_3J_4}F(J_3J_4\ell'\lambda';L\ell_6) \\
&\quad\times(-)^{\ell_6}\int_{\ell_6}\{2u\gamma_\Lambda d_1'D_1'\}\sum_{\ell_1\sim\ell_4}\tilde{C}(\ell_1\ell_3\ell_4\ell_2,J_1J_2J_3J_4;L)\,(-)^{\ell_1+\ell_2} \\
&\qquad\times\sum_{k=0}^{3}(-)^k\binom{3}{k}\int_{\ell_1}\{(\eta_k-2u^2\gamma_\Lambda)d_1d_1'\}\int_{\ell_2}\{(\zeta_k-2\gamma_\Lambda)D_1D_1'\} \\
&\qquad\qquad\times\int_{\ell_3}\{(\varepsilon_k-2u\gamma_\Lambda)d_1D_1'\}\int_{\ell_4}\{(\varepsilon_k-2u\gamma_\Lambda)D_1d_1'\}\Big\},
\end{aligned}
$$

$$
\langle \Phi^{c_2}_{\ell\lambda L}(d_2;D_2)\,|\,V_{\Lambda N}\,|\,\Phi^{c_2}_{\ell'\lambda' L}(d_2';D_2')\rangle
$$

$$
= N_{c_2c_2}(-)^{\ell+\lambda}\ 4\bar{V}_{\Lambda N}
$$

$$
\times\Big\{\exp\Big[-\gamma_\Lambda(D_2^2+D_2'^2+d_2^2/4+d_2'^2/4)\Big]
$$

$$
\times\sum_{\ell_5}\sum_{J_1J_2}F(J_1J_2\ell\lambda;L\ell_5)\,\mathcal{J}_{\ell_5}(\gamma_\Lambda d_2D_2)\sum_{\ell_6}\sum_{J_3J_4}F(J_3J_4\ell'\lambda';L\ell_6)\,\mathcal{J}_{\ell_6}(\gamma_\Lambda d_2'D_2')
$$

$$
\times\sum_{\ell_1\sim\ell_4}\mathcal{C}(\ell_1\ell_3\ell_4\ell_2,J_1J_2J_3J_4;L)\,(-)^{\ell_1+\ell_2}\,\mathcal{J}_{\ell_2}((8x'-2\gamma_\Lambda)D_2D_2')
$$

$$
\times\,\mathcal{J}_{\ell_3}(\gamma_\Lambda d_2D_2')\,\mathcal{J}_{\ell_4}(\gamma_\Lambda D_2d_2')\sum_{k=0}^{3}(-)^k\binom{3}{k}\,\mathcal{J}_{\ell_1}((2-k-\gamma_\Lambda/2)d_2d_2')\Big\},
$$

$$
\langle \Phi^{c_1}_{\ell\lambda L}(d_1;D_1)\,|\,V_{\Lambda N}\,|\,\Phi^{c_2}_{\ell'\lambda' L}(d_2;D_2)\rangle
$$

$$
= N_{c_1c_2}(-)^{\ell+\lambda}\ \bar{V}_{\Lambda N}
$$

$$
\times\Big\{\exp\Big[-\gamma_\Lambda(D_1^2+D_2^2+u^2d_1^2+d_2^2/4)\Big]\sum_{\ell_5}\sum_{J_1J_2}F(J_1J_2\ell\lambda;L\ell_5)(-)^{\ell_5}\mathcal{J}_{\ell_5}(u\gamma_\Lambda d_1D_1)
$$

$$
\times\sum_{\ell_6}\sum_{J_3J_4}F(J_3J_4\ell'\lambda';L\ell_6)\,(-)^{\ell_6}\,\mathcal{J}_{\ell_6}(\gamma_\Lambda d_2D_2)
$$

$$
\times\sum_{\ell_1\sim\ell_4}\mathcal{C}(\ell_1\ell_3\ell_4\ell_2,J_1J_2J_3J_4;L)\,(-)^{\ell_1+\ell_3+\ell_4}
$$

$$
\times\,\mathcal{J}_{\ell_2}((4x'-2\gamma_\Lambda)D_1D_2)\,\mathcal{J}_{\ell_3}((4z-2u\gamma_\Lambda)d_1D_2)
$$

$$
\times\sum_{k=0}^{3}(-)^k\binom{3}{k}\,\mathcal{J}_{\ell_1}((\tilde{\eta}_k+u\gamma_\Lambda)d_1d_2)\,\mathcal{J}_{\ell_4}((\tilde{\varepsilon}_k-\gamma_\Lambda)D_1d_2)
$$

$$
+\sum_{\ell_6}\sum_{J_3J_4}F(J_3J_4\ell'\lambda';L\ell_6)\,\mathcal{J}_{\ell_6}(\gamma_\Lambda d_2D_2)
$$

$$
\times\sum_{\ell_1\sim\ell_4}\mathcal{C}(\ell_1\ell_3\ell_4\ell_2,J_1J_2J_3J_4;L)\,(-)^{\ell_1+\ell_3+\ell_4}
$$

$$
\times\,\mathcal{J}_{\ell_2}((4x'-2\gamma_\Lambda)D_1D_2)\,\mathcal{J}_{\ell_3}((4z-2u\gamma_\Lambda)d_1D_2)
$$

$$
\times\sum_{k=1}^{4}(-)^k\binom{3}{k-1}\,\mathcal{J}_{\ell_1}((\tilde{\eta}_k-u\gamma_\Lambda)d_1d_2)\,\mathcal{J}_{\ell_4}((\tilde{\varepsilon}_k+\gamma_\Lambda)D_1d_2)
$$

$$
+\exp\Big[-\gamma_\Lambda(d_1^2+D_2^2+d_2^2/4)\Big]\ (-)^{\ell+\lambda+L}
$$

$$\times \sum_{\ell_5 J_1 J_2} F(J_1 J_2 \ell' \lambda'; L \ell_5) \int_{\ell_5}(\gamma_\Lambda d_2 D_2)$$

$$\times \sum_{\ell_1 \sim \ell_4} \tilde{C}(\ell_1 \ell_3 \ell_4 \ell_2, \ell \lambda J_1 J_2; L) \; (-)^{\ell_1+\ell_3+\ell_4} \int_{\ell_2}(4x' D_1 D_2)$$

$$\times \int_{\ell_3}((4z-2\gamma_\Lambda) d_1 D_2) \sum_{k=0}^{3} (-)^k \binom{3}{k} \int_{\ell_1}((\tilde{\eta}_k - \gamma_\Lambda) d_1 d_2) \int_{\ell_4}(\tilde{\varepsilon}_k D_1 d_2)$$

$$+ \sum_{\ell_5 J_1 J_2} F(J_1 J_2 \ell' \lambda'; L \ell_5) \; (-)^{\ell_5} \int_{\ell_5}(\gamma_\Lambda d_2 D_2)$$

$$\times \sum_{\ell_1 \sim \ell_4} \tilde{C}(\ell_1 \ell_3 \ell_4 \ell_2, \ell \lambda J_1 J_2; L) \; (-)^{\ell_1+\ell_3+\ell_4} \int_{\ell_2}(4x' D_1 D_2)$$

$$\times \int_{\ell_3}((4z-2\gamma_\Lambda) d_1 D_2) \sum_{k=1}^{4} (-)^k \binom{3}{k-1} \int_{\ell_1}((\tilde{\eta}_k + \gamma_\Lambda) d_1 d_2) \int_{\ell_4}(\tilde{\varepsilon}_k D_1 d_2) \Big\} .$$

Appendix B

In this Appendix we give an explicit expression of the squared transition matrix element $N_n(E)$ in Eq.(2.42).

The ^{8}Be($\alpha\alpha$)-n reduced width amplitude $\mathcal{Y}_{\ell_i\lambda_i L_N,d_i}(R)$ for the normalized ^{9}Be-ground-state wave function $\Psi_{J_i}(^9\mathrm{Be})$ ($J_i=3/2^-$) obtained by the microscopic $\alpha+\alpha+n$ cluster model[63] is defined by

$$\mathcal{Y}_{\ell_i\lambda_i L_N,d_i}(R) = \frac{9}{1}\left\langle \Psi_{J_i}(^9\mathrm{Be}) \middle| \left[\left(\psi_{\ell_i}^{d_i}(^8\mathrm{Be}) \times \frac{1}{R^2}\delta(R'-R) Y_{\lambda_i}(\hat{R}') \right)_{L_N} \times \theta^n_{1/2} \right]_{J_i} \right\rangle, \quad \text{(B.1)}$$

$$\psi_{\ell_i}^{d_i}(^8\mathrm{Be}) = \frac{1}{\sqrt{2}} \sqrt{\binom{8}{4}^{-1}} \mathcal{A}\left[\phi(\alpha)\phi(\alpha)\, \varphi_{\ell_i}(r';d_i)\, Y_{\ell_i}(\hat{r}') \right], \quad \text{(B.2)}$$

where ℓ_i and λ_i denote the angular momentums with respect to the α-α and $(\alpha+\alpha)$-n relative coordinate, $\vec{r}$ and $\vec{R}$, respectively, and L_N is the total orbital angular momentum, $\vec{L}_N = \vec{\ell}_i + \vec{\lambda}_i$. The generator coordinate (GC) d_i in the wave packet $\varphi_{\ell_i}(r',d_i)$ which is defined in Eq.(2.6) specifies the α-α relative distance, and $\theta^n_{1/2}$ is the spin function of the valence neutron.

The n-th $^9_\Lambda$Be eigenstate $\Psi_n^{L_\Lambda}(^9_\Lambda\mathrm{Be};E)$ with the Kapur-Peierls-type outgoing wave boundary condition in Eq.(2.23) can be expanded in terms of the GC basis $\psi_{\ell_i}^{d_i}(^8\mathrm{Be})$ (see Eq.(B.2)) for the $\alpha+\alpha$ relative part and the wave packet $\varphi_{\lambda_f}(R;D_f)$ (see Eq.(2.6)) for the $(\alpha+\alpha)$-Λ part, as shown in Fig.3(b) and (c),

$$\Psi_n^{L_\Lambda}(^9_\Lambda\mathrm{Be};E) = \sum_{\substack{c_f=(\ell_f,\lambda_f)_{L_\Lambda} \\ d_f,\ D_f}} A_n^{c_f}(d_f,D_f;E) \left[\psi_{\ell_f}^{d_f}(^8\mathrm{Be}) \varphi_{\lambda_f}(R;D_f) Y_{\lambda_f}(\hat{R}) \right]_{L_\Lambda}, \quad \text{(B.3)}$$

where $A_n^{c_f}(d_f,D_f;E)$ is the expansion coefficient obtained by solving the coupled-channel integro-differential equations with the Bloch operator in Eq.(2.28), and $c_f=(\ell_f,\lambda_f)_{L_\Lambda}$ denotes a channel of the angular momentum coupling. Other notations are self-explanatory.

With the use of Eqs.(B.1) and (B.3), the transition matrix element $N_n(E)$ is expressed by

$$N_n(E) = \frac{1}{[J_i]} \sum_{J_f=L_\Lambda\pm 1/2} \sum_{k,\mu} \left| M_{k\mu}(J_f,J_i;E) \right|^2 , \qquad (B.4)$$

$$\begin{aligned} M_{k\mu}(J_f,J_i;E) = & \sum_{\substack{c_f=(\ell_f,\lambda_f)_{L_\Lambda} \\ d_f,\ D_f}} \sum_{(\ell_i,\lambda_i)_{L_N}} \sqrt{[J_i][J_f][L_N][L_\Lambda][\lambda_i][k]} \\ & \times (\lambda_i 0k0|\lambda_f 0)\ W(L_\Lambda 1/2kJ_i;J_f L_N)\ W(\ell_f\lambda_i L_\Lambda k;L_N\lambda_f)\ \delta_{\ell_i\ell_f} \\ & \times \sqrt{\binom{9}{1}^{-1}}\ A_n^{c_f}(d_f,D_f;E) \\ & \times \langle \varphi_{\lambda_f}(R;D_f)|\hat{\gamma}_{J_{k\mu}}(p_K,p_\pi,\theta;8R/9)|\ \mathcal{Y}_{\ell_i\lambda_i L_N,d_f}(R)\rangle, \qquad (B.5) \end{aligned}$$

where $[k]=2k+1$, and $\hat{\gamma}_{J_{k\mu}}$ is given in Eq.(2.47).

Appendix C

The folding potential between the Λ particle and the $\alpha+^{16}O$ nucleus is defined in Eq.(4.15). The explicit expression for the Gaussian Λ-N interaction of Eq.(2.17) is given in terms of the spherical Bessel function with an imaginary argument $\mathcal{J}_\ell(z)$.

$$
\begin{aligned}
U(R;c_1d_1,c_2d_2) &= 16\pi v^0_{\Lambda N}(\gamma_0\beta^2_{\Lambda N})^{3/2}\exp\left[-\gamma_0R^2-\frac{4}{5b_N^2}+\frac{\gamma_0}{100}(d_1^2+d_2^2)\right] \\
&\times (-)^L\sqrt{[\lambda_1][\lambda_2]}\sum_{q_4}(\lambda_1 0\lambda_2 0|q_4 0)\,W(\ell_1\lambda_1\ell_2\lambda_2;Lq_4) \\
&\times \sum_{q_1q_2q_3}(-)^{q_1+q_2+q_3}[q_1][q_2][q_3](q_1 0q_2 0|\ell_1 0)(q_1 0q_3 0|\ell_2 0) \\
&\times (q_2 0q_3 0|q_4 0)\,W(\ell_1q_2\ell_2q_3;q_1q_4)\sum_{k=0}^{3}(-)^k\binom{3}{k}\sum_{r=0}^{k}\binom{k}{r}\left[\frac{d_1d_2}{2b_N^2}\right]^r \\
&\times\Bigg\{\exp\left[-\frac{3}{20}\gamma_0(d_1^2+d_2^2)\right]\mathcal{J}^{(r)}_{q_1}(h_1(k)d_1d_2)\,\mathcal{J}_{q_2}\left(\tfrac{4}{5}\gamma_0d_1R\right)\mathcal{J}_{q_3}\left(\tfrac{4}{5}\gamma_0d_2R\right) \\
&\quad-\exp\left[-\frac{3}{20}\gamma_0d_1^2\right]\Bigg\{\Bigg[\left(1+\frac{\gamma_0}{10}d_2^2\right)\mathcal{J}^{(r)}_{q_1}(h_1(k)d_1d_2) \\
&\qquad+\gamma_0d_1d_2\left(\frac{\gamma^2}{2b_N^2}+\frac{1}{10}\right)\mathcal{J}^{(r+1)}_{q_1}(h_1(k)d_1d_2)\Bigg]\mathcal{J}_{q_2}\left(\tfrac{4}{5}\gamma_0d_1R\right)\mathcal{J}_{q_3}\left(-\tfrac{1}{5}\gamma_0d_2R\right) \\
&\qquad+(\gamma_0d_2R)\,\mathcal{J}^{(r)}_{q_1}(h_2(k)d_1d_2)\,\mathcal{J}_{q_2}\left(\tfrac{4}{5}\gamma_0d_1R\right)\mathcal{J}^{(1)}_{q_3}\left(-\tfrac{1}{5}\gamma_0d_2R\right)\Bigg\} \\
&\quad-\exp\left[-\frac{3}{20}\gamma_0d_2^2\right]\Bigg\{\Bigg[\left(1+\frac{\gamma_0}{10}d_1^2\right)\mathcal{J}^{(r)}_{q_1}(h_1(k)d_1d_2) \\
&\qquad+\gamma_0d_1d_2\left(\frac{\gamma^2}{2b_N^2}+\frac{1}{10}\right)\mathcal{J}^{(r+1)}_{q_1}(h_1(k)d_1d_2)\Bigg]\mathcal{J}_{q_2}\left(-\tfrac{1}{5}\gamma_0d_1R\right)\mathcal{J}_{q_3}\left(\tfrac{4}{5}\gamma_0d_2R\right) \\
&\qquad+(\gamma_0d_1R)\,\mathcal{J}^{(r)}_{q_1}(h_2(k)d_1d_2)\,\mathcal{J}_{q_2}\left(-\tfrac{1}{5}\gamma_0d_1R\right)\mathcal{J}^{(1)}_{q_3}\left(\tfrac{4}{5}\gamma_0d_2R\right)\Bigg\} \\
&\quad+\left[f_1(d_1,d_2,R)\,\mathcal{J}^{(r)}_{q_1}(h_3(k)d_1d_2)+\frac{1}{25}(\gamma_0^2b_N^2d_1d_2)\mathcal{J}^{(r+1)}_{q_1}(h_3(k)d_1d_2)\right] \\
&\qquad\times\mathcal{J}_{q_2}\left(-\tfrac{1}{5}\gamma_0d_1R\right)\mathcal{J}_{q_3}\left(-\tfrac{1}{5}\gamma_0d_2R\right) \\
&\quad+\frac{2}{5}(\gamma_0^2b_N^2)\,\mathcal{J}^{(r)}_{q_1}(h_3(k)d_1d_2)\Big[(d_1R)\,\mathcal{J}^{(1)}_{q_2}\left(-\tfrac{1}{5}\gamma_0d_1R\right)\mathcal{J}_{q_3}\left(-\tfrac{1}{5}\gamma_0d_2R\right)
\end{aligned}
$$

$$+ (d_2 R) \int_{q_2}\left(-\tfrac{1}{5}\gamma_0 d_1 R\right) \int^{(1)}_{q_3}\left(-\tfrac{1}{5}\gamma_0 d_2 R\right) \Big]$$

$$+ \Big[f_2(d_1,d_2,R) \int^{(r)}_{q_1} (h_3(k+1)d_1 d_2) + \gamma_0 d_1 d_2 f_3(R) \int^{(r+1)}_{q_1} (h_3(k+1)d_1 d_2)$$

$$- \frac{\gamma_0^2}{100}(d_1^2 d_2^2) \int^{(r+2)}_{q_1} (h_3(k+1)d_1 d_2) \Big] \int_{q_2}\left(-\tfrac{1}{5}\gamma_0 d_1 R\right) \int_{q_3}\left(-\tfrac{1}{5}\gamma_0 d_2 R\right)$$

$$+ \Big[f_4(d_2) \int^{(r)}_{q_1} (h_3(k+1)d_1 d_2) - \frac{1}{10}(\gamma_0 d_1 d_2) \int^{(r+1)}_{q_1} (h_3(k+1)d_1 d_2) \Big]$$

$$\times (\gamma_0 d_1 R) \int^{(1)}_{q_2}\left(-\tfrac{1}{5}\gamma_0 d_1 R\right) \int_{q_3}\left(-\tfrac{1}{5}\gamma_0 d_2 R\right)$$

$$+ \Big[f_4(d_1) \int^{(r)}_{q_1} (h_3(k+1)d_1 d_2) - \frac{1}{10}(\gamma_0 d_1 d_2) \int^{(r+1)}_{q_1} (h_3(k+1)d_1 d_2) \Big]$$

$$\times (\gamma_0 d_2 R) \int_{q_2}\left(-\tfrac{1}{5}\gamma_0 d_1 R\right) \int^{(1)}_{q_3}\left(-\tfrac{1}{5}\gamma_0 d_2 R\right)$$

$$+ \int^{(r)}_{q_1} (h_3(k+1)d_1 d_2)(\gamma_0 d_1 R) \int^{(1)}_{q_2}\left(-\tfrac{1}{5}\gamma_0 d_1 R\right)$$

$$\times (\gamma_0 d_2 R) \int^{(1)}_{q_3}\left(-\tfrac{1}{5}\gamma_0 d_2 R\right) \Big\}, \qquad (C.1)$$

where

$$\gamma_0 = 1/(\gamma^2 + b_N^2) \quad , \qquad \gamma^2 = \beta_{\Lambda N}^2 - b_N^2/20 \ , \qquad (C.2)$$

$$h_1(k) = \frac{1}{2b_N^2}\left[-k + \frac{11}{5} + \gamma_0\gamma^2 + \frac{9}{25}\gamma_0 b_N^2 \right] , \qquad (C.3a)$$

$$h_2(k) = \frac{1}{2b_N^2}\left[-k + \frac{11}{5} + \frac{4}{25}\gamma_0 b_N^2 \right] , \qquad (C.3b)$$

$$h_3(k) = \frac{1}{2b_N^2}\left[-k + \frac{16}{5} - \frac{1}{25}\gamma_0 b_N^2 \right] , \qquad (C.3c)$$

$$f_1(d_1,d_2,R) = (1+3\gamma_0\gamma^2) + \frac{1}{50}\gamma_0^2 b_N^2 (d_1^2+d_2^2) + 2\gamma_0^2 b_N^2 R^2 \ , \qquad (C.4a)$$

$$f_2(d_1,d_2,R) = -3\gamma_0\gamma^2 + \frac{\gamma_0}{10}\left[1 - \frac{\gamma_0 b_N^2}{5}\right](d_1^2+d_2^2) + \frac{\gamma_0^2}{100} d_1^2 d_2^2 - 2\gamma_0^2 b_N^2 R^2 \ , \qquad (C.4b)$$

$$f_3(R) = \frac{1}{5}\left[1 - \frac{\gamma_0 b_N^2}{5}\right] - \frac{1}{2\gamma_0 b_N^2}(1+2\gamma_0\gamma^2) - \gamma_0 R^2 \ , \qquad (C.4c)$$

$$f_4(d) = 1 - \frac{2}{5}\gamma_0 b_N^2 + \frac{1}{10}\gamma_0 d^2 \ . \qquad (C.4d)$$

Appendix D

The reduced quadrupole transition probability $B(E2;L_i \to L_f)$ is defined with the use of the electric quadrupole transition operator M(E2) in Eq.(4.18), and its explicit expression is given by

$$B(E2;L_i \to L_f) = \frac{1}{2L_i+1} \sum_{M_i,M_f} \left| \langle \Psi_{L_f M_f} | M(E2) | \Psi_{L_i M_i} \rangle \right|^2, \quad (D.1)$$

$$= e^2 (2L_f+1) \Bigg\{ \sum_{c_i,d_i,n_i} \sum_{c_f,d_f,n_f} w_{c_i}(d_i,n_i)\, w_{c_f}(d_f,n_f)$$

$$\times \Bigg[\delta_{\ell_f,\ell_i} \sqrt{(2\lambda_f+1)}\, (-)^{\ell_f+\lambda_f-L_i}\, W(\lambda_f L_f \lambda_i L_i;\ell_i 2)\, (\lambda_f|2|\lambda_i)$$

$$\times \frac{8}{5} N_{\ell_i}(d_i,d_f) \langle u_{n_f\lambda_f}(R)|R^2|u_{n_i\lambda_i}(R)\rangle$$

$$+ \delta_{\lambda_f,\lambda_i} \delta_{n_f,n_i} \sqrt{(2\ell_f+1)}\, (-)^{\ell_i+\lambda_i-L_f}\, W(\ell_f L_f \ell_i L_i;\lambda_i 2)\, (\ell_f|2|\ell_i)$$

$$\times \frac{10M_\Lambda^2}{(20M_N+M_\Lambda)^2} \sum_{n_i,n_f} a_{n_i\ell_i}(d_i)\, a_{n_f\ell_f}(d_f)\, \mu_{N<}$$

$$\times \langle u_{n_f\ell_f}(r)|r^2|u_{n_i\ell_i}(r)\rangle \Bigg] \Bigg\}^2, \quad (D.2)$$

where $N<$ denotes the smaller value of $2n_i+\ell_i$ and $2n_f+\ell_f$, and $(\lambda_f|2|\lambda_i)$ is $\sqrt{5/(4\pi)}\ (\lambda_f 020|\lambda_i 0)$.

References

1) See, for examples,
D.H. Davis and J. Sacton, High Energy Physics,
ed. E.H.S. Burhop, Vol.2 (Academic Press, 1967).
J. Pnievski, Methods in Subnuclear Physics, ed. M. Nikelic,
Vol.V, Part 1 (Gordon and Breach, 1969).

2) See, for example,
A. Gal, Advances in Nucl. Phys., eds. M. Baranger and
E. Vogt, Vol.8 (1975, Plenum), p.1.

3) D.J. Prouse, Phys. Rev. Lett. 17 (1966), 782.

4) M. Danysz et al., Nucl. Phys. 49 (1963), 121.

5) G. Alexander et al., Phys. Rev. 173 (1968), 1452.
B. Sechi-Zorn et al., Phys. Rev. 175 (1968), 1735.
J.A. Kadyk et al., Nucl. Phys. B27 (1971), 13.
J.M. Hauptman, LBL Report No. LBL-3608 (1974).
F. Eisele et al., Phys. Lett. 37B (1971), 204.
R. Engelamnn et al., Phys. Lett. 21 (1966), 587.

6) Proc. Int. Conf. on Hyperfragments CERN, 1964, ed. W. Lock.
Proc. Int. Conf. on Hypernuclear Physics, 1969, Argonne,
eds. A.R. Bodmer and L.G. Hyman.
Proc. Summer Study Meeting on Nuclear and Hypernuclear
Physics with Kaon Beems, ed. H. Palevsky, BNL Report 18335
(1973).
See Ref.2) as the most comprehensive review at that time.

7) W. Brückner et al., Phys. Lett. 55B (1975), 107; 62B (1976),
481; 79B (1978), 157; Proc. Kaon Factory Workshop, ed.

M.K. Craddock (Triumf, Vancouver, 1979), p.124.

8) R. Bertini et al., Phys. Lett. 83B (1979), 306; Nucl. Phys. A360 (1981), 315; A368 (1981), 365.

9) B. Povh, Rep. Prog. Phys. 39 (1976), 824; Ann. Rev. Nucl. Part. Sci., eds. J.D. Jackson et al. (1978, Annual Reviews Inc., Palo Alto), p.1; J. Phys. Soc. Jpn. 44 (1978), Suppl. p.775; Nucl. Phys. A335 (1980), 233.

10) B. Povh, Prog. Part. Nucl. Phys. 5 (1981), 245.

11) M. Bedjidian et al., Phys. Lett. 94B (1980), 480.

12) R.E. Chrien et al., Phys. Lett. 89B (1979), 31.

13) M. May et al., Phys. Rev. Lett. 47 (1981), 1106.

14) M. May et al., Phys. Rev. Lett. 51 (1983), 2085.

15) R. Grace et al., Phys. Rev. Lett. 55 (1985), 1055.

16) R. Bertini et al., Phys. Lett. 90B (1980), 375; 136B (1984), 29; 158B (1985), 19.

17) H. Piekarz et al., Phys. Lett. 110B (1982), 428.

18) T. Yamazaki and T. Ishikawa, Proc. Workshop Hypernuclear Physics (KEK, 1982), p.66.
T. Yamazaki, T. Ishikawa, K. Yazaki and A. Matsuyama, Phys. Lett. 144B (1984), 177.
T. Yamazaki et al., Phys. Rev. Lett. 54 (1985), 102.

19) M.M. Nagels, T.A. Rijken and J.J. deSwart, Phys. Rev. D12 (1975), 744; D15 (1977), 2547; D20 (1979), 1633.

20) Y. Yamamoto and H. Bandō, Prog. Theor. Phys. Suppl. No.81 (1985), Chap.II.

21) A. Gal, J.M. Soper and R.H. Dalitz, Ann. of Phys. 63 (1971), 53; 72 (1972), 445; 113 (1978), 79.

22) R.H. Dalitz and A. Gal, Phys. Rev. Lett. 36 (1976), 362; Ann. of Phys. 116 (1978), 167; 131 (1981), 314.

23) R.H. Dalitz, Proc. Int. Conf. Nuclear Structure (1980, Berkeley), Nucl. Phys. A354 (1981), 101c.

24) C.B. Dover, L. Ludeking and G.E. Walker, Phys. Rev. C22 (1980), 2073.

C.B. Dover, Proc. 9th Int. Conf. High Energy Physics and Nuclear Structure (1981, Varsailles), Nucl. Phys. A374 (1982), 359c.

C.B. Dover and G.E. Walker, Phys. Rep. 89, No.1 (1982), p.1.

25) E.H. Auerbach, A.J. Baltz, C.B. Dover, A. Gal, S.H. Kahana, L. Ludeking and D.J. Millener, Phys. Rev. Lett. 47 (1981), 1110; Ann. of Phys. 148 (1983), 381.

26) D.J. Millner, A. Gal, C.B. Dover and D.H. Dalitz, Phys. Rev. C31 (1985), 499.

27) L. Majling, M. Sotona, J. Zofka, V.N. Fetisov and R.A. Eramzhyan, Phys. Lett. 92B (1980), 256.

L. Majling, J. Zofka, V.N. Fetisov and R.A. Eramzhyan, Phys. Lett. 130B (1983), 235.

28) J. Revai and J. Zofka, Phys. Lett. 101B (1981), 228.

29) Zhang Zong-ye, Li Gaung-lie and Yu You-wen, Phys. Lett. 108B (1982), 261.

30) A.R. Bodmer, Q.N. Usumani and J. Carlson, Nucl. Phys. A222 (1984), 510; Phys. Rev. C29 (1984), 684.

31) R.H. Dalitz and G. Rajasekaran, Nucl. Phys. 50 (1964), 450.

32) A.R. Bodmer and S. Ali, Nucl. Phys. 56 (1964), 657.

33) A.R. Bodmer and J.W. Murphy, Nucl. Phys. 64 (1965), 593;

73 (1965), 664.

34) Y.C. Tang and R.C. Herndon, Phys. Rev. 138 (1965), B637; Nuovo Cim. 66 (1966), 117.

35) Y. Sunami and H. Narumi, Prog. Theor. Phys. 66 (1981), 335.

36) S. Oryu et al., private communication.

37) H. Bandō, M. Seki and Y. Shono, Prog. Theor. Phys. 66 (1981), 2118; 68 (1982), 364 Errata.

38) T. Motoba, H. Bandō and K. Ikeda, Prog. Theor. Phys. 79 (1983), 189; 81 (1984), 222.

39) T. Yamada, K.Ikeda, H. Bandō and T. Motoba, Prog. Theor. Phys. 73 (1985), 397.

40) T. Motoba, H. Bandō, K. Ikeda and T. Yamada, Prog. Theor. Phys. Suppl. No.81 (1985), Chap.III.

41) T. Yamada, K. Ikeda, H. Bandō and T. Motoba, Prog. Theor. Phys. 71 (1984), 985.

42) T. Yamada, T. Motoba, K. Ikeda and H. Bandō, Prog. Theor. Phys. Suppl. No.81 (1985), Chap.IV.

43) H. Bandō, K. Ikeda and T. Motoba, Prog. Theor. Phys. 66 (1981), 1344; 67 (1982), 508.

44) K. Miyahara, K. Ikeda and H. Bandō, Prog. Theor. Phys. 69 (1983), 1717.

45) H. Bandō, Prog. Theor. Phys. 69 (1983), 1731.

46) K. Kobayashi, Master thesis of Niigata University (March, 1984).

47) K. Ikeda, H. Bandō and T. Motoba, Prog. Theor. Phys. Suppl. No.81 (1985), Chap.V.

48) K. Ikeda et al., Prog. Theor. Phys. Suppl. No.52 (1972);

No.68 (1980).

49) For example, Proc. Int. Conf. Clustering Aspects of Nuclear Structure and Nuclear Reactions (Winnipeg, 1978), ed. W.T.H. Van Oers et al. (AIP Conf. Proc. No.47).

50) P.L. Kapur and R.E. Peierls, Proc. Roy. Soc. A166 (1938), 277.

51) Y. Fukushima and M. Kamimura, Proc. Int. Conf. on Nuclear Structure (Tokyo, 1977), ed. T. Marumori, Suppl. of J. Phys. Soc. Jpn. Vol.44, 1978, p.255.

52) Y. Fujiwara, H. Horiuchi, K. Ikeda, M. Kamimura, K. Kato, Y. Suzuki and E. Uegaki, Prog. Theor. Phys. Suppl. No.68 (1980), 29, and references cited therein.

53) H. Horiuchi and K. Ikeda, Prog. Theor. Phys. 40 (1968), 277.

54) F. Nemoto and H. Bandō, Prog. Theor. Phys. 47 (1972), 1210.

55) T. Matsuse, M. Kamimura and Y. Fukushima, Prog. Theor. Phys. 53 (1975), 706.

56) Y. Mito and M. Kamimura, Prog. Theor. Phys. 56 (1970), 583. M. Kamimura, Prog. Theor. Phys. Suppl. No.62 (1977), 236.

57) A.B. Volkov, Nucl. Phys. 74 (1965), 33.

58) J. Hiura and R. Tamagaki, Prog. Theor. Phys. Suppl. No.52 (1972),25.

59) H. Bandō, K. Ikeda and T. Motoba, Prog. Theor. Phys. 69 (1983), 918.

60) C. Bloch, Nucl. Phys. 4 (1957), 503.

61) J. Hüfner, S.Y. Lee and H.A. Weidenmuller, Nucl. Phys. A234 (1974), 429; Phys. Lett. 49B (1974), 409.

62) A. Boussy, Nucl. Phys. A290 (1977), 324; Phys. Lett. 84B (1979), 41; 99B (1981), 373.

63) S. Okabe, Y. Abe and H. Tanaka, Prog. Theor. Phys. 57 (1977), 866.

64) M. Kamimura, Nucl. Phys. A351 (1981), 456.

65) For example, N.K. Glendenning, Phys. Rev. 137 (1965), B102.

66) H. Horiuchi, K. Ikeda and Y. Suzuki, Prog. Theor. Phys. Suppl. No.52 (1972), Chap.III, p.89.

67) A. Tohsaki-Suzuki, Prog. Theor. Phys. Suppl. No.62 (1977), 191.

Table I

Squared overlaps $P^{(\beta)}_{n,N}$ of the three-channel coupled wf $\Psi_{BSA}(L_N)$ (N=I,II,III) with the single-channel wf $\Phi^{(\beta)}_{BSA}(L_n)$ (n=1,2) (or wf $\Phi^{(2+3)}_{BSA}(L_n)$ (n=1,2) obtained by the $\Lambda+^8Be(0^+)$ and $\Lambda+^8Be(2^+)$ two-channel coupled problem). The definition is given in Eq.(2.19).

		Three-channel coupled wf's $\Psi_{BSA}(L_N)$		
		$L^\pi=1^-_I$	$L^\pi=1^-_{II}$	$L^\pi=1^-_{III}$
	(E_Λ MeV)	(-0.5 MeV)	(3.7 MeV)	(5.0 MeV)
$\Phi^{(1)}_{BSA}$: $^5_\Lambda$He+α	$L_n=1^-_1$	0.980	0.003	0.004
	1^-_2	0.001	0.941	0.053
$\Phi^{(2)}_{BSA}$: $\Lambda+^8Be(0^+)$	1^-_1	0.387	0.119	0.447
	1^-_2	0.053	0.008	0.145
$\Phi^{(3)}_{BSA}$: $\Lambda+^8Be(2^+)$	1^-_1	0.338	0.000	0.341
	1^-_2	0.029	0.018	0.000
$\Phi^{(2+3)}_{BSA}$: $\Lambda+^8Be(0^+,2^+)$	1^-_1	0.795	0.093	0.012
	1^-_2	0.014	0.035	0.920

Table II

Calculated energy eigenvalues $W_n(E_\alpha)$ and the squared transition matrix elements $N_n(E_\alpha)$ for p_{K^-} = 790 MeV/c and θ_{π^-} = 0°, where E_α corresponds to the energy E in Eq.(2.24) measured with respect to the ${}^{5}_{\Lambda}$He+α threshold energy (E_α and W_n in MeV).

E_α		n=1	n=2	n=3
2.0	W_n	1.74 - 0.41i	5.37 - 1.37i	7.21 - 0.04i
	N_n	0.01 - 0.00i	0.02 - 0.01i	0.21 + 0.01i
6.0	W_n	2.08 - 0.49i	6.60 - 3.03i	7.24 - 1.65i
	N_n	0.01 - 0.00i	0.01 - 0.01i	0.24 - 0.11i
10.0	W_n	2.22 - 0.44i	7.93 - 3.19i	8.03 - 2.21i
	N_n	0.01 + 0.00i	-0.01 - 0.01i	0.27 - 0.11i

Table III

Calculated energies ("Full") of the band head states in which the Λ particle occupies mainly the $(0s)_\Lambda$ state. In order to study the effects of channel couplings, the results with only the main channel ("NO") are presented. The energies are measured with respect to the Λ-^{12}C(g.s.) threshold.

L^π	Main channel	Full (MeV)	NO (MeV)
0^+_I	$\left[{}^{12}C(0^+_1)\otimes s_\Lambda \right]$	-11.31	-10.11
2^+_I	$\left[{}^{12}C(2^+_1)\otimes s_\Lambda \right]$	- 6.87	- 6.12
4^+_I	$\left[{}^{12}C(4^+_1)\otimes s_\Lambda \right]$	1.73	2.11
0^+_{II}	$\left[{}^{12}C(0^+_2)\otimes s_\Lambda \right]$	3.36	4.85
2^+_{II}	$\left[{}^{12}C(2^+_2)\otimes s_\Lambda \right]$	8.04	8.80
3^-_I	$\left[{}^{12}C(3^-_1)\otimes s_\Lambda \right]$	2.76	3.35
1^-_{II}	$\left[{}^{12}C(1^-_1)\otimes s_\Lambda \right]$	6.43	7.36

Table IV

Estimates of root-mean-square radii of the 3α nuclear part ($\sqrt{\langle r^2\rangle}_{3\alpha}$) and Λ-3α relative coordinate ($\sqrt{\langle R^2\rangle}_{3\alpha-\Lambda}$) for the positive and negative parity states in ${}^{13}_{\Lambda}C$. The values in the parentheses are for ${}^{12}C$.

K^π	Main configuration	L^π	$\sqrt{\langle r^2\rangle}_{3\alpha}$ (fm)	$\sqrt{\langle R^2\rangle}_{3\alpha-\Lambda}$ (fm)
0^+_I	$\left[{}^{12}C(k^\pi=0^+_1)\otimes(0s)_\Lambda \right]$	0^+	2.39 (2.42)	2.17
		2^+	2.38 (2.38)	2.17
		4^+	2.30 (2.30)	2.07
0^+_{II}	$\left[{}^{12}C(k^\pi=0^+_2)\otimes(0s)_\Lambda \right]$	0^+	3.48 (3.55)	3.24
		2^+	3.62 (3.91)	3.70
3^-_I	$\left[{}^{12}C(k^\pi=3^-_1)\otimes(0s)_\Lambda \right]$	3^-	2.80 (2.77)	2.56
1^-_{II}	$\left[{}^{12}C(k^\pi=1^-_1)\otimes(0s)_\Lambda \right]$	1^-	3.19 (3.38)	3.16
1^-_I	$\left[{}^{12}C(k^\pi=0^+)\otimes(0p)_\Lambda \right]$	1^-	2.41	3.34
		2^-	2.38	3.25
		3^-	2.38	3.48
		4^-	2.30	3.21
		5^-	2.31	3.65
0^-_I	$\left[{}^{12}C(k^\pi=0^+)\otimes(0p)_\Lambda \right]$	1^-	2.66	3.92
		3^-	2.35	4.31

	1^-	3.57	4.22
1^-_{III} $\left[{}^{12}C(k^\pi=0^+_2)\otimes(0p)_\Lambda \right]$	2^-	3.80	4.55
	3^-	3.26	4.77
0^-_{II} $\left[{}^{12}C(k^\pi=0^+_2)\otimes(0p)_\Lambda \right]$	1^-	3.76	4.53
0^+_{III} $\left[{}^{12}C(k^\pi=0^+_1)\otimes(1s)_\Lambda \right]$	0^+	2.53 (2.42)	4.46
	2^+	2.53 (2.38)	4.51

Table V

Harmonic oscillator expansions of the Λ-particle wave functions in the low-lying states (L=0∿2) of ${}^{17}_{\Lambda}O$ and L=0 of ${}^{5}_{\Lambda}He$. The h.o. node is denoted by n.

	${}^{16}O-\Lambda$				$\alpha-\Lambda$
	$L=0^+$	$L=1^-$	$L=0_2^+$	$L=2^+$	$L=0^+$
$-B_\Lambda$	-14.83	-2.37	1.85	4.19	-3.12
n=0	0.998	0.953	0.041	0.440	0.973
1	-0.014	-0.194	0.556	-0.371	-0.074
2	0.052	0.182	-0.426	0.404	0.204
3	-0.018	-0.104	0.421	-0.390	-0.034
4	0.004	0.071	-0.365	0.361	0.059
⋮	⋮	⋮	⋮	⋮	⋮

Table VI

Calculated energies of the positive parity band head states in ${}^{21}_{\Lambda}\mathrm{Ne}(L^+)$ and their channel probabilities W_c^2. The angular momentum channel is denoted by $c=(\ell,\lambda)$. The parity coupling "FULL" represents the results with both positive and negative parity channels of the α-${}^{16}\mathrm{O}$ states, while "NO" those with only leading parity channels.

$L^+=K^+$	Parity Coupling	$-E_\Lambda$ (MeV)	W_c^2 (0, 0)	(2, 2)	(4, 4)	(1, 1)	(3, 3)
0^+_{I}	FULL	-17.2	.980	.005	.000	.015	.000
	NO	-16.9	.996	.004	.000	-	-
0^+_{II}	FULL	-7.6	.807	.016	.000	.176	.001
	NO	-5.5	.993	.007	.000	-	-
0^+_{III}	FULL	-1.1	.749	.023	.000	.229	.000
	NO	1.8	.985	.014	.000	-	-
0^+_{IV}	FULL	-0.1	.323	.059	.006	.589	.023
1^+_{I}	FULL	1.6	-	.142	.000	.851	.006
0^+_{V}	FULL	0.7	.636	.142	.001	.217	.003
	NO	0.5	.826	.170	.004	-	-
0^+_{VI}	FULL	3.3	.285	.697	.007	.010	.002
	NO	3.4	.264	.730	.006	-	-

Table VII

Spectroscopic factors S^2 of the positive parity states in ${}^{21}_{\Lambda}Ne(L^+)$ leading to the three decay channels. For comparision, calculated S^2-factors for the corresponding $\alpha+{}^{16}O$ decay of ${}^{20}Ne$ are also given in the right hand side of Table. The SU(3) shell-model limit values are inserted for typical cases.

K^π	L^+	$\alpha+{}^{17}_{\Lambda}O(s)$	$\alpha+{}^{17}_{\Lambda}O(p)$	${}^{5}_{\Lambda}He+{}^{16}O$	${}^{20}Ne\to\alpha+{}^{16}O$
SU(3) limit		(.205)		(.045)	(.23)
$K^\pi=0^+_I$	0	.255	.051	.056	.39
$\left(0^+_1\otimes 0s_\Lambda\right)$	2	.254	.050	.052	.38
	4	.248	.047	.051	.36
	6	.236	.039	.049	.33
	8	.219	.029	.046	.27
$K^\pi=0^+_{II}$	0	.226	.182	.013	.73
$\left(0^+_2\otimes 0s_\Lambda\right)$	2	.255	.214	.014	.77
	4	.278	.237	.014	.80
	6	.292	.256	.014	.82
	8	.296	.281	.013	.86
$K^\pi=0^+_{III}$	0	.105	.084	.007	-
$\left(0^+_3\otimes 0s_\Lambda\right)$	2	.126	.106	.007	-

$K^{\pi}=0^{+}_{IV}$	0	.168	.243	.334	.65
$\left(0^{-}_{1}\otimes 0p_{\Lambda}\right)$	2	.229	.212	.262	.65
	4	.222	.176	.173	.65
	6	.204	.123	.117	.65
$K^{\pi}=1^{+}$	1	-	.329	-	.65
$\left(0^{-}_{1}\otimes 0p_{\Lambda}\right)$	2	.229	.214	.024	-
	3	-	.312	-	.65
	4	.036	.337	.014	-
	5	-	.231	-	.65
SU(3) limit		(.069)	(.002)		
$K^{\pi}=0^{+}_{V}$	0	.108	.003	.000	-
$\left(0^{+}_{1}\otimes 1s_{\Lambda}\right)$	2	.010	.080	.057	-
	4	.002	.115	.144	-
$K^{\pi}=0^{+}_{VI}$	0	.000	.018	.025	-
$\left(0^{+}_{1}\otimes 0d_{\Lambda}\right)$	2	.002	.124	.008	-
	4	.021	.010	.013	-

Table VIII

Particle-decay widths of the typical states in $^{21}_{\Lambda}Ne(L^{\pi})$. Energetically forbidden channels are marked by asterisks. The values in the parentheses are for the levels which energies are higher than the corresponding Coulomb barrier.

K^{π}	L	$\alpha+^{17}_{\Lambda}O(s)$	$^{20}Ne+\Lambda$	$\alpha+^{17}_{\Lambda}O(p)$	$^{5}_{\Lambda}He+^{16}O$
$K^{\pi}=0^{+}_{I}$	8	0.00 (MeV)	*	*	*
$K^{\pi}=0^{+}_{II}$	0	0.69	*	*	*
	2	0.69	*	*	*
	4	0.70	*	*	*
	6	0.83	*	*	*
	8	0.84	0.00	0.00	0.00
$K^{\pi}=0^{+}_{IV}$	0	(1.42)	*	*	*
	2	(1.76)	0.00	*	*
	4	(1.59)	0.01	0.00	0.01
	6	(1.21)	0.08	0.01	0.02
$K^{\pi}=1^{+}$	1	-	0.00	*	*
	2	(0.45)	0.32	0.00	0.02
	3	-	0.06	0.01	*
	4	(0.50)	0.82	0.26	0.05

$K^{\pi}=0^{+}_{V}$	0	(1.03)	0.65	*	*
	2	(0.30)	0.69	*	0.00
	4	(0.00)	0.74	0.00	0.04
$K^{\pi}=0^{+}_{VI}$	0	(0.00)	1.16	0.03	0.12
	2	(0.01)	1.87	0.11	0.00
$K^{\pi}=0^{-}_{I}$	3	0.00	*	*	*
	5	0.05	*	*	*
	7	(0.12)	*	*	*
	9	(0.09)	0.00	0.00	0.00
$K^{\pi}=0^{-}_{II}$	1	0.61	*	*	*
	3	(0.53)	*	*	*
	5	(0.39)	*	*	*
	7	(0.19)	0.00	*	0.00
$K^{\pi}=1^{-}$	1	(0.00)	*	*	*
	2	-	*	*	-
	3	(0.14)	*	*	*
	4	-	*	*	-

Table IX

Calculated energies of the negative parity band head states in $^{21}_{\Lambda}Ne(L^-)$ and their channel probabilities W_c^2. Comments as for Table VI.

$L^-(K^-)$	Parity Coupling	$-E_\Lambda$ (MeV)	W_c^2 (0, 1)	(2, 1)	(2, 3)	(1, 0)	(1, 2)	(3, 2)
$1^-(0^-_I)$	FULL	-11.5	.051	.084	.004	.856	.004	.004
	NO	-10.1	-	-	-	.994	.003	.003
$1^-(0^-_{II})$	FULL	-5.0	.487	.395	.009	.097	.001	.002
	NO	-5.5	.486	.499	.008	-	-	-
$1^-(0^-_{III})$	FULL	-4.3	.078	.124	.001	.775	.010	.012
	NO	-1.1	-	-	-	.993	.003	.004
$1^-(1^-)$	FULL	-3.0	.451	.526	.000	.006	.009	.005
	NO	-2.8	.508	.490	.000	-	-	-

Table X

Spectroscopic factors S^2 of the positive parity states in $^{21}_{\Lambda}Ne(L^-)$ leading to the three decay channels. Comments as for Table VII.

K^π	L^-	$\alpha+^{17}_{\Lambda}O(s)$	$\alpha+^{17}_{\Lambda}O(p)$	$^{5}_{\Lambda}He+^{16}O$	$^{20}Ne\rightarrow\alpha+^{16}O$
SU(3) limit		(.303)		(.056)	(.34)
$K^\pi=0^-_I$	1	.295	.182	.025	.65
$\left(0^-_1\otimes 0s_\Lambda\right)$	3	.298	.186	.024	.65
	5	.295	.185	.023	.65
	7	.281	.188	.019	.65
	9	.181	.197	.003	.65
SU(3) limit		(.026)		(.075)	
$K^\pi=0^-_{II}$	1	.143	.147	.168	-
$\left(0^+_1\otimes 0p_\Lambda\right)$	3	.135	.150	.149	-
	5	.132	.190	.144	-
	7	.132	.124	.136	-
	9	.218	.059	.137	-
$K^\pi=0^-_{III}$	1	.141	.116	.010	-
$\left(0^-_2\otimes 0s_\Lambda\right)$	3	.173	.159	.009	-
	5	.199	.199	.008	-
	7	.218	.228	.010	-
	9	.286	.242	.011	-

$K^{\pi}=1^{-}$	1	.004	.283	.004	-
$\left(0_1^{+}\otimes 0p_{\Lambda}\right)$	2	-	.286	-	-
	3	.016	.265	.013	-
	4	-	.276	-	-
	5	.014	.246	.010	-
	6	-	.257	-	-
	7	.009	.222	.005	-

Figure Captions

Fig. 1 Excitation function of the forward $^{9}Be(K^{-},\pi^{-})^{9}_{\Lambda}Be$ reaction for p_{K^-} = 790 MeV/c [7].

Fig. 2 Energy spectra of $^{9}_{\Lambda}Be$ calculated by the microscopic $\alpha+\alpha+\Lambda$ cluster model under the bound state approximation (BSA)[37),38),40]. Three particle-decay thresholds are indicated by the arrows.

Fig. 3 (a) The basic coordinate system adopted to describe the $^{5}_{\Lambda}He+\alpha$ channel. The other coordinate systems, (b) and (c), are also used to represent the $\Lambda+^{8}Be(0^{+})$ and $\Lambda+^{8}Be(2^{+})$ channels, respectively.

Fig. 4 Calculated phase shifts for the $L^{\pi}=1^{-}$ partial waves of three independent $^{5}_{\Lambda}He+\alpha$, $\Lambda+^{8}Be(0^{+})$ and $\Lambda+^{8}Be(2^{+})$ channels without channel couplings.

Fig. 5 Folding potentials for the $\Lambda-^{8}Be(0^{+})$ (dotted line) and $\Lambda+^{8}Be(2^{+})$ (solid line) channels.

Fig. 6 Calculated cross sections for the incident $^{5}_{\Lambda}He+\alpha$ (Fig.6(a)) and $\Lambda+^{8}Be(0^{+})$ (Fig.6(b)) channels with respect to the α-particle energy (E_{α}) and Λ-particle energy (E_{Λ}) (E_{Λ}; $E_{\alpha} = E_{\Lambda} + 2.5$ MeV) in the CM frame. The channels 1, 2 and 3 represent the $^{5}_{\Lambda}He+\alpha$, $\Lambda+^{8}Be(0^{+})$ and $\Lambda+^{8}Be(2^{+})$, respectively.

Fig. 7 Calculated absolute values of the S-matrix elements for the incident $^{5}_{\Lambda}He+\alpha$ (Fig.7(a)) and $\Lambda+^{8}Be(0^{+})$ (Fig.7(b)) channels. Comments as for Fig.6.

Fig. 8 Energy dependence of the eigenvalues $W_{n}(E_{\alpha})$ =

$\varepsilon_n(E_\alpha) - \Gamma_n(E_\alpha)/2$ (See Eq.(2.31)), where E_α corresponds to the energy E in Eq.(2.24) measured with respect to the ${}^{5}_{\Lambda}\mathrm{He}+\alpha$ threshold energy.

Fig. 9 Calculated strength function S(E) for the ${}^{9}\mathrm{Be}(K^-,\pi^-){}^{9}_{\Lambda}\mathrm{Be}$ reaction with p_{K^-} = 790 MeV/c. Three cases of the π^- direction θ_π = 0°, 5° and 10° are plotted against the hypernuclear energy E (E_α and E_Λ measured from the ${}^{5}_{\Lambda}\mathrm{He}+\alpha$ and the $\Lambda+{}^{8}\mathrm{Be}(0^+)$ thresholds, respectively).

Fig. 10 Experimental energy spectra of ${}^{12}\mathrm{C}$ and the calculated one by the microscopic 3α RGM[51),52)]. The level energies are measured with respect to the ${}^{8}\mathrm{Be}(0^+)+\alpha$ threshold.

Fig. 11 Calculated energy spectra and B(E2) values (in e^2fm^4) of ${}^{12}\mathrm{C}$ by the microscopic 3α RGM[51),52)]. The solid lines correspond to the observed levels shown in Fig.10.

Fig. 12 Density distributions for the $\ell^\pi = 0^+_1, 2^+_1, 4^+_1, 0^+_2, 2^+_2, 1^-_1$ and 3^-_1 states of ${}^{12}\mathrm{C}$ calculated by the microscopic 3α RGM[64)] and the corresponding s-wave folding potentials for $\Lambda-{}^{12}\mathrm{C}(\ell^\pi)$. The energies of each eigenstates are also shown.

Fig. 13 Calculated energy spectra and B(E2) values (in e^2fm^4) of ${}^{13}_{\Lambda}\mathrm{C}$. The level energies are measured with respect to the $\Lambda+{}^{12}\mathrm{C}$ threshold. For comparision the energy spectra of ${}^{12}\mathrm{C}$ are displayed.

Fig. 14 Diagonal (solid lines) and non-diagonal (dotted lines) folding potentials between ${}^{12}\mathrm{C}$ and Λ for the $(i\ell,\lambda)_L\pi$ =

$(1^-_1, s_\Lambda)_{1^-}$, $(0^+_1, p_\Lambda)_{1^-}$ and $(2^+_1, p_\Lambda)_{1^-}$ channels.

Fig. 15 Diagonal and non-diagonal folding potentials between ^{12}C and Λ for the $(i\ell,\lambda)_L{}^\pi = (0^+_2, p_\Lambda)_{1^-}$ and $(2^+_2, p_\Lambda)_{1^-}$ channels.

Fig. 16 Summary of the rotational bands in ^{20}Ne. The left three of the six observed bands are concerned with the $\alpha+^{16}O$ di-cluster model which produces the three bands in the right side. The energies are measured with respect to the $\alpha+^{16}O$ threshold.

Fig. 17 (a) The basic coordinate system adopted to describe the three-cluster wave function for $^{21}_{\Lambda}Ne$. The other two coordinate, (b) and (c), are also used in treating the $\alpha+^{17}_{\Lambda}O$ and $^{5}_{\Lambda}He+^{16}O$ decay channels.

Fig. 18 Calculated energy spectra and B(E2) values (in e^2fm^4) of the positive parity states in $^{21}_{\Lambda}Ne$. The level energies are measured with respect to the $^{20}Ne+\Lambda$ threshold. For comparision the calculated ground band of ^{20}Ne is inserted with the $\alpha+^{16}O$ threshold referring to the $\alpha+^{17}_{\Lambda}O$ threshold of $^{21}_{\Lambda}Ne$.

Fig. 19 Estimates of the root-mean-square radius $\sqrt{\langle r^2 \rangle}$ between α and ^{16}O clusters within each K^π band of $^{21}_{\Lambda}Ne$. Those for the $K^\pi=0^+_1$, 0^+_2 and 0^- band members of ^{20}Ne are shown for comparision.

Fig. 20 Calculated reduced width amplitudes (RWA) of the band head 0^+ states in $^{21}_{\Lambda}Ne$ leading to the $\alpha+^{17}_{\Lambda}O(s)$ and $^{5}_{\Lambda}He+\alpha$ channels. For comparision the RWA's of $\ell^\pi=0^+_1$ and 0^+_2 states in ^{20}Ne are also shown.

Fig. 21 Calculated energy spectra and B(E2) values of the negative parity states in $^{21}_{\Lambda}$Ne. Comments as for Fig.18.

Fig. 22 Same as Fig.20 except for the negative parity states in $^{21}_{\Lambda}$Ne and ^{20}Ne.

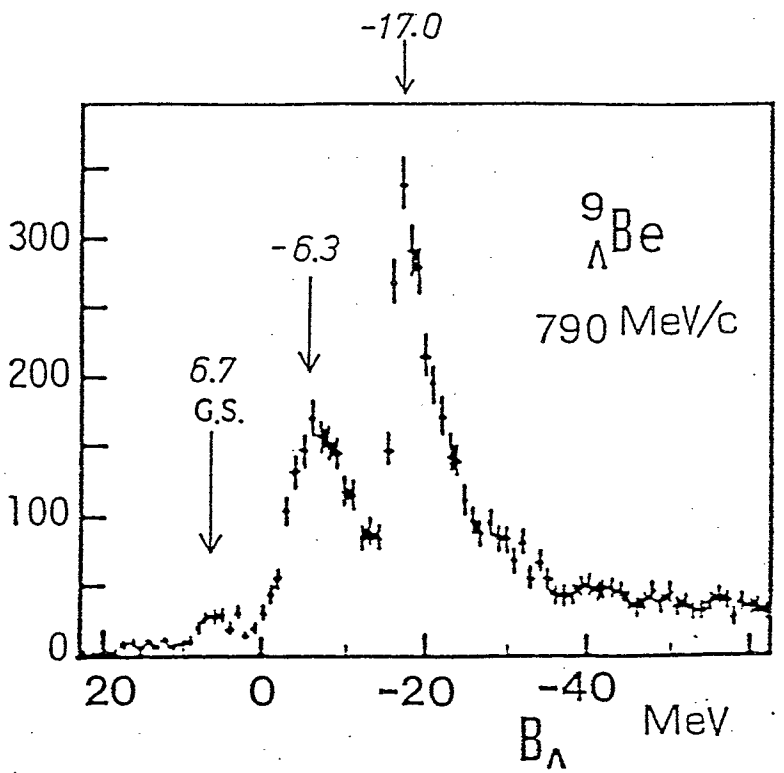
-17.0
-6.3
6.7
G.S.
300
200
100
0
20
0
-20
-40
MeV
B_Λ
$^{9}_{\Lambda}Be$
790 MeV/c

Fig.1

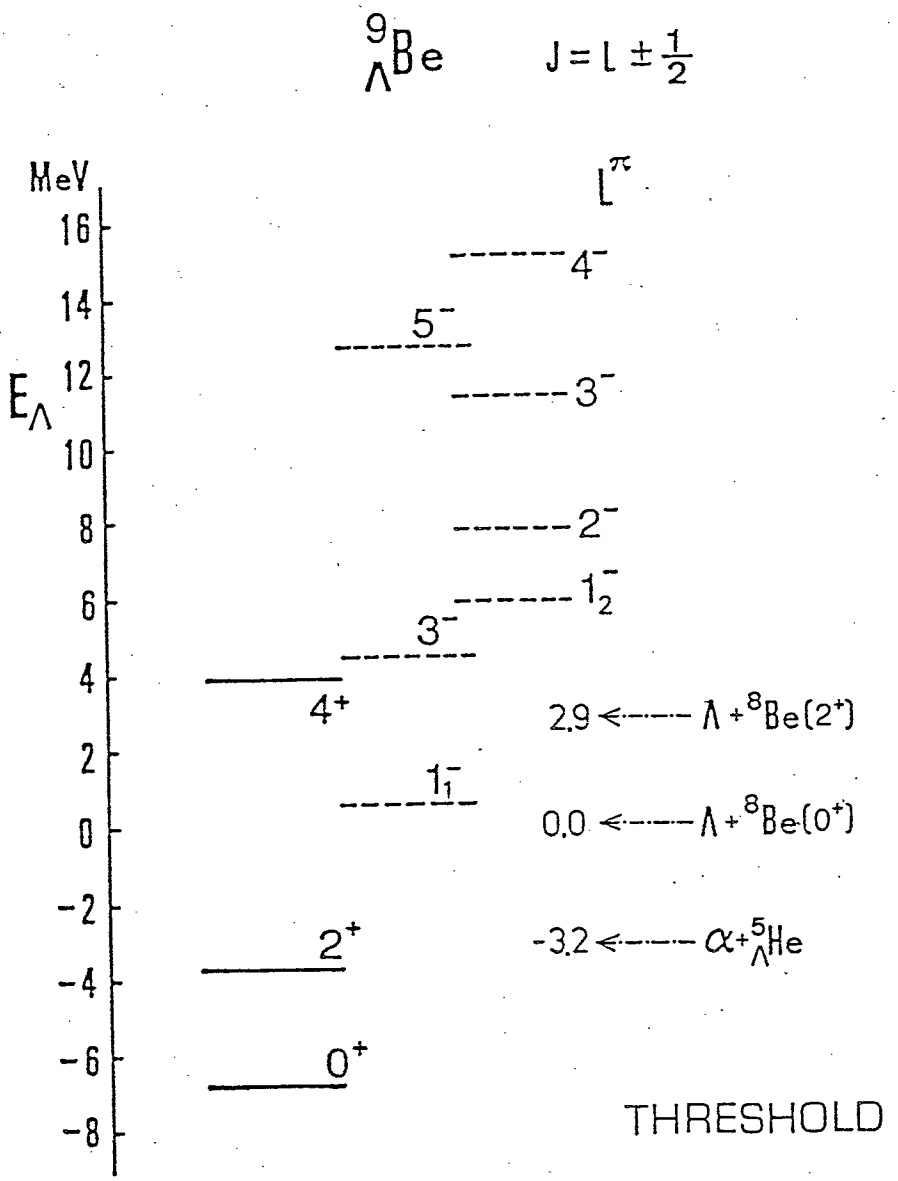
$^{9}_{\Lambda}Be$ $J = l \pm \frac{1}{2}$
MeV
E_Λ
16
14
12
10
8
6
4
2
0
-2
-4
-6
-8
l^π
4^-
5^-
3^-
2^-
1_2^-
3^-
4^+
1_1^-
2^+
0^+
2.9 ← $\Lambda + {}^{8}Be(2^+)$
0.0 ← $\Lambda + {}^{8}Be(0^+)$
-3.2 ← $\alpha + {}^{5}_{\Lambda}He$
THRESHOLD

Fig.2

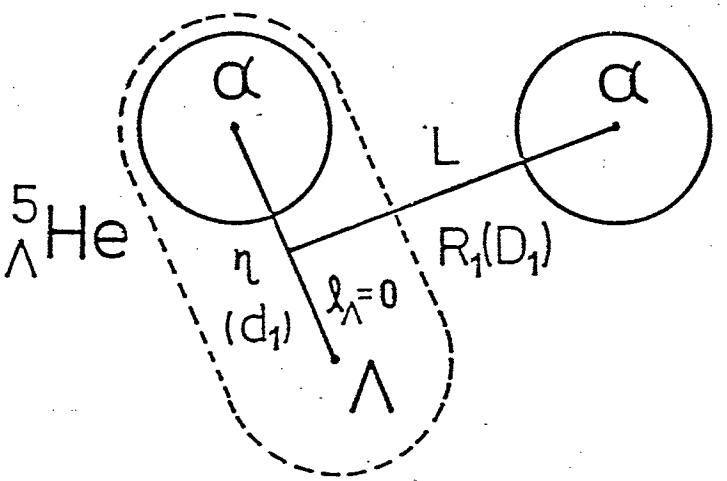
α
α
L
$^{5}_{\Lambda}$He
η
(d_1)
ℓ_Λ=0
$R_1(D_1)$
Λ

(a)

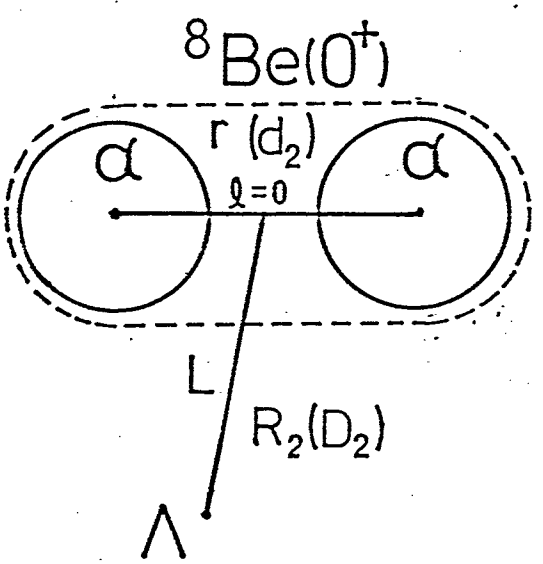
^{8}Be(0^+)
r (d_2)
α
α
ℓ=0
L
$R_2(D_2)$
Λ

(b)

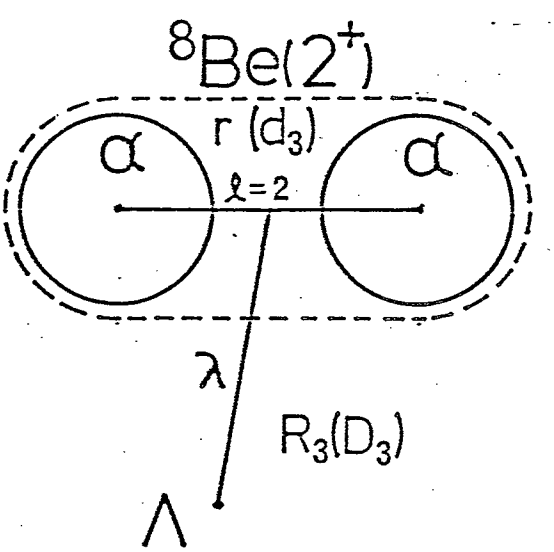
^{8}Be(2^+)
r (d_3)
α
α
ℓ=2
λ
$R_3(D_3)$
Λ

(c)

Fig.3

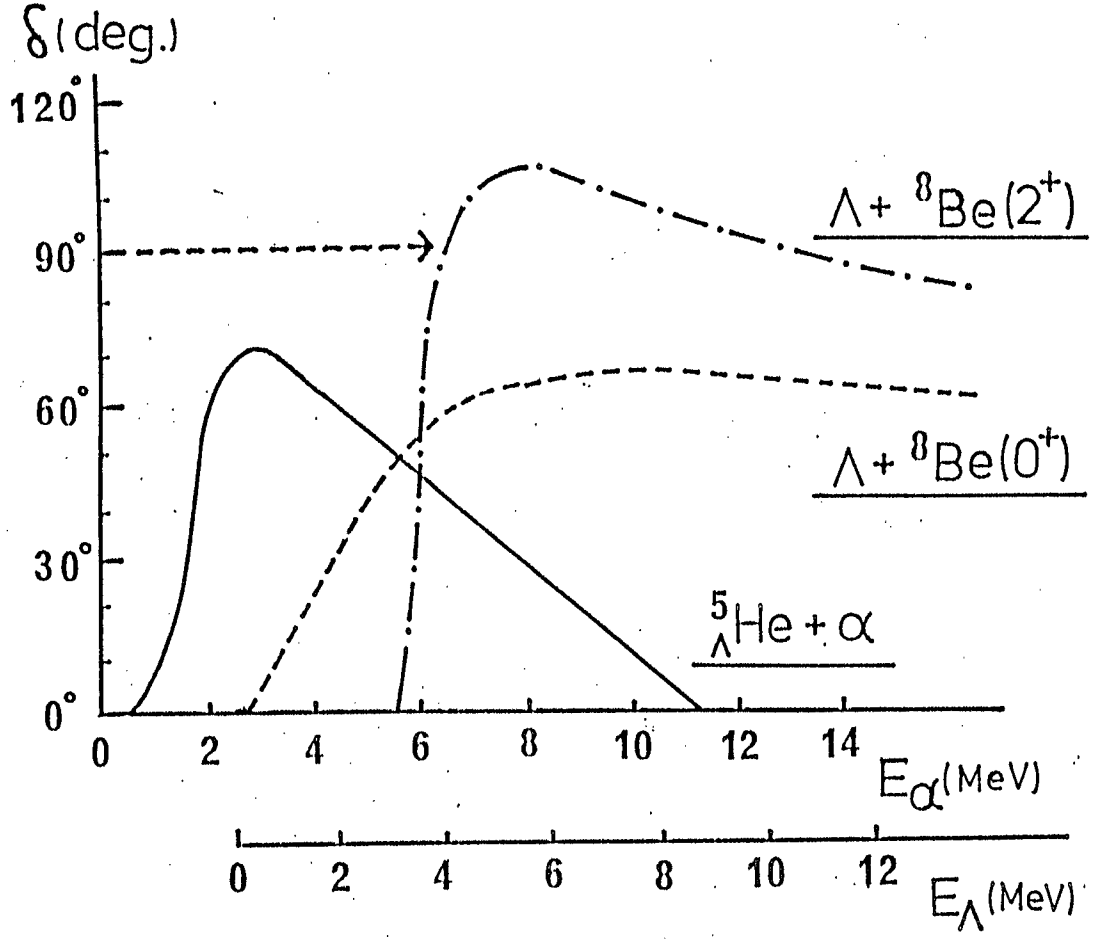
δ(deg.)
120°
90°
60°
30°
0°
Λ+ ⁸Be(2⁺)
Λ+ ⁸Be(0⁺)
⁵ΛHe + α
0
2
4
6
8
10
12
14
Eα(MeV)
0
2
4
6
8
10
12
EΛ(MeV)

Fig.4

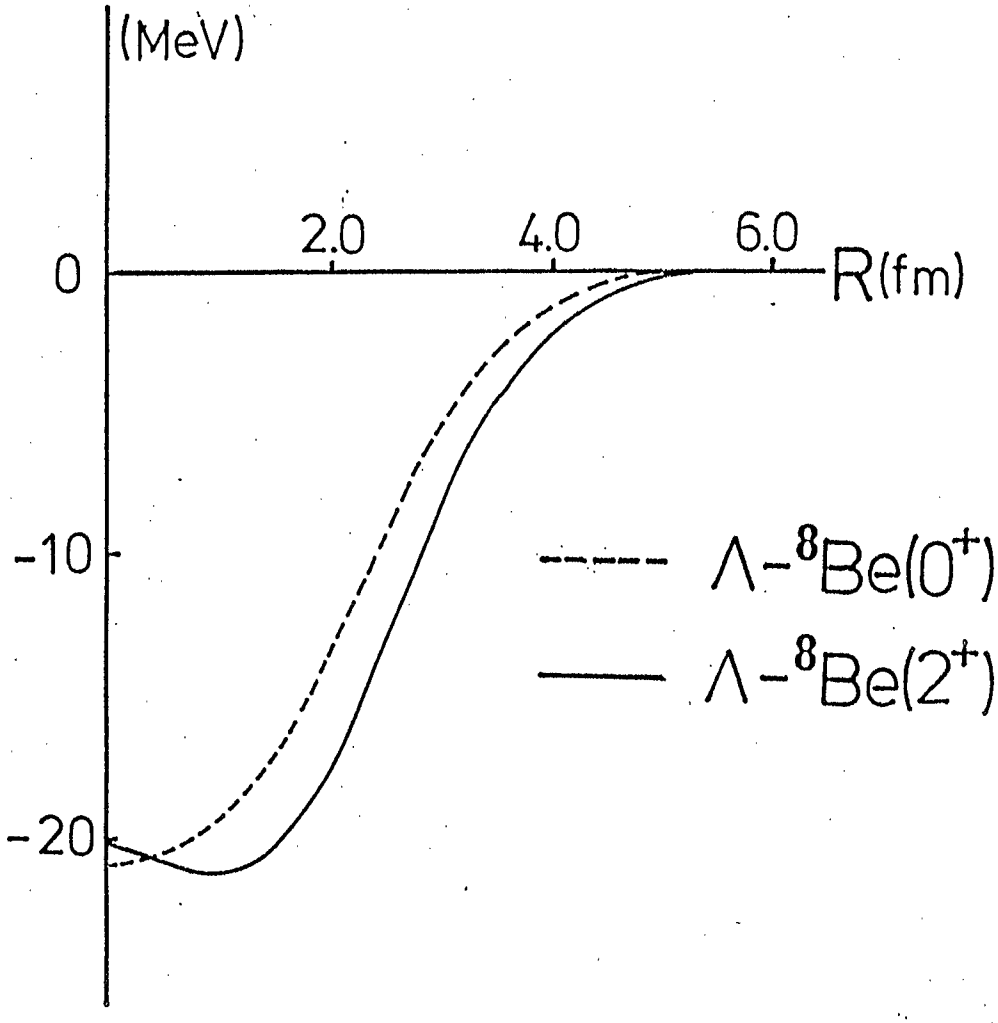

Fig.5

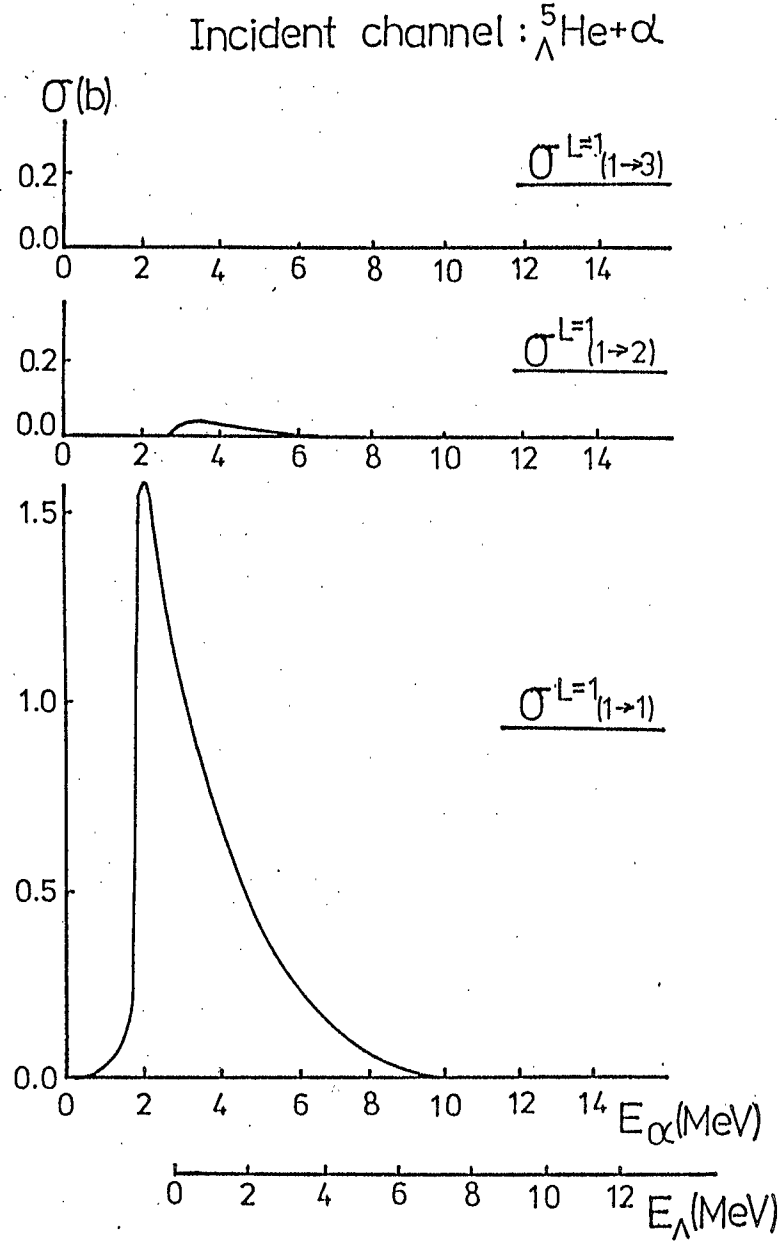
Incident channel : $^{5}_{\Lambda}$He+α
σ(b)
$\sigma^{L=1}_{(1\to3)}$
$\sigma^{L=1}_{(1\to2)}$
$\sigma^{L=1}_{(1\to1)}$
E_α(MeV)
E_Λ(MeV)

Fig.6(a)

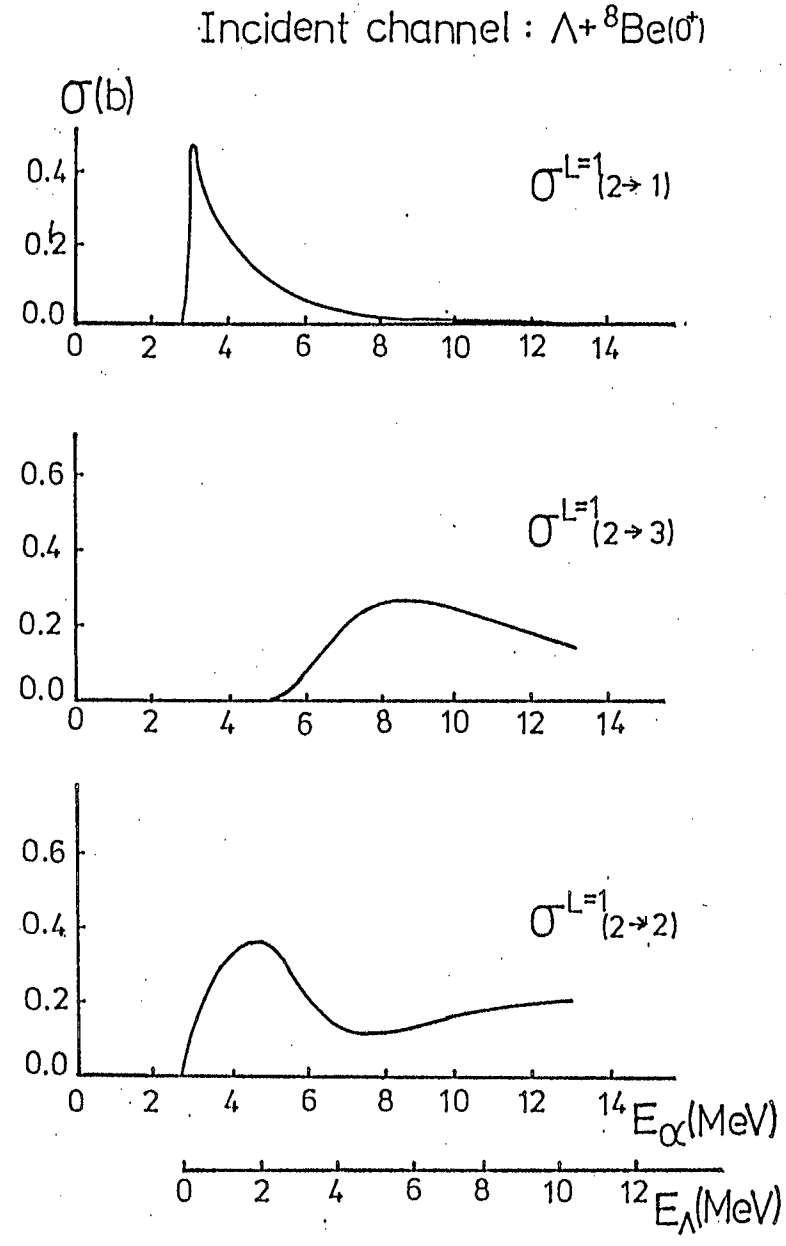
Incident channel : Λ+^{8}Be(0^{+})
σ(b)
$\sigma^{L=1}_{(2\to1)}$
$\sigma^{L=1}_{(2\to3)}$
$\sigma^{L=1}_{(2\to2)}$
E_α(MeV)
E_Λ(MeV)

Fig.6(b)

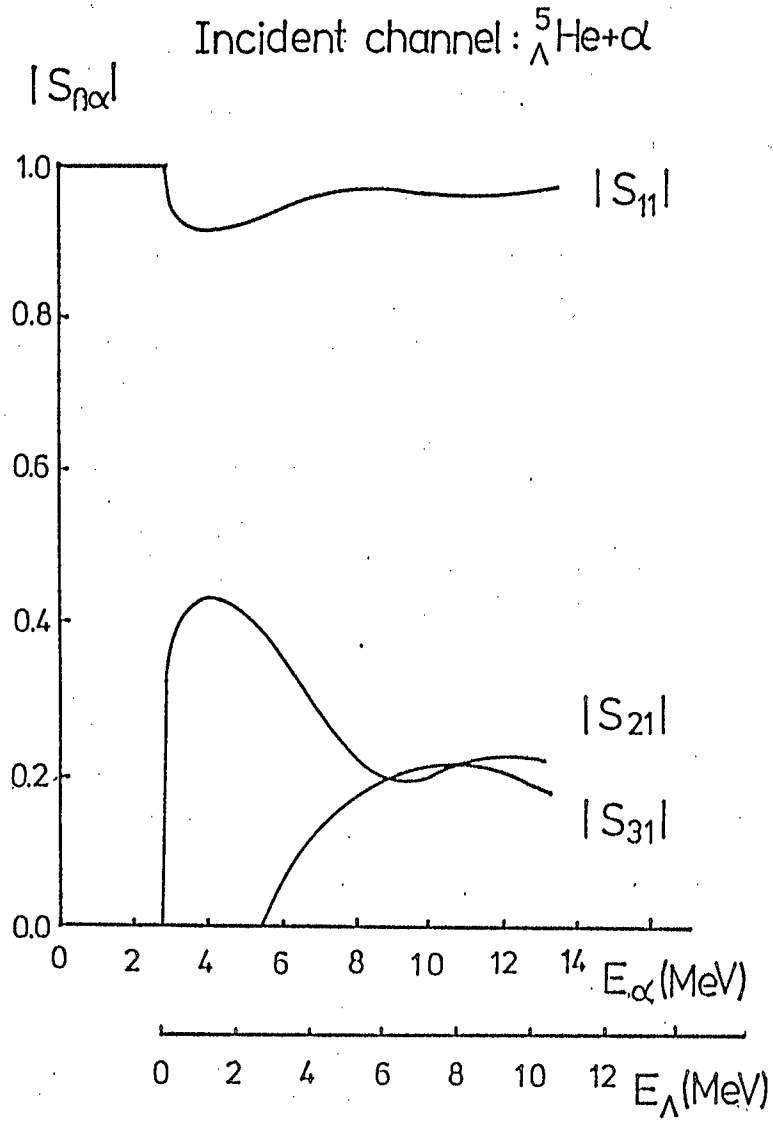
Incident channel : $^{5}_{\Lambda}$He+α
$|S_{\beta\alpha}|$
1.0
0.8
0.6
0.4
0.2
0.0
$|S_{11}|$
$|S_{21}|$
$|S_{31}|$
0 2 4 6 8 10 12 14 E_α(MeV)
0 2 4 6 8 10 12 E_Λ(MeV)

Fig.7(a)

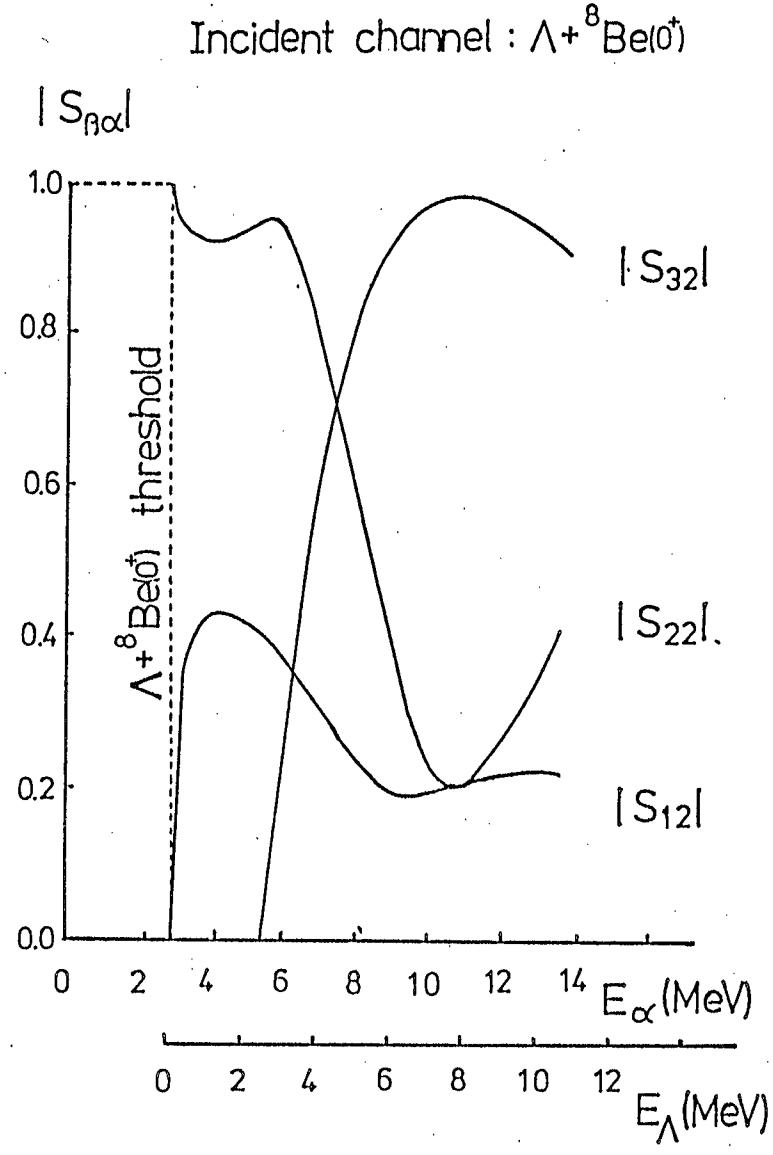
Incident channel : Λ+^{8}Be(0^{+})
$|S_{\beta\alpha}|$
1.0
0.8
0.6
0.4
0.2
0.0
Λ+^{8}Be(0^{+}) threshold
$|S_{32}|$
$|S_{22}|$
$|S_{12}|$
0 2 4 6 8 10 12 14 E_α(MeV)
0 2 4 6 8 10 12 E_Λ(MeV)

Fig.7(b)

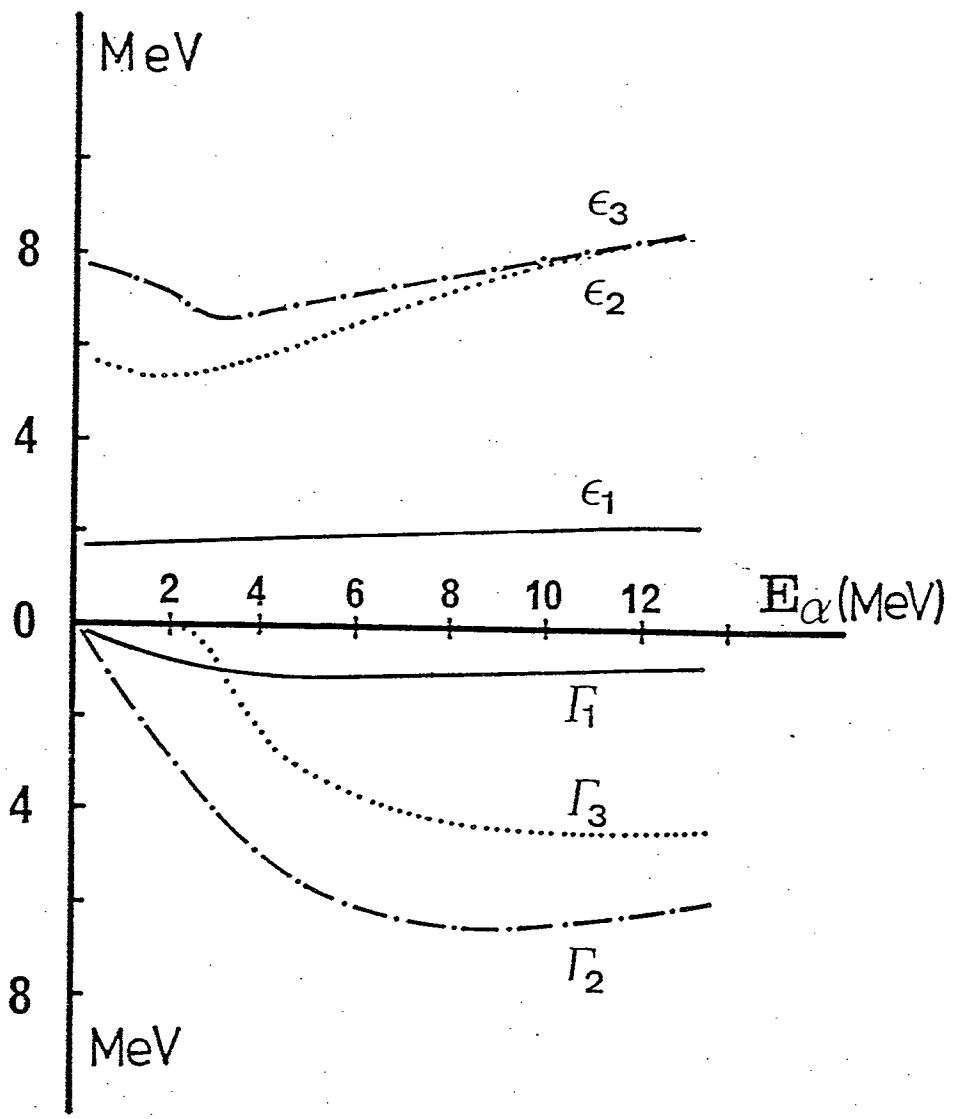
MeV
8
4
0
4
8
MeV
ϵ_3
ϵ_2
ϵ_1
2
4
6
8
10
12
E_α(MeV)
Γ_1
Γ_3
Γ_2

Fig. 8

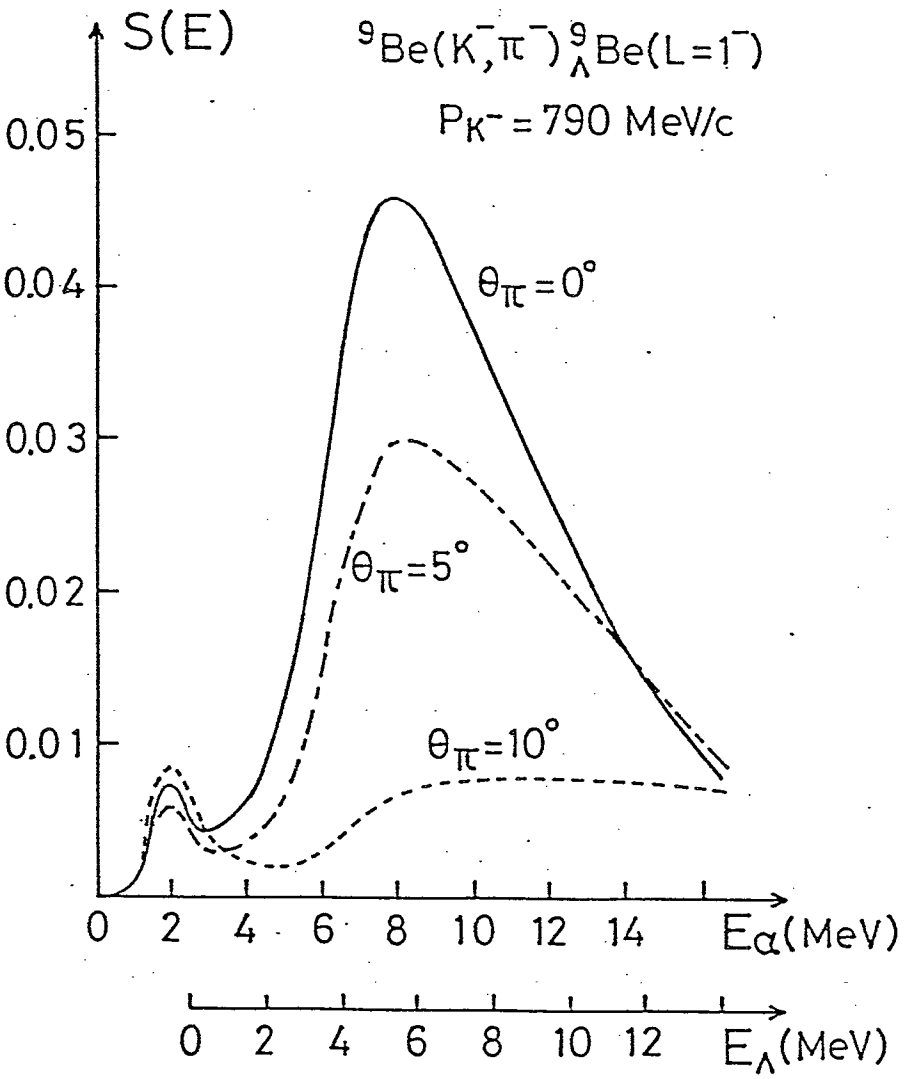
S(E)
$^{9}Be(K^{-},\pi^{-})^{9}_{\Lambda}Be(L=1^{-})$
P_{K^-} = 790 MeV/c
0.05
0.04
0.03
0.02
0.01
$\theta_\pi = 0°$
$\theta_\pi = 5°$
$\theta_\pi = 10°$
0 2 4 6 8 10 12 14 E_α(MeV)
0 2 4 6 8 10 12 E_Λ(MeV)

Fig.9

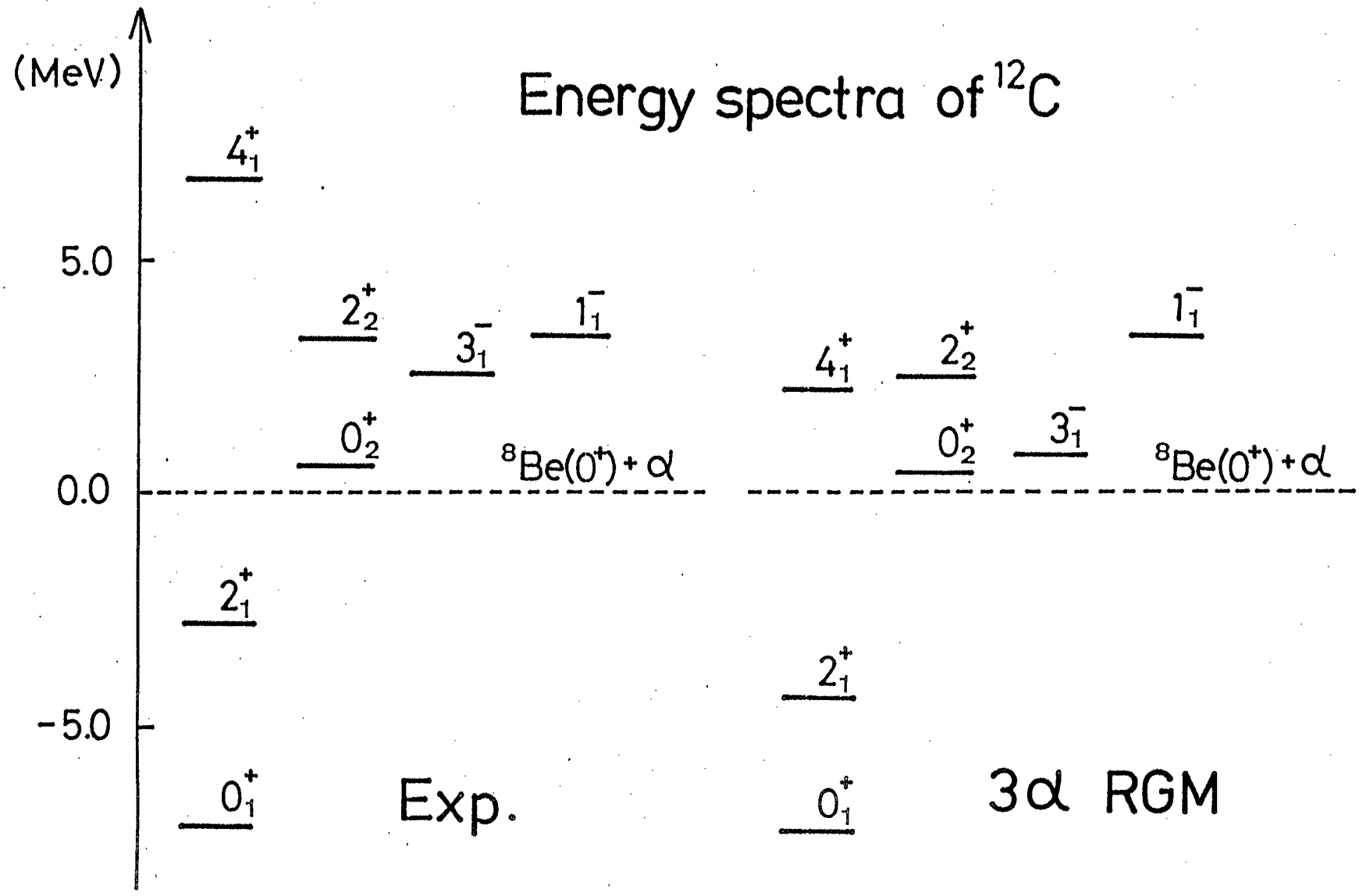
Energy spectra of ^{12}C
(MeV)
5.0
0.0
-5.0
4_1^+
2_2^+
3_1^-
1_1^-
0_2^+
$^8Be(0^+)+\alpha$
2_1^+
0_1^+
Exp.
4_1^+
2_2^+
1_1^-
0_2^+
3_1^-
$^8Be(0^+)+\alpha$
2_1^+
0_1^+
3α RGM

Fig.10

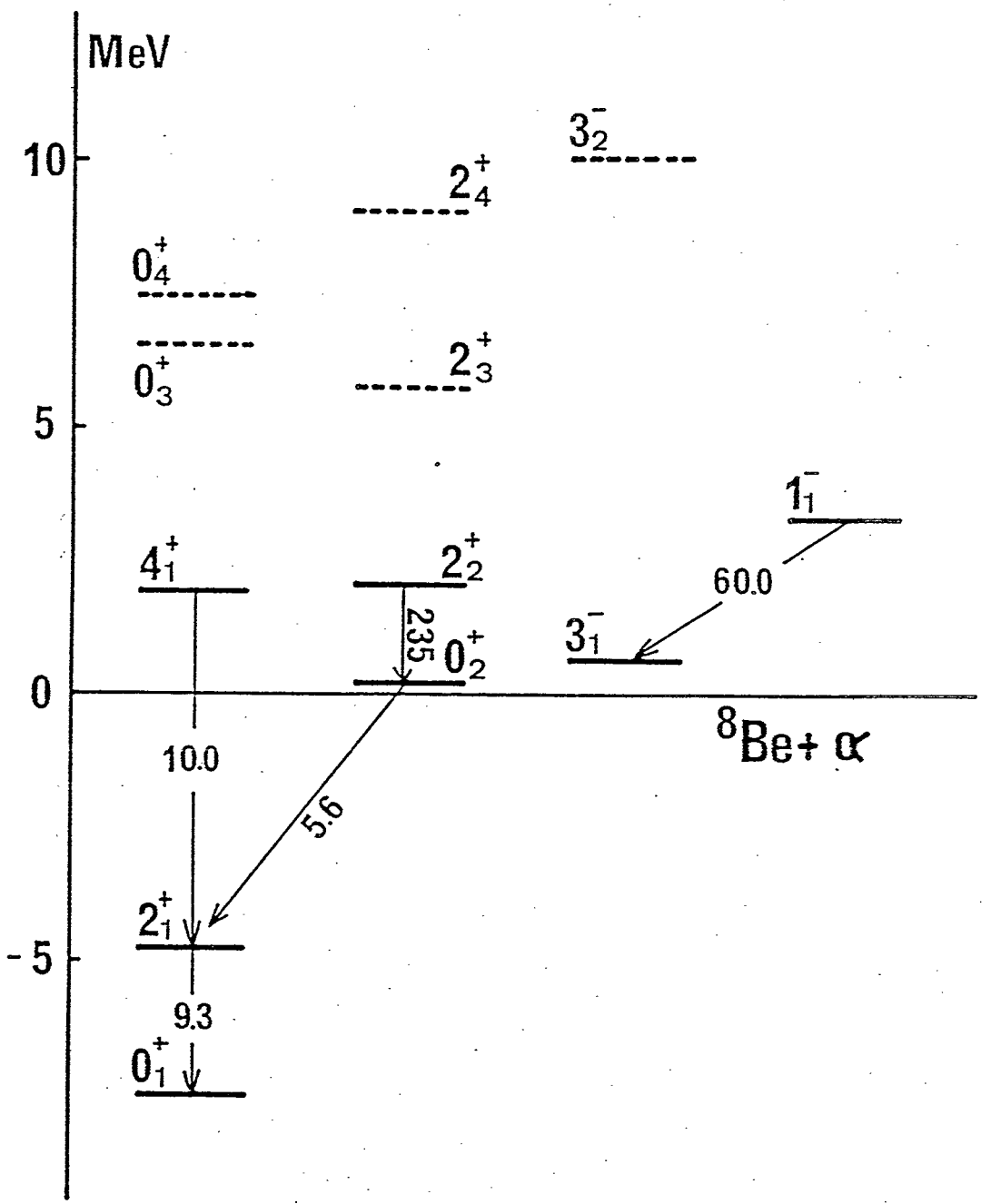
MeV
10
5
0
-5
3_2^-
2_4^+
0_4^+
2_3^+
0_3^+
1_1^-
4_1^+
2_2^+
60.0
235
3_1^-
0_2^+
$^8Be + \alpha$
10.0
5.6
2_1^+
9.3
0_1^+

Fig. 11

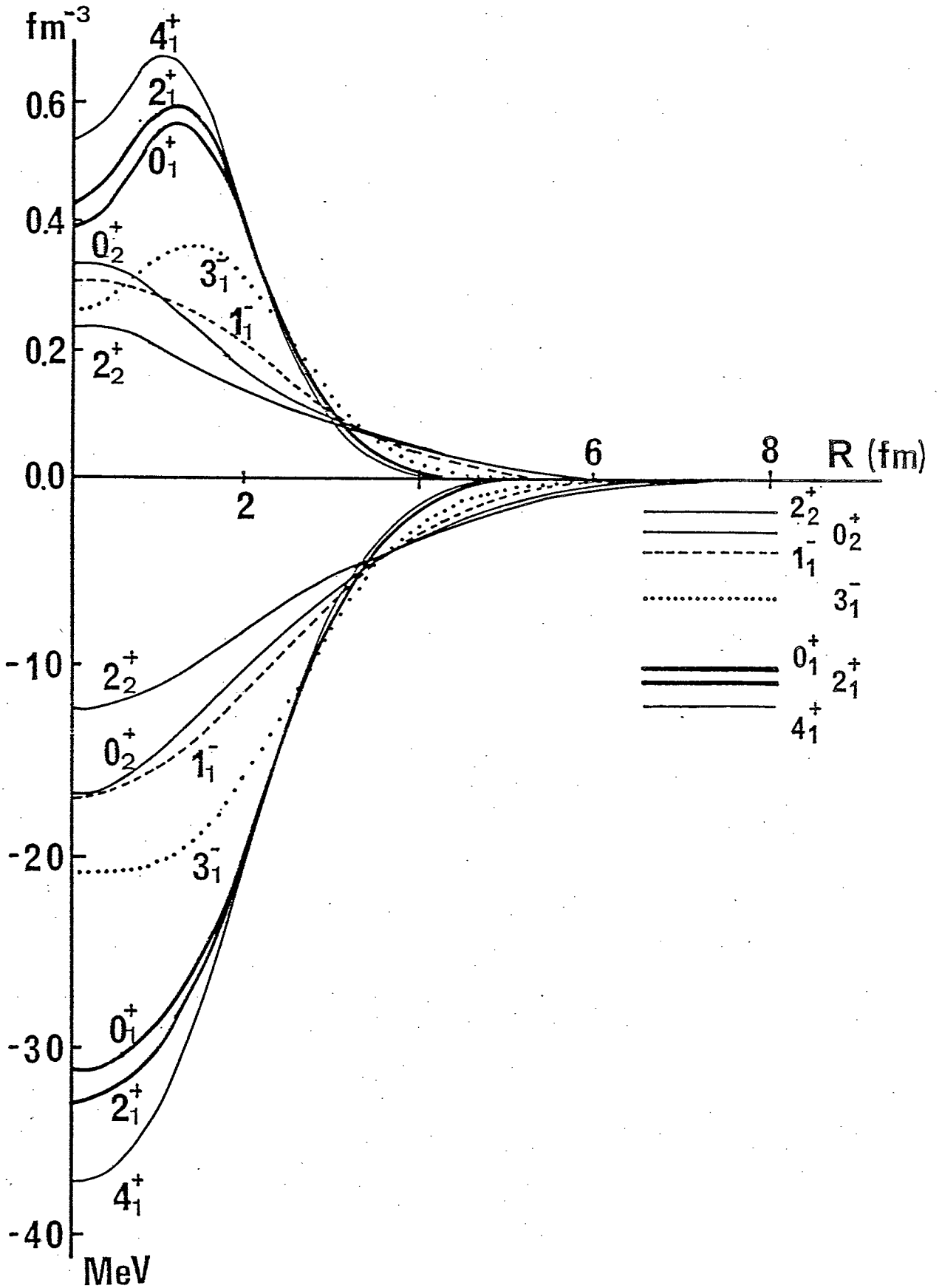

Fig.12

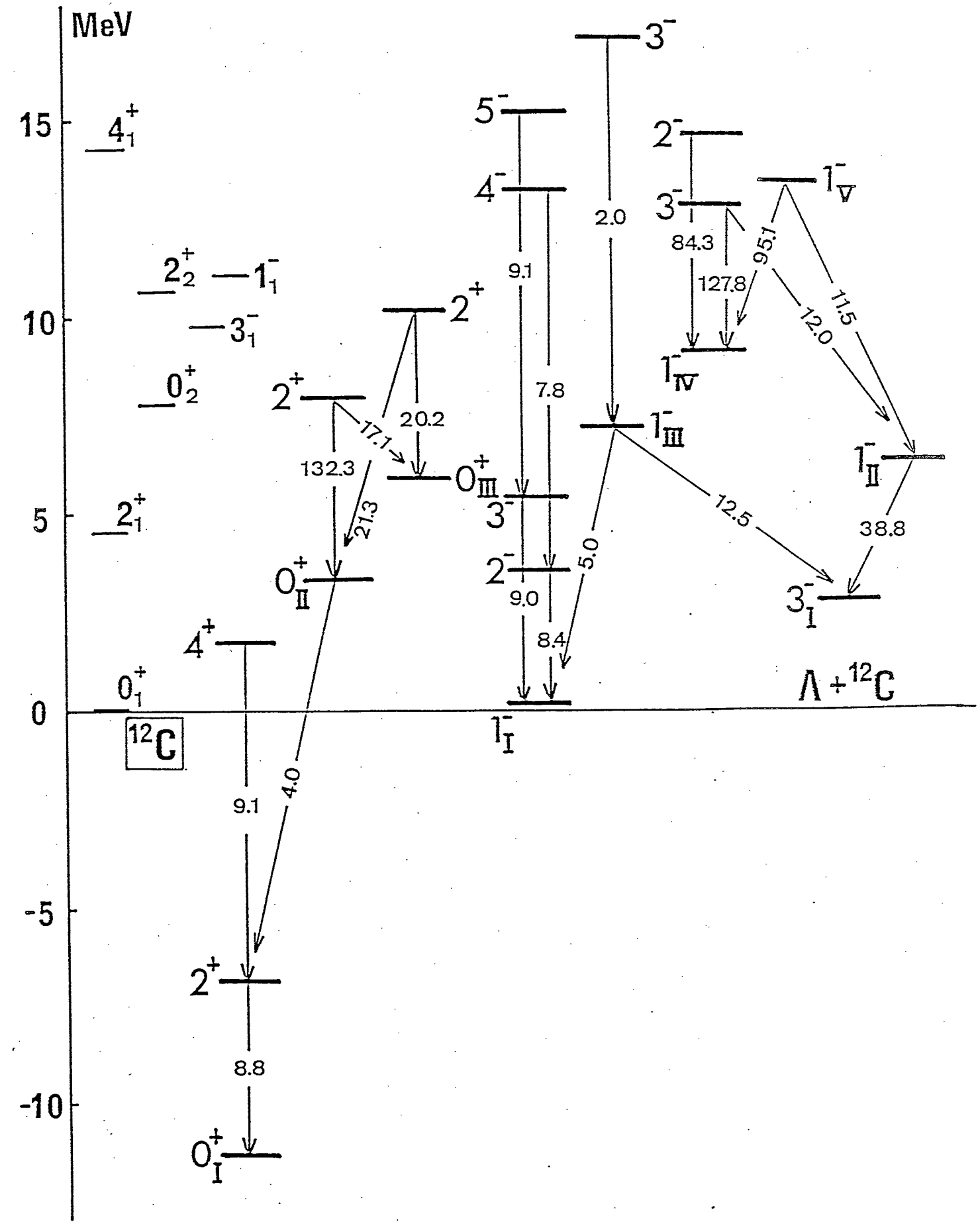
MeV
15
10
5
0
-5
-10
4^+_1
2^+_2
1^-_1
3^-_1
0^+_2
2^+_1
0^+_1
^{12}C
4^+
2^+
0^+_I
2^+
0^+_{II}
2^+
0^+_{III}
5^-
4^-
3^-
2^-
1^-_I
3^-
1^-_{III}
2^-
3^-
1^-_{IV}
1^-_V
1^-_{II}
3^-_I
$\Lambda + ^{12}C$
9.1
132.3
17.1
20.2
21.3
4.0
8.8
9.1
7.8
9.0
8.4
2.0
5.0
84.3
127.8
95.1
12.0
11.5
12.5
38.8

Fig.13

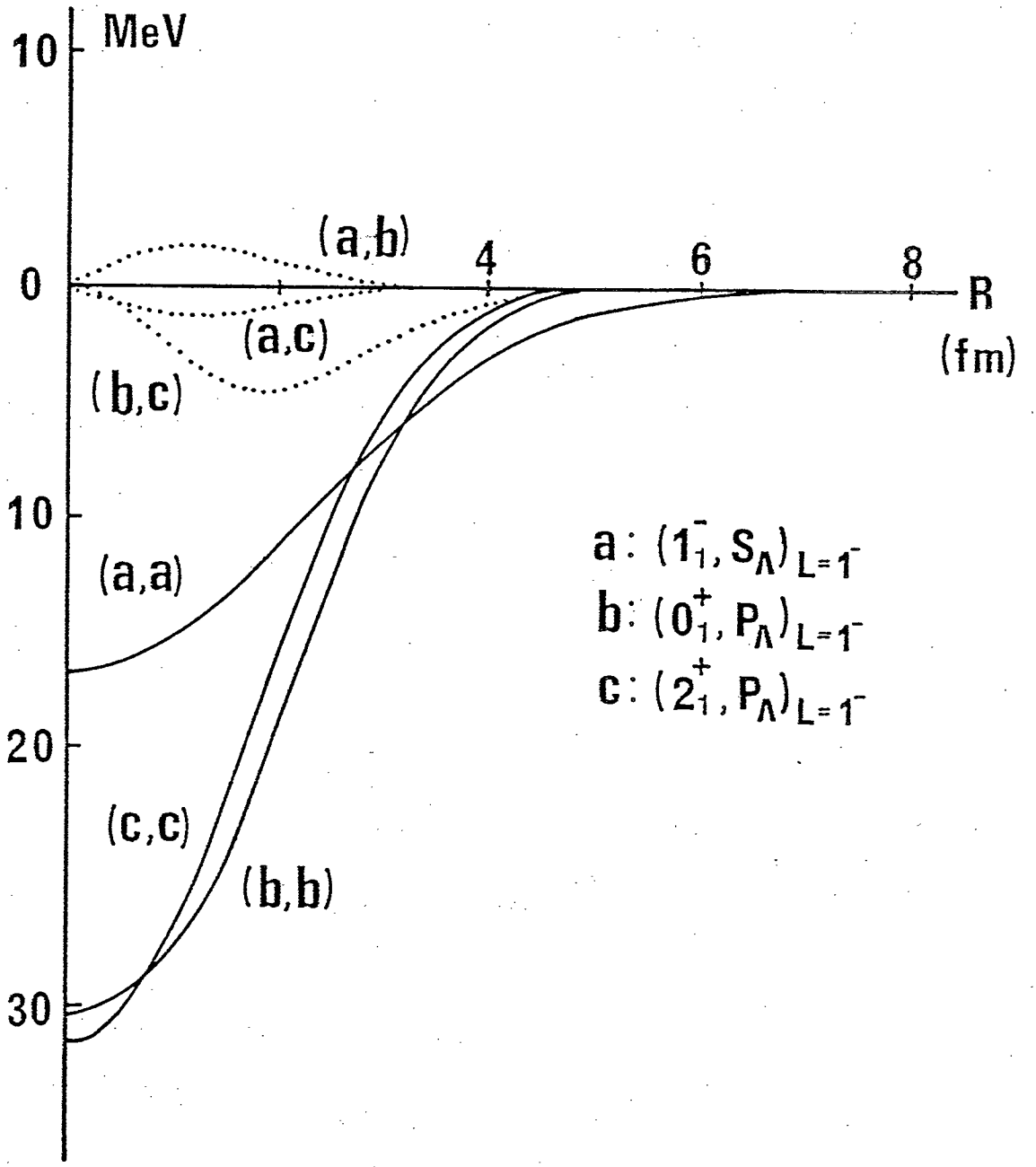
MeV
10
0
10
20
30
4
6
8
R
(fm)
(a,b)
(a,c)
(b,c)
(a,a)
(c,c)
(b,b)
a: $(1^-_1, S_\Lambda)_{L=1^-}$
b: $(0^+_1, P_\Lambda)_{L=1^-}$
c: $(2^+_1, P_\Lambda)_{L=1^-}$

Fig. 14

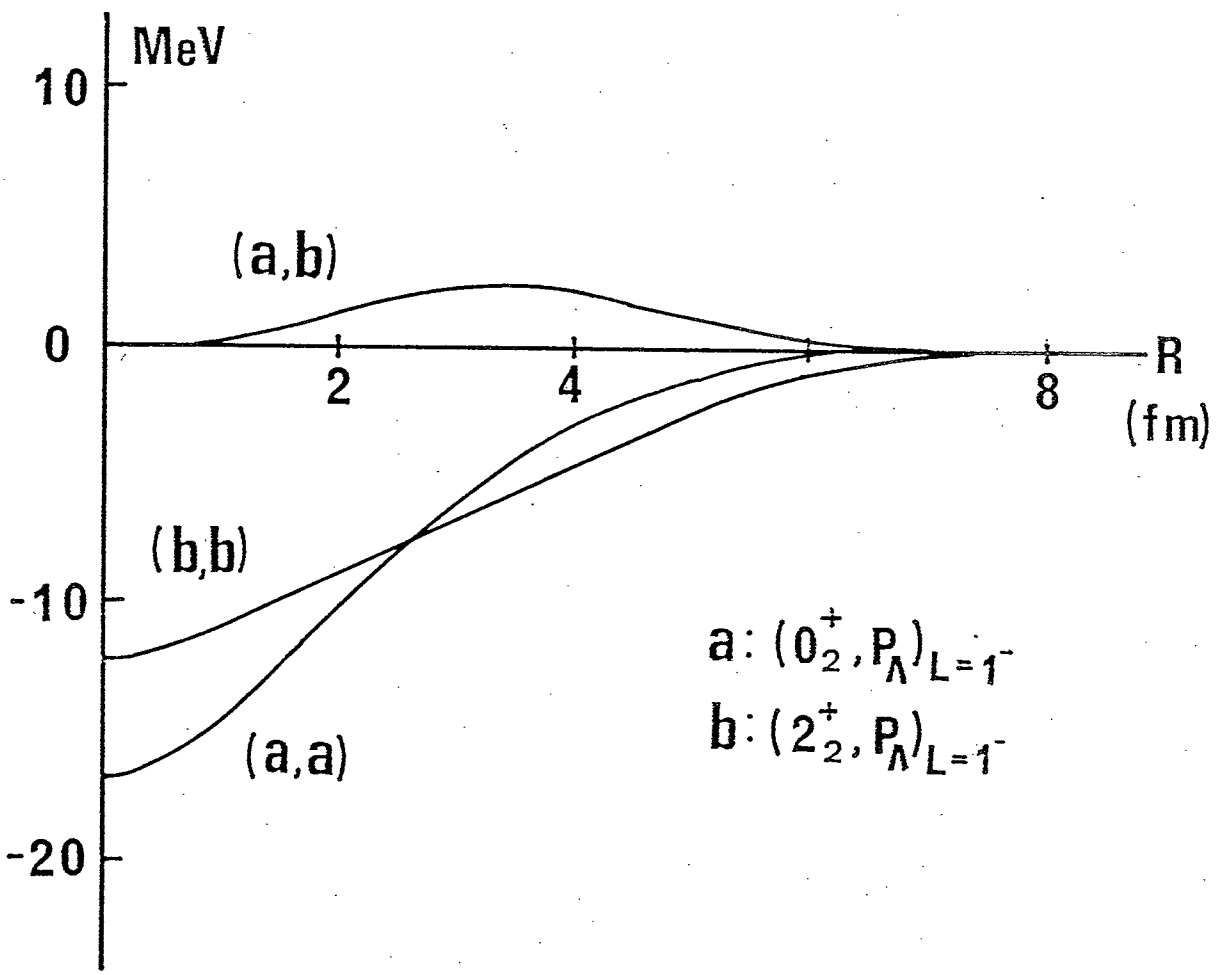

Fig.15

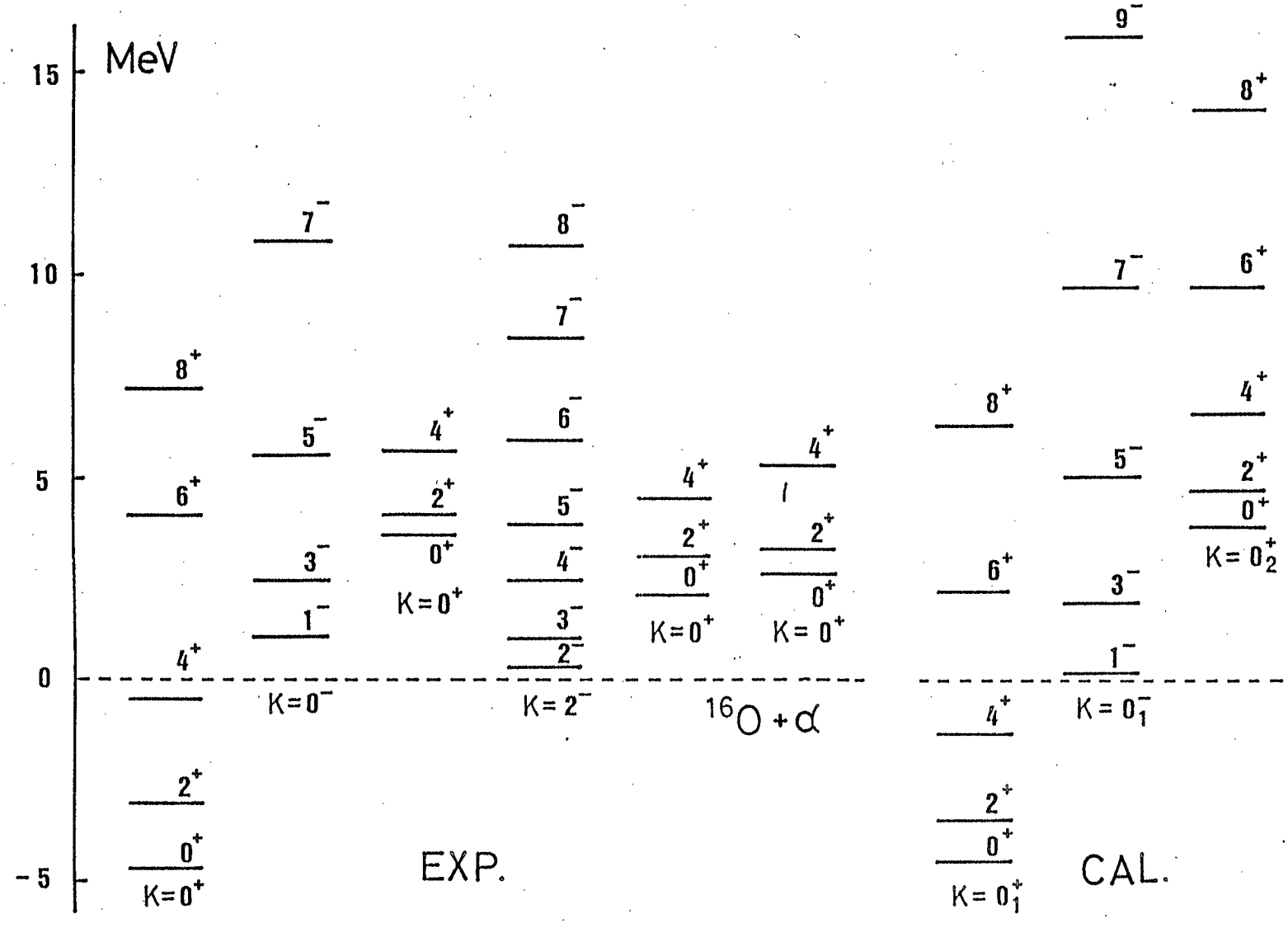
MeV
15
10
5
0
-5
8+
6+
4+
2+
0+
K=0+
7−
5−
3−
1−
K=0−
4+
2+
0+
K=0+
8−
7−
6−
5−
4−
3−
2−
K=2−
4+
2+
0+
K=0+
4+
2+
0+
K=0+
16O + α
8+
6+
4+
2+
0+
K=0+1
9−
7−
5−
3−
1−
K=0−1
8+
6+
4+
2+
0+
K=0+2
EXP.
CAL.

Fig.16

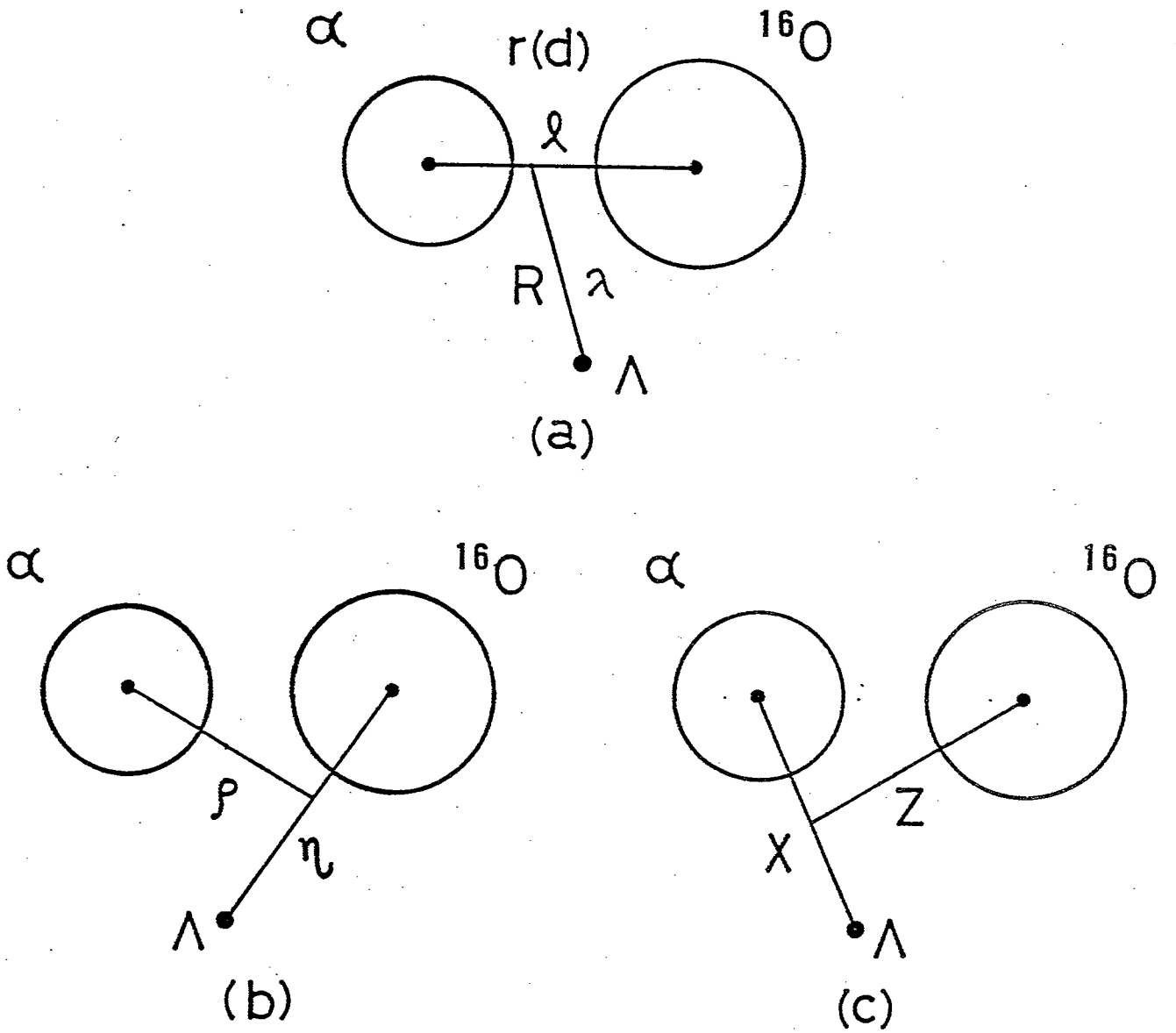

Fig. 17

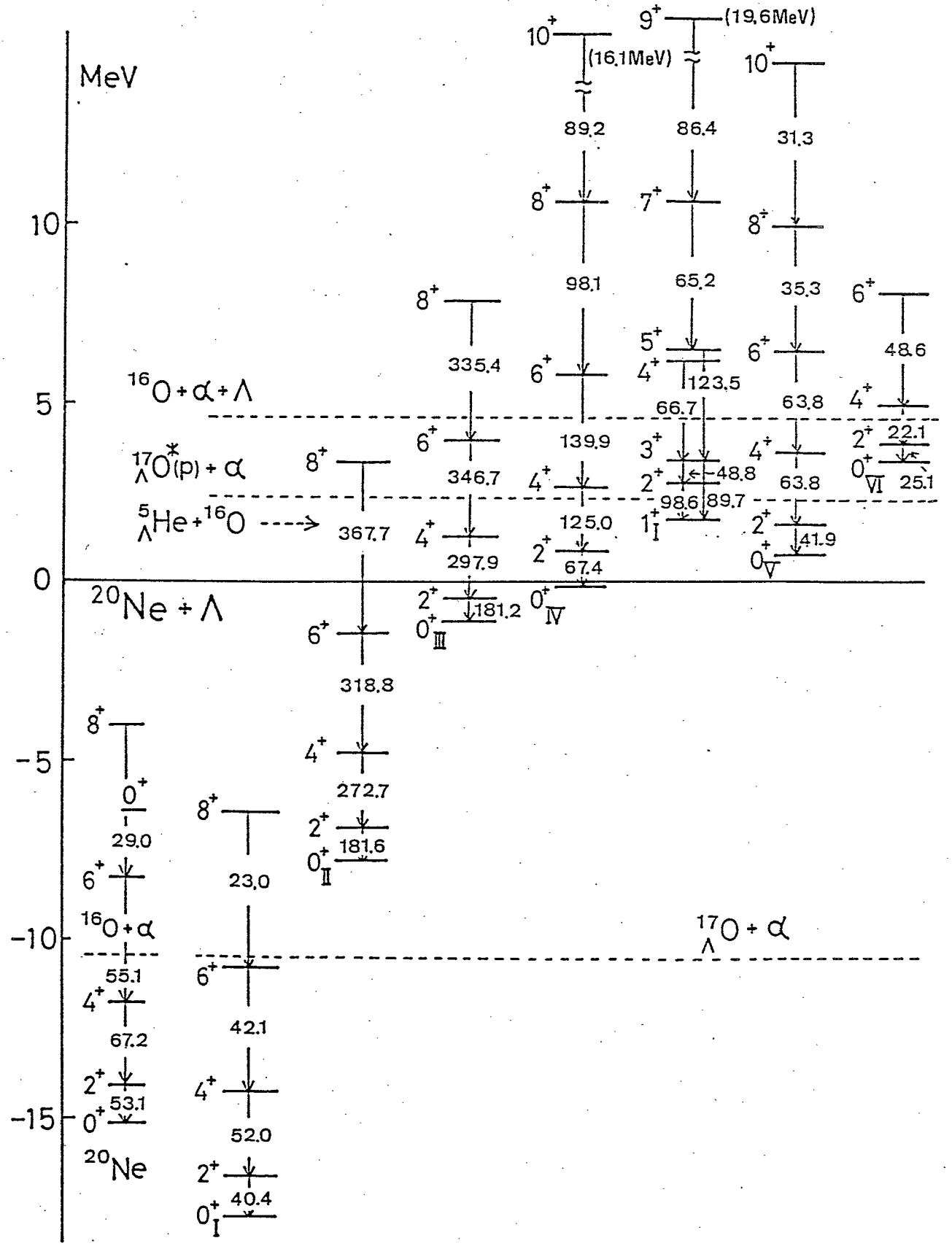
MeV
10
5
0
-5
-10
-15
$^{16}O+\alpha+\Lambda$
$^{17}_{\Lambda}O^{*}(p)+\alpha$
$^{5}_{\Lambda}He+^{16}O$
$^{20}Ne+\Lambda$
$^{16}O+\alpha$
$^{17}_{\Lambda}O+\alpha$
^{20}Ne
10^+
(16.1MeV)
89.2
8^+
98.1
6^+
139.9
4^+
125.0
2^+
67.4
0^+_{IV}
9^+
(19.6MeV)
86.4
7^+
65.2
5^+
4^+
123.5
66.7
3^+
2^+
48.8
98.6
89.7
1^+_I
10^+
31.3
8^+
35.3
6^+
63.8
4^+
63.8
2^+
41.9
0^+_V
8^+
335.4
6^+
346.7
4^+
297.9
2^+
181.2
0^+_{III}
6^+
48.6
4^+
2^+
22.1
0^+_{VI}
25.1
8^+
367.7
6^+
318.8
4^+
272.7
2^+
181.6
0^+_{II}
8^+
0+
29.0
6^+
55.1
4^+
67.2
2^+
53.1
0^+
8^+
23.0
6^+
42.1
4^+
52.0
2^+
40.4
0^+_I

Fig.18

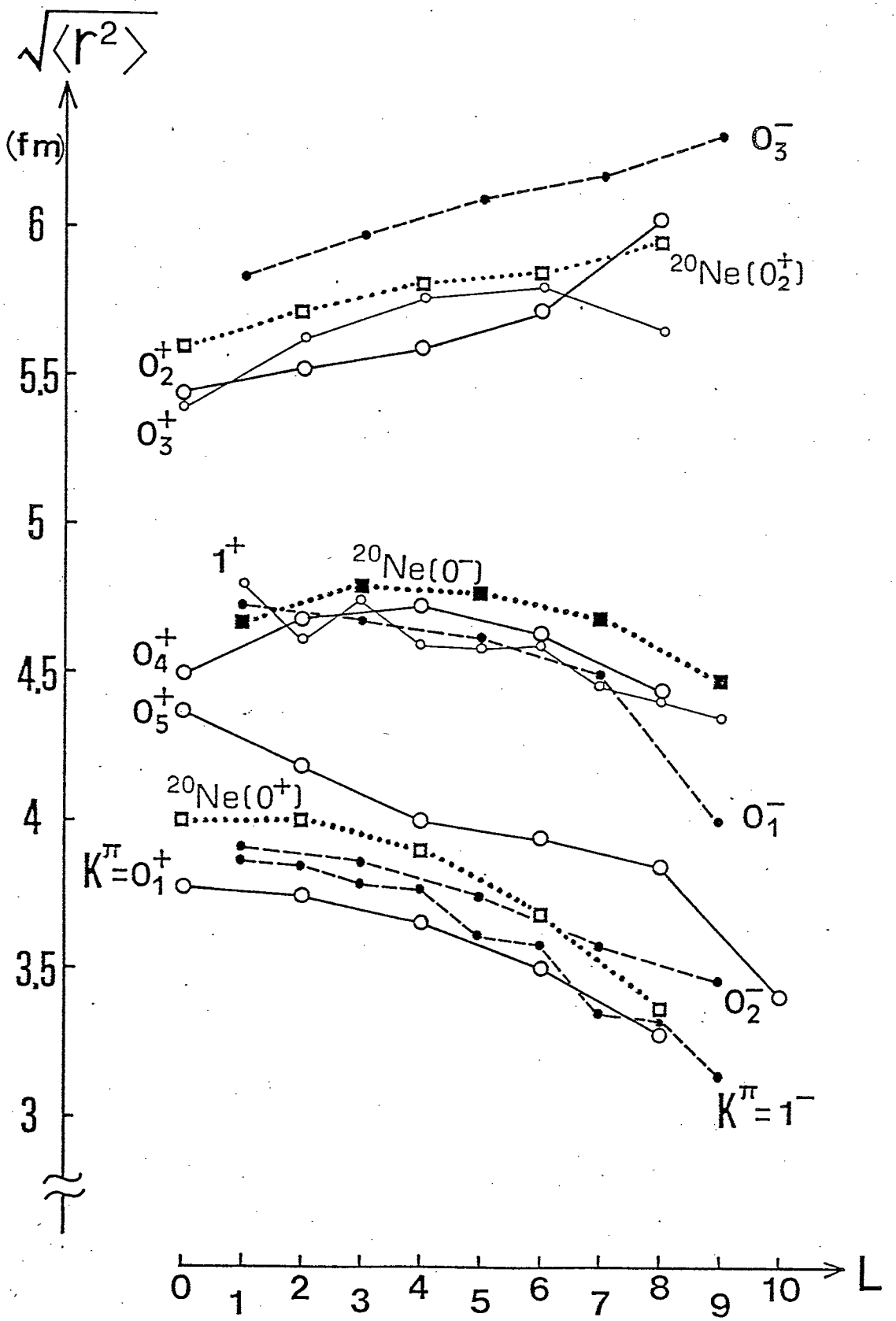
$\sqrt{\langle r^2 \rangle}$
(fm)
6
5.5
5
4.5
4
3.5
3
0_3^-
$^{20}Ne(0_2^+)$
0_2^+
0_3^+
1^+
$^{20}Ne(0^-)$
0_4^+
0_5^+
$^{20}Ne(0^+)$
0_1^-
$K^\pi=0_1^+$
0_2^-
$K^\pi=1^-$
0 1 2 3 4 5 6 7 8 9 10
L

Fig.19

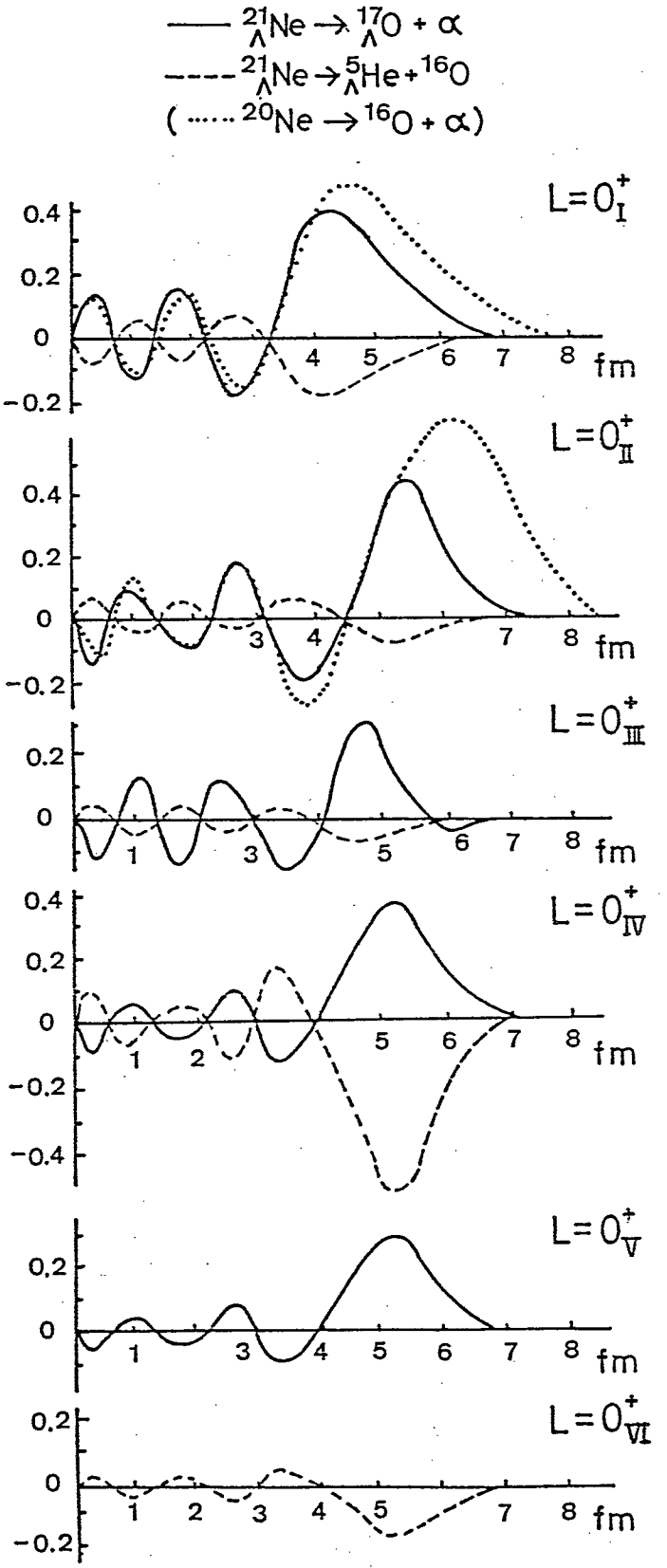
——— $^{21}_{\Lambda}Ne \rightarrow {}^{17}_{\Lambda}O + \alpha$
- - - - $^{21}_{\Lambda}Ne \rightarrow {}^{5}_{\Lambda}He + {}^{16}O$
(····· $^{20}Ne \rightarrow {}^{16}O + \alpha$)
$L=0^+_I$
$L=0^+_{II}$
$L=0^+_{III}$
$L=0^+_{IV}$
$L=0^+_V$
$L=0^+_{VI}$
fm

Fig. 20

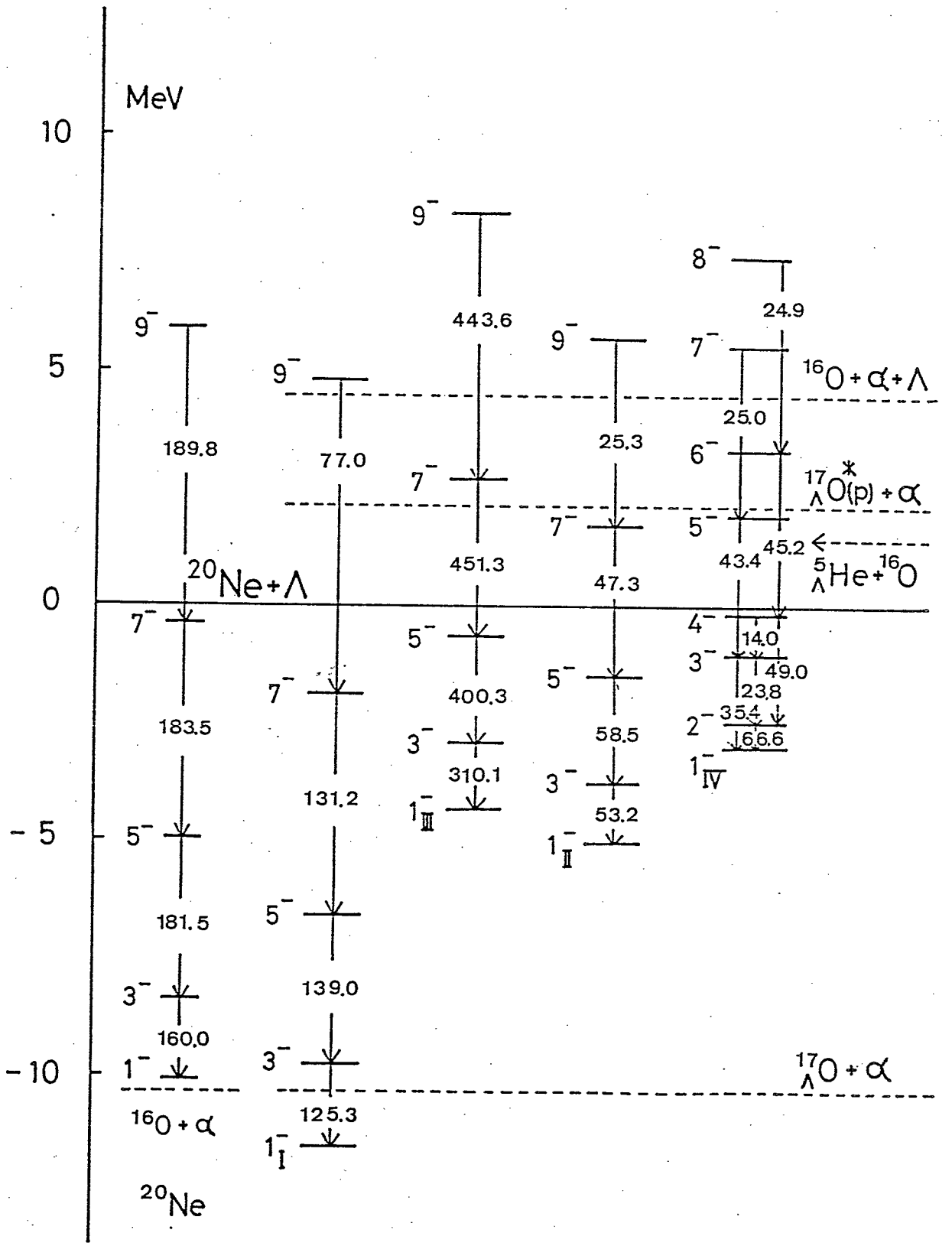
MeV
10
5
0
- 5
- 10
9⁻
189.8
7⁻
183.5
5⁻
181.5
3⁻
160.0
1⁻
16O + α
20Ne
20Ne+Λ
9⁻
77.0
7⁻
131.2
5⁻
139.0
3⁻
125.3
1⁻I
9⁻
443.6
7⁻
451.3
5⁻
400.3
3⁻
310.1
1⁻III
9⁻
25.3
7⁻
47.3
5⁻
58.5
3⁻
53.2
1⁻II
8⁻
24.9
7⁻
25.0
6⁻
5⁻
43.4
45.2
4⁻
14.0
3⁻
49.0
23.8
2⁻
35.4
16.6
1⁻IV
16O + α + Λ
17ΛO*(p) + α
5ΛHe+16O
17ΛO + α

Fig. 21

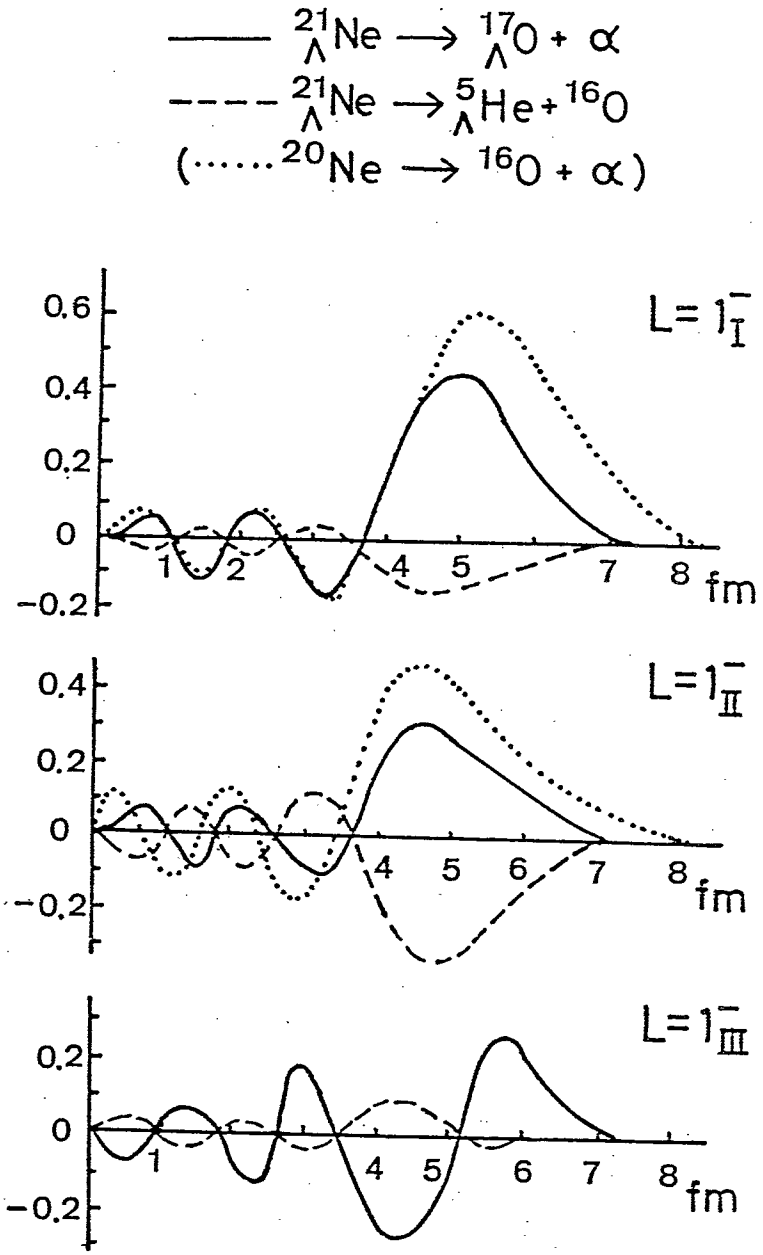
$^{21}_{\Lambda}Ne \rightarrow {}^{17}_{\Lambda}O + \alpha$
$^{21}_{\Lambda}Ne \rightarrow {}^{5}_{\Lambda}He + {}^{16}O$
$(\cdots\cdots {}^{20}Ne \rightarrow {}^{16}O + \alpha)$
L=1⁻I
L=1⁻II
L=1⁻III
0.6
0.4
0.2
0
-0.2
1
2
4
5
6
7
8
fm

Fig. 22